



universität
wien

MASTERARBEIT

Titel der Masterarbeit

A Tale of Two Molecules

Revisiting the $CO-A_V$ relationship in the L1495-B213
molecular cloud

Verfasser

Kieran Leschinski

angestrebter akademischer Grad

Master of Science (MSc)

Wien, 2014

Studienkennzahl lt. Studienblatt:

A 066 861

Studienrichtung lt. Studienblatt:

Masterstudium Astronomie

Betreuer:

Univ.-Prof. João Alves, PhD

Contents

1. Introduction	7
1.1. The L1495-B213 complex	8
1.2. Demarcation of Barnard regions 7, 10, 211, 213, 216, 217 and 218 . . .	10
1.3. The data sets used in this study	12
2. Extinction in the ISM	14
2.1. Determining hydrogen column density using dust extinction and the dust-to-gas ratio	14
2.1.1. Extinction due to dust particles in the interstellar medium . . .	14
2.1.2. The connection between colour excess and extinction	15
2.1.3. Column density and the reddening law	16
2.2. Techniques for mapping extinction	17
2.2.1. Star counting	18
2.2.2. Extinction by using color excess	20
2.2.3. Near Infrared Colour Excess Revisited - NICER	22
2.3. NICER in detail	24
2.3.1. Definitions	24
2.3.2. Our implementation of the NICER method	26
2.3.3. Star selection and pixel binning	28
2.4. Extinction maps used in this study	29
3. Column densities of ^{13}CO and $C^{18}O$ and their role in determining $N(H_2)$	34
3.1. Determining CO column densities	35
3.2. ^{13}CO and $C^{18}O$ maps	39
4. Mapping ^{13}CO and $C^{18}O$ versus A_V	41
4.1. Relationship between ^{13}CO , $C^{18}O$ and A_V inside the L1495-B213 filament	41
4.1.1. Extinction, A_V	41
4.1.2. ^{13}CO column density and abundance	41
4.1.3. $C^{18}O$ column density and abundance	43
4.1.4. Relative isotopologue abundances: $X(^{13}CO/C^{18}O)$	43
4.2. Relationship between ^{13}CO and A_V outside the L1495-B213 filament	44
4.2.1. Extinction, A_V	44
4.2.2. ^{13}CO column density	44
5. The ridge method for cleaning noisy data	46
5.1. Justification	46
5.2. The ridge method algorithm	47

6. The X_{CO} factor - Comparing the column densities of ^{13}CO and $C^{18}O$ with extinction A_V	49
6.1. Relationship between ^{13}CO and A_V	49
6.1.1. The global relationship as derived from the ISM surrounding L1495-B213	49
6.1.2. Regional variations in ^{13}CO along the L1495-B213 filament	53
6.2. Relationship between $C^{18}O$ and A_V	57
6.2.1. The global relationship	57
6.2.2. Regional variations in $C^{18}O$	59
6.3. Relative abundances of ^{13}CO and $C^{18}O$ compared to H_2	61
6.3.1. Global relationships along the filament and around L1495-B213	61
6.3.2. Local variations of $X(^{13}CO)$, $X(C^{18}O)$ and $X(^{13}CO/C^{18}O)$	63
6.4. Confirmation of the ratio of the isotopologues ^{13}CO to $C^{18}O$ - $X(^{13}CO/C^{18}O)$ and departures therefrom	64
6.5. The $X(CO/H_2)$ ratio and conversion to $N(^{12}CO)$	64
6.6. Comparison to the literature	66
6.6.1. Comparison to the study by Frerking et al. (1982)	66
6.6.2. Comparison with other authors	69
7. Summary and conclusions	72
8. Future work	75
9. Acknowledgements	76
9.1. Official acknowledgements	76
9.2. Personal acknowledgements	76
Appendices	82
A. Maps	82
A.1. L1495-B213 filament maps	82
A.1.1. Extinction map - A_V	83
A.1.2. Column density map - $N(^{13}CO)$	84
A.1.3. Column density map - $N(C^{18}O)$	85
A.1.4. Abundance map - $X(^{13}CO)$	86
A.1.5. Abundance map - $X(C^{18}O)$	87
A.1.6. Isotopologue abundance map - $N(^{13}CO)/N(C^{18}O)$	88
A.2. Surrounding region maps	89
A.2.1. Extinction Map - A_V	89
A.2.2. Column density map - $N(^{13}CO)$	90
A.2.3. Abundance map - $X(^{13}CO)$	91

B. Python notebook for generating extinction values and comparative data sets	92
C. Barnard's Catalogue Entries for Taurus	104
D. List of Figures	109
E. List of Acronyms and Symbols	110
F. Deutsche Zusammenfassung	111
G. Curriculum Vitae	112

Abstract

Molecular hydrogen is one of the key pieces in the star formation puzzle. However, in the cold (10K) interiors of molecular clouds the properties of H_2 must be inferred by using measurements of extinction or the emission from tracer molecules such as CO . As extinction occurs at all wavelengths and scales linearly with column density, it is a better tracer of H_2 than CO . However it is mainly useful for nearby ($d < 1kpc$) clouds, whereas CO is detected in extragalactic sources. The conversion factor between these two methods is therefore of great importance in many fields of astronomy.

By looking at 7 different sub-regions in the L1495-B213 filament in Taurus, we aimed to constrain the $^{13}CO - A_V$ and $C^{18}O - A_V$ relationships as well as shed some light on the large discrepancies in the molecular abundances presented in the literature.

We generated extinction maps from the 2MASS (Skrutskie et al., 2006) catalogue using the NICER technique (Lombardi and Alves, 2001) and compared these pixel by pixel to the maps of ^{13}CO and $C^{18}O$ emission from Goldsmith et al. (2008) and Hacar et al. (2013). This was done for 9 data subsets: The L1495-B213 filament as a whole, the region surrounding the L1495-B213 filament (only in A_V and ^{13}CO), and each of the 7 sub-regions in the L1495-B213 filament.

We found that ^{13}CO was a poor tracer of H_2 at medium to high column densities ($A_V > 2^m$). $C^{18}O$ emission on the other hand showed remarkable linearity when compared to extinction in the range $2^m < A_V < 20^m$. Our best fit to the whole L1495-B213 filament is:

$$N(C^{18}O) = (2.25 \pm 0.37) \cdot 10^{14} \cdot (A_V - 1.07 \pm 0.60)$$

After comparing the slopes of the individual sub-regions, we found a weak correlation between $C^{18}O$ abundance and the surface density of YSOs in the sub-region as reported by Hacar et al. (2013). We also found the isotopologue ratio to be approx. $N(^{13}CO)/N(C^{18}O) \approx 8 \pm 3$ for the ISM in the solar neighbourhood, which is similar to the ISM value given by Wilson and Rood (1994).

Through studying 7 different sub-regions in the L1495-B213 cloud we see a remarkable variation in the $^{13}CO - A_V$ and $C^{18}O - A_V$ relationships, akin to the variation seen in the literature values over the last 30 years. We conclude that ^{13}CO is most useful as a tracer of the diffuse ($A_V < 2^m$) extra-filamentary gas and should not be used to determine masses of filaments or cores. Where possible $C^{18}O$ should be the tracer of choice for the denser gas ($A_V > 2^m$).

1. Introduction

”If you wish to make an apple pie from scratch, you must first invent the universe.”
- Carl Sagan.

However in order to invent the universe, one must know its constituents: Hydrogen (for the most part). Hydrogen makes up over 90% of the universe. It is also the primary ingredient in stars and the star formation process. Hence in order to answer the timeless questions about the origins of the Sun, the Earth and even ourselves, we need to understand the life cycle of hydrogen. Star formation occurs when large reservoirs of hydrogen succumb to their own gravitational attraction and collapse (Shu et al., 1987). However hydrogen exists primarily as a very diffuse, quasi-static interstellar medium (ISM). We know that both stars and the ISM exist because we have observed large quantities of both (Trumpler, 1930). The pressing question currently is how do stars form out of the ISM? Many authors have looked for the answer to this question (Bok, 1977, Shu, 1977, Shu et al., 1987, Bonnell et al., 1998). Current theories propose that the ISM collapses into filaments and that inside these filaments dense cores form (Schneider and Elmegreen, 1979, Hartmann et al., 2001). It is from these dense cores that the stars are born.

Currently, the weakest link in the star formation chain is how the filaments, and indeed the dense cores, come to be. With the newest generations of telescopes (e.g. Herschel - Pilbratt et al., 2010) and observational and reduction techniques (e.g. FIVE - Hacar et al., 2013), we are able to see inside these filaments with a much greater resolution than ever before. However much of the initial characterisation of a filament still depends on the determination of the molecular hydrogen column density along the line of sight, whether that be from direct measurements of extinction or an extrapolation based on the column density of other molecules. The link between the dense ISM and star formation is well established (Krumholz et al., 2011), as is the link between the existence of CO and the denser regions of the ISM (Dame et al., 1987). Therefore an accurate knowledge of the CO column density in a cloud, or even another galaxy, can provide a realistic measure of the possible future star formation in that region. Hence our interest in knowing the relationship between CO and H_2 . Unfortunately the exact relationship between the dust column density and CO is not very well constrained. There have been many studies into this relationship for several different molecular clouds. This has resulted in a lack of agreement about the exact underlying dependence (Frerking et al., 1982, Duvert et al., 1986, Lada et al., 1994, Alves et al., 1999, Hayakawa et al., 2001, Kainulainen et al., 2006, Pineda et al., 2008). It is the goal of this thesis to shed some light on this lack of agreement.

Atomic (HI) and ionised (HII) hydrogen is generally directly observable via continuum radiation, emission, absorption and electronic spin-flip lines. Observations become problematic when trying to observe molecular (H_2) hydrogen. H_2 is notoriously difficult to observe because, due to the low temperatures [O(10K)] in the regions where it is created, it is unable to radiate. Being homo-nuclear by nature, its lowest purely rotational transition ($J = 2 \rightarrow 0$) has a first level spacing of 509K and can therefore only be excited in gas where the temperature is on the order of 100 K or greater (Dabrowski, 1984). Thankfully the next most abundant interstellar molecule, CO , does not suffer these limitations. With its weak permanent dipole moment, and therefore possibility for dipole transitions, it radiates at the temperatures found in the coldest [O(10K)] and densest regions of the ISM (Jefferts et al., 1970, Wilson et al., 1970). The lower abundances of the CO isotopologues ^{13}CO and $C^{18}O$ mean that column densities up to several tens of magnitudes worth of extinction are traceable using emission from the various isotopologues of CO .

Since the presence, and indeed the ubiquity, of CO throughout the galaxy was established (Jefferts et al., 1970, Wilson et al., 1970, Dame et al., 1987, Dame et al., 2001), CO has become the main tool used to reliably quantify the spatial distribution of molecular hydrogen. Many authors have attempted to calibrate the relationship between CO emission and H_2 column density (also known as the X_{CO} -factor) over the years, with most finding that their results differed by as much as a factor of 2 from the other authors. One of the earliest and most commonly cited works (Frerking et al., 1982) introduces a relationship that is at the lower limit of what has been found by most other authors. Given that this seminal study by Frerking et al. (1982) was conducted over 30 years ago and that our ability to investigate the $CO - H_2$ relationship has improved remarkably in the intervening years, we find it prudent that this relationship should be re-investigated. In this study we attempt to show that the differences in the $CO - H_2$ relationship as reported in the literature are intrinsic to the ISM and molecular clouds and that these differences also exist inside individual clouds on distance scales smaller than the molecular cloud itself. Therefore, without an intimate knowledge of the intra-cloud environment, the poorly constrained $CO - H_2$ relationship will remain poorly constrained.

1.1. The L1495-B213 complex

The region we have chosen to study is the L1495-B213 filament in Taurus (Figure 1). This region has been studied extensively because of its proximity to Earth (140pc - Elias, 1978b) and the multitude of different environmental conditions observed in each of the sub-regions. As these sub-regions appear to be at different stages in their star forming histories, the L1495-B213 cloud complex is a perfect laboratory in which

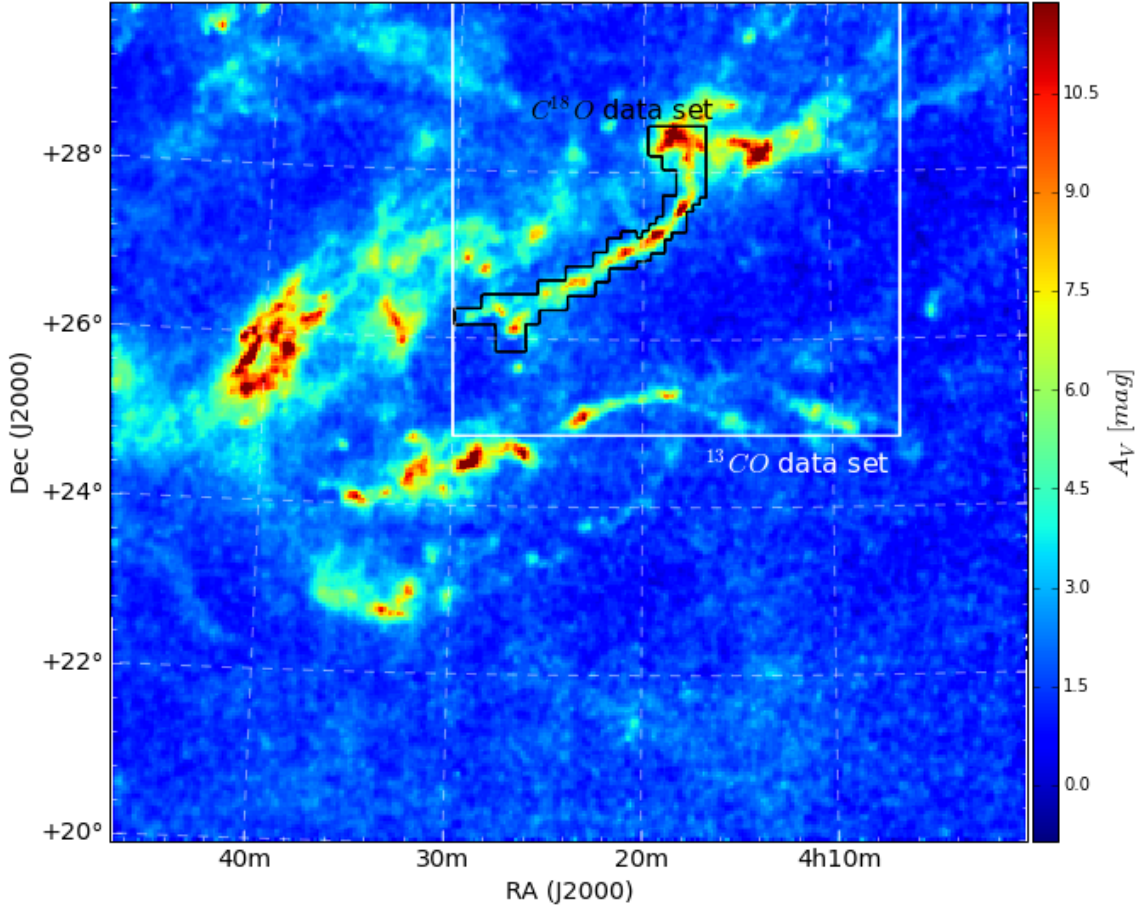


Figure 1: Extinction map of a 120 square degree region of the Taurus molecular cloud complex. We have focussed on the L1495-B213 complex in the white square in the upper middle. The black outline shows the region covered by the $C^{18}O$ data. The dense region located on the middle-left is the region originally studied by Frerking et al. (1982) (Discussed in §6)

to study the inherent processes of star formation (Elias, 1978b, Frerking et al., 1982, Duvert et al., 1986, Onishi et al., 1996, Goldsmith et al., 2008, Schmalzl et al., 2010, Palmeirim et al., 2013, Pineda et al., 2010, Hacar et al., 2013).

The complex was first catalogued in Barnard’s 1927 sky atlas (Barnard et al., 1927) as a coherent filament-like structure. In the Lynds Catalogue of Dark Nebulae (Lynds, 1962) the whole filament falls under the designation of L1495. The region is a long filamentary structure which contains several dense cores that are forming, or will eventually form, stars (Hartmann et al., 2001, Hacar et al., 2013). It is shown in Figure 2. The observed region covers 28 square degrees of the sky between $\alpha = [4^h 8^m, 4^h 30^m]$ and $\delta = [24^\circ 50', 30^\circ 10']$ and has been observed completely in ^{13}CO and A_V . The data set for $C^{18}O$ covers 8 square degrees along the filamentary structure located between $\alpha = [4^h 16^m, 4^h 30^m]$ and $\delta = [25^\circ 50', 28^\circ 33']$ and complements the ^{13}CO

and A_V data sets.

In our study we consider the region in two ways: 1) as a single coherent global structure, as catalogued by Lynds (1962) and 2) as a grouping of 7 individual regions with their own physical conditions. We refer to these sub-regions following the designations of Barnard et al. (1927). Hacar et al. (2013) showed that the region is in fact a superposition of 35 kinematically distinct sub-structures, which shows that even on small scales, we are still covering several internal sub-structures inside the filament. For the sake of consistency we shall adopt the nomenclature used in Hacar et al. (2013) and refer to the whole region as the L1495-B213 complex (a combination of the designations from the catalogues by Lynds, 1962 and Barnard et al., 1927).

For the analysis involving the ^{13}CO isotopologue we have also investigated the diffuse ISM surrounding the L1495-B213 complex. We included this surrounding environment in order to be able to probe the relationship between dust in the diffuse gas which causes only low to mild extinction ($A_V < 5^m$) and the unsaturated regime of the ^{13}CO emission. It is clear from Figure 1 that the remainder of the map also includes data that is associated with other cloud structures. These denser regions help to constrain the upper envelope of the data. The $C^{18}O$ data set focuses only on the regions of higher extinction ($A_V > 1^m$) inside the filament because regions outside the filament aren't sufficiently shielded from the interstellar radiation field for a stable population of $C^{18}O$ to exist. Consequently, the data set is much smaller than for ^{13}CO . As the scope for this study is the complex L1495-B213, we didn't source ^{13}CO or $C^{18}O$ data for the other cloud structures (e.g. L1486, L1506 Duvert et al., 1986). This may be approached in a future study.

1.2. Demarcation of Barnard regions 7, 10, 211, 213, 216, 217 and 218

The L1495-B213 complex comprises various different regions, each with its own dynamical history. This is visible not only through the differences in extinction and CO emission in the different sub-regions, but also through the difference in chemical compositions and the number of detected YSOs in each of the sub-regions (Hacar et al., 2013). Furthermore, according to the study on the cloud kinematics in L1495-B213 by Hacar et al. (2013), the perceived continuous filamentary structure is actually due to the superposition of many smaller and shorter filaments. This also supports the assumption that the sub-regions of L1495-B213 are structures in themselves and therefore deserve to be studied separately. To this end we divided the L1495-B213 complex into 7 regions: B7, B10, B211, B213, B216, B217 and B218.

Rather than using the brightness boundaries between the subregions as indicated by Barnard (Barnard et al., 1927), we decided to split the regions using the contour

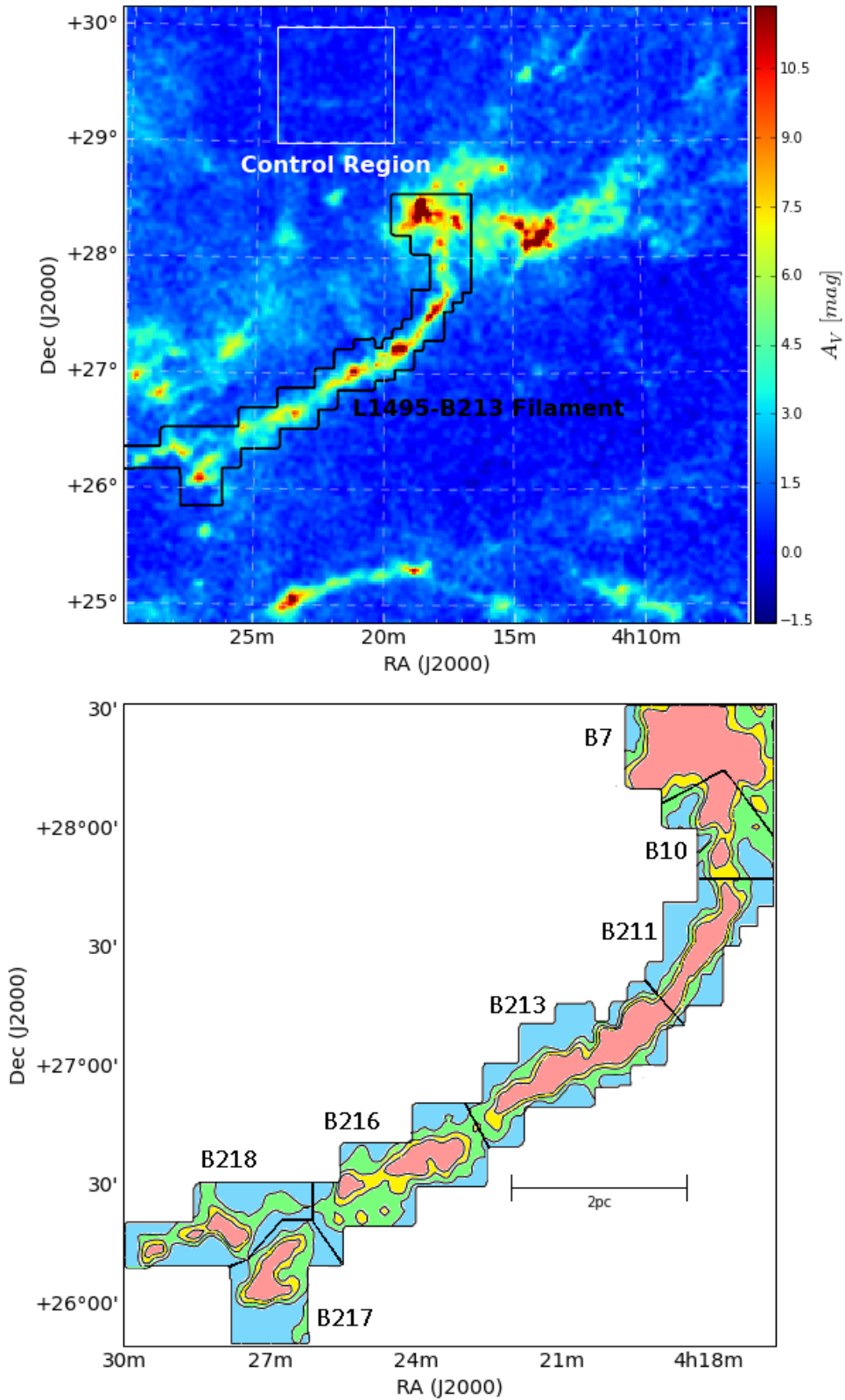


Figure 2: Top: The region covered by the ^{13}CO data. The black outline shows the region covered by the $C^{18}O$ data and the white box shows the region of low extinction we used to calibrate the intrinsic colours of stars in the J, H and Ks bands (discussed in detail in Section 2). Bottom: A schematic of the L1495-B213 filament. The contours are set to $A_V = [2.5, 3.75, 5]$ magnitudes. We used these contours to define the borders between the 7 sub-regions.

lines in extinction, A_V . The border between the B7/B10 and B211/213 complexes follows the $A_V = 5^m$ contour. The $A_V = 3.75^m$ contours defines the border between B211/213 and B216 and the three sub-regions of B216, B217 and B218 are split along the $A_V = 2.5^m$ contour. Unfortunately the border between B211 and B213 isn't clearly visible in extinction, so we used the historical border as defined in Schmalzl et al. (2010) and Hacar et al. (2013). This happens to go straight through the extinction peak seen in Figure 2. This cut is justified by the analysis of Hacar et al. (2013) - see Figure 15 therein. Figure 2 shows the demarcation lines and the extinction contours used.

Name	R.A. (J2000)	Dec (J2000)	Width [deg (pc)]	Height [deg (pc)]	Area [deg ² (pc ²)]	# Points
B7	64.540223	28.288447	0.776 (1.88)	0.521 (1.27)	0.30 (1.79)	2490
B10	64.369752	28.048863	0.435 (1.06)	0.438 (1.06)	0.14 (0.84)	1155
B211	64.524722	27.452356	0.687 (1.67)	0.812 (1.98)	0.31 (1.88)	2370
B213	65.154231	27.006567	0.895 (2.18)	0.666 (1.62)	0.36 (2.13)	2494
B216	65.887042	26.561377	0.875 (2.13)	0.708 (1.73)	0.32 (1.94)	2306
B217	66.451027	26.083734	0.437 (1.06)	0.541 (1.32)	0.20 (1.21)	1808
B218	66.751927	26.356405	0.770 (1.88)	0.416 (1.01)	0.23 (1.37)	1966

Table 1: Positional and area information for the sub-regions of L1495-B213. The width and height are defined by the most extreme points of the each sub-region and the area is the sum of pointings covered by observations in each sub-region.

Each of the Barnard regions cover approximately a third of a square degree on the sky (See Table 1). As the Taurus molecular cloud is located at a distance of 140pc (Elias, 1978b), each of these sub-regions covers on average 1.5 pc². Hence the variations in the large-scale abundances seen in this study exist on a sub-parsec scale.

1.3. The data sets used in this study

We obtained the ^{13}CO and $C^{18}O$ integrated fluxes used in Goldsmith et al. (2008) and Hacar et al. (2013) in the form of ASCII tables containing the offset in R.A and Declination as well as the flux measurement for each individual pointing on the sky. These were converted into a FITS map in radio coordinates. We determined the line of sight extinction values towards each pointing given in the ^{13}CO and $C^{18}O$ data sets by using a pipeline written by the author and the 2MASS point source catalogue (Skrutskie et al., 2006). The extinction values were determined for areas with the same beam-size as the original data. From this we created 9 spatially distinct data subsets:

- one for each of the 7 Barnard regions shown in Figure 2, covering A_V , ^{13}CO and

$C^{18}O$,

- one for the whole L1495-B213 filament, covering A_V , ^{13}CO and $C^{18}O$, and
- one for the surrounding diffuse part of the Taurus cloud, covering only A_V and ^{13}CO .

Each of these data sets contained information about position, ^{13}CO and $C^{18}O$ line intensities, A_K , A_V , $N(^{13}CO)$, $N(C^{18}O)$ and $N(H_2)$ column densities as well as $X(^{13}CO)$ and $X(C^{18}O)$ abundances for independent Niquist sampled pointings spaced at $37.5''$ within the specific region.

This thesis is organised in the following way: Section 2 gives the background and theory for using extinction to determine the H_2 column density. The mechanics of the Near-Infrared, Colour Excess Revisited (NICER) method is discussed and we provide a user-friendly explanation and example of how to use it. At the end of the section our extinction maps are presented. In Section 3 the theory behind using CO as a tracer of the H_2 column density is explained. The maps used in this study are also presented at the end of the section. Section 4 covers how we combined the data and used the extinction (A_V), ^{13}CO and $C^{18}O$ emission maps to generate a view of the relative abundances of the three molecules with respect to each other along the L1495-B213 filament. We take a brief interlude in Section 5 to introduce a simple method for extracting underlying trends in noisy data - the ridge method - and in Section 6 we present the results obtained using this method to determine the correlation between the H_2 and CO isotopologue column densities. We also present our main results and discuss the findings and implications of the connection between the 3 molecules. Section 7 lays down the conclusions of our study and summarises the results.

2. Extinction in the ISM

Hydrogen in all its forms is the primary constituent of the universe. In its atomic form it is found everywhere inside and outside galaxies. In its molecular form it is found all throughout galaxies where star formation is occurring. The vast clumps, cores and filaments that make up the structure of the interstellar medium and which are the birth places of stars are, not coincidentally, also home to vast reservoirs of H_2 (Palla and Stahler, 2002). Therefore in order to understand the fundamental processes that govern how the universe works and why things are the way they are, we first need to be able to detect the building blocks of molecular clouds.

2.1. Determining hydrogen column density using dust extinction and the dust-to-gas ratio

Unlike its atomic counterpart, molecular hydrogen is notoriously difficult to observe. In order for molecular hydrogen to be able to survive in the interstellar radiation field (IRSF), the ISM must be cold [O(10K)] and dense [$n(H) > O(10^2) \text{ cm}^3$]. However none of the rotational, vibrational or electronic transitions for molecular hydrogen are excited at these temperatures. Luckily the interstellar medium also contains dust, which is much more efficient at attenuating light and appears to be relatively uniformly distributed throughout the galaxy with densities proportional to the hydrogen column density (Bohlin et al., 1978). Thus in order to infer the presence of H_2 using dust, we must 1) assume a constant gas-to-dust ratio and 2) look for how the dust affects light from distant stars as it passes through regions of H_2 . A whole range of measurement techniques are based on exactly this phenomenon - Extinction.

2.1.1. Extinction due to dust particles in the interstellar medium

The most abundant molecule, H_2 , is remarkably inefficient at attenuating light due to its indifference towards continuum photons. However the dust particles present in the ISM are remarkably efficient at attenuating light due to their ability to absorb continuum photons. Hence molecular clouds are "visible" through their lack of emission in the optical and NIR regimes, something which sets them apart from the almost uniform stellar background (van Rhijn, 1929). The amount of attenuation by dust, and consequently the column density of H_2 along a line of sight, can be quantified by the amount of extinction that light from a background star suffers when travelling through a molecular cloud. The observed flux of a star is given by:

$$F_\lambda = \frac{L_\lambda}{4\pi D^2} e^{-\tau_\lambda} \quad (1)$$

where D is the distance to the star (which is generally poorly constrained), L_λ is the

intrinsic luminosity of the star and τ is the optical depth of the intervening material. The optical depth is nothing more than a measure of the number of particles present along the line of sight:

$$\tau_\lambda = \int n_d \sigma_d(\lambda) ds \quad (2)$$

where σ_d is the effective cross-section of the dust particles, n_d is the number of dust particles and ds is the distance between the observer and the star. If we assume the gas-to-dust ratio published by Bohlin et al. (1978), these terms can be replaced with the relevant values that determine the hydrogen column density. By combining these two expressions with Pogson's equation¹ relating stellar flux to observed stellar magnitude, it can be shown that there is a direct correlation between the extinction suffered by a star and the column density of hydrogen along that line of sight.

$$A_\lambda = 2.5 \log_{10}(F_\lambda^{int}/F_\lambda^{obs}) \quad (3)$$

$$A_\lambda = 2.5 \log_{10}(e^{\tau_\lambda}) \quad (4)$$

$$A_\lambda \approx 1.086 \tau_\lambda \propto \int n_d \sigma_d(\lambda) ds = f(\sigma, \lambda) \cdot N(H) \quad (5)$$

where the intrinsic flux, F_λ^{int} , is that of a model star, or of an observed star which is close by and suffers little from extinction (i.e. $\tau \approx 0$) and $f(\sigma, \lambda)$ is the gas-to-dust ratio for a given particle cross-section, σ , and wavelength, λ . $f(\sigma, \lambda)$ can be calculated by using the gas-to-dust ratio $N(H_2)/E(B-V)$ (Bohlin et al., 1978) and the conversions between extinction in different wavelengths and colour excess $E(B-V)$ (Rieke and Lebofsky, 1985).

2.1.2. The connection between colour excess and extinction

The easiest way to measure the extinction, A_V , along a line of sight is to look at how the colours of a background star have changed. Dust attenuates light differently at different wavelengths. For example, compared to the V filter almost a third more light is absorbed by interstellar dust in the B filter, assuming a normal reddening law ($R_V = 3.1$, see Rieke and Lebofsky, 1985). Hence, the more dust that lies along a line of sight, the dimmer a background star will appear in the B filter. Conversely stars appear brighter in the near-infrared filters of J, H and K_S relative to the V band, because less light is attenuated at these wavelengths. In general the following

¹Pogson's equation, also known as the apparent magnitude-flux equation:

$$m_1 - m_2 = 2.5 \log \frac{F_2}{F_1}$$

rule holds if the effective cross-section of dust grains remains constant: The smaller the relative size of the dust grain compared to the wavelength of light, the less light will be attenuated. In order to gain a measure of the extinction and therefore how much material is intervening along the line of sight, the difference in optical depth of this intervening material along two different lines of sight towards stars of the same spectral type at different distances can be used. The difficult part in this method is finding pairs of stars which are close to identical. For this spectroscopy or spectrophotometry must be used in order to precisely determine the spectral type of a pair of stars.

$$\tau_{\lambda,obs} - \tau_{\lambda,int} = \log_e\left(\frac{F_{int}}{F_{obs}}\right) + \log_e\left(\frac{D_{int}^2}{D_{obs}^2}\right) + \log_e\left(\frac{L_{obs}}{L_{int}}\right) \quad (6)$$

As the stars are of the same spectral type, the intrinsic luminosity term, $\frac{L_{obs}}{L_{int}}$, disappears. Furthermore, the nearby star was chosen because of the lack of interstellar material between us and it. Therefore the optical depth along the path to it is close to zero. The distance term is removed by observing the pair of stars in a second band. Historically this comparison was done in the B and V bands, but the same result can be achieved with any combination of filters:

$$A_{\lambda_1} \propto \tau_{\lambda_1} = \log_e\left(\frac{F_{\lambda_1,int}}{F_{\lambda_1,obs}}\right) + \log_e\left(\frac{D_{int}^2}{D_{obs}^2}\right) \quad (7)$$

$$A_{\lambda_2} \propto \tau_{\lambda_2} = \log_e\left(\frac{F_{\lambda_2,int}}{F_{\lambda_2,obs}}\right) + \log_e\left(\frac{D_{int}^2}{D_{obs}^2}\right) \quad (8)$$

Subtracting equation 8 from equation 7 gives:

$$A_{\lambda_1} - A_{\lambda_2} \propto \log_e\left(\frac{F_{\lambda_1,int}}{F_{\lambda_1,obs}}\right) - \log_e\left(\frac{F_{\lambda_2,int}}{F_{\lambda_2,obs}}\right) \quad (9)$$

where $A_{\lambda_1} - A_{\lambda_2} = E(\lambda_1 - \lambda_2)$ and is known as the colour excess. Colour excess is also known as the selective extinction as it quantifies the difference in absorption in the range between two filters. A_{λ} is known as the total extinction at a specific wavelength and quantifies the total amount of light that is attenuated along the path from the star to the observer. It is essentially an extension of the selective absorption where the second filter corresponds to a wavelength $\lambda \gg \sigma_d$. At such wavelengths, the dust is too small to measurably interact with the passing photons, essentially letting the photons pass unhindered. This results in $A_{\lambda_2} = 0$.

2.1.3. Column density and the reddening law

Colour, and more usefully colour excess, has the property that it remains constant with distance. The further away a star is, the fainter its apparent magnitude in *all bands*. As colour is the difference between fluxes in two bands of the same star, the

colour stays the same. Hence, colour excess removes the need to know the distance to a star in order to determine the line-of-sight extinction. The standard reference for colours and for selective- ($E(\lambda_1 - \lambda_2)$) to total-extinction (A_λ) is the paper by Rieke and Lebofsky (1985). The ratio between extinction and colour excess is referred to as reddening and is given as:

$$R = \frac{A_V}{E(B - V)} = 3.1 \quad (10)$$

where R is the reddening and $E(B-V)$ is the colour excess between the B and V bands. The one assumption here is that the distribution of interstellar grains and dust sizes remain constant throughout the Milky Way. This seems to be the case for the majority of the sky, however, it has been argued that this distribution changes depending on the conditions along different lines of sight, e.g. towards molecular clouds or the galactic centre. Cardelli et al. (1989) find that R could vary between 2.75 and 5.3 in the ultraviolet part of the spectrum where the difference in grain sizes plays the largest role. In the infrared region however, R remains remarkably constant. Using measurements of Lyman α absorption from the Copernicus satellite Bohlin et al. (1978) found the following relation for the ratio between the total number of particles and the colour excess along a line of sight:

$$\left\langle \frac{N(HI + 2H_2)}{E(B - V)} \right\rangle = 5.8 \cdot 10^{21} \text{ cm}^{-2} \text{ mag}^{-1} \quad (11)$$

Using the assumptions of a normal reddening law ($R = 3.1$) and presuming that all the hydrogen inside a molecule cloud is in the form of H_2 (i.e. $N(HI + 2H_2) \approx N(H_2)$) and that the number of atoms in an H_2 molecule is 2, equation 11 can be rewritten as:

$$\langle N(H_2) \rangle [\text{cm}^{-2}] = 9.4 \cdot 10^{20} \cdot A_V \quad (12)$$

Thus we have a measure of the line of sight column density of H_2 based on the distance-independent property of colour. Of course without any data on the HI column density, this method is limited to lines of sight where $N(H_2) \gg N(HI)$, i.e. towards molecular clouds, making it ideal for this study.

2.2. Techniques for mapping extinction

Determining the extinction towards a star is a useful way of determining the amount of interstellar material that lies along the path between the observer and the star. However the method of star matching is a time consuming process. It requires accurate knowledge of the stars spectral type and therefore the spectrum of the star (Elias, 1978a). In the absence of a complete spectral catalogue of the whole Milky Way galaxy it is prudent to develop other methods to infer the amount of extinction along a line of sight. Historically several methods have been employed to this end.

During the middle of the 20th century the star counting method was by far the most widely used (Bok and Reilly, 1947)². As various different astronomical filters became more readily available, so too did the method of colour excess. More recently the availability of infrared data and large scale infrared photometric surveys has seen a shift of the colour excess methods into the infrared regime (Lada et al., 1994). The Two Micron All Sky Survey (2MASS) (Skrutskie et al., 2006) has meant that large scale extinction maps can now be generated with relative ease for the entire sky by using the near infrared regime between 1.2 and 2.2 microns (Lada et al., 1994, Lombardi and Alves, 2001, Lombardi, 2009). The completion of the WISE all-sky survey has meant that the Rayleigh Jeans tail of a stellar blackbody curve can now be used to accurately determine total extinctions for filters blue-wards of $4.6\mu m$. The WISE filters are sensitive to the photons which are not greatly affected by the ISM and as such can be used to remove any local emission from the photometric measurements in a similar way to Majewski et al. (2011).

2.2.1. Star counting

Star counting has been around since the birth of modern astronomy. In the 1920s van Rhijn (1929) used it to determine our precise position with respect to the galactic plane. Bok and Reilly (1947) later applied this technique to quantify the dark clouds seen along the plane of the Milky Way. In essence the technique involves dividing an image (or a photographic plate) into equally sized rectangular regions or riseau squares and counting the number of stars that are above a given magnitude limit (Bok and Cordwell, 1973, Dickman, 1978). This action is applied to both the region of interest and a control field. The control field is preferably a region of sky close-by that suffers noticeably little extinction. van Rhijn (1929) provided approximate background counts for the majority of the Milky Way in order to circumvent the need to assume a constant stellar background throughout the Milky Way. According to Bok (1956) an approximate formula for determining the photographic (close to modern B filter) extinction depending on the number of stars per riseau square is:

$$A_{phot} \approx -2.66 \cdot \log_{10}(N_{riseau}/N_{control}) \quad (13)$$

where A_{phot} is the photographic extinction, N_{riseau} is the number of stars in a riseau square and $N_{control}$ the number of stars in the control field next to the region of interest.

While sufficient for finding general properties of a cloud's envelope and estimating lower limits for the amount of extinction, and therefore mass, in the central regions

²Although to say widely implies vastly more attention than was given by the astronomical community at the time

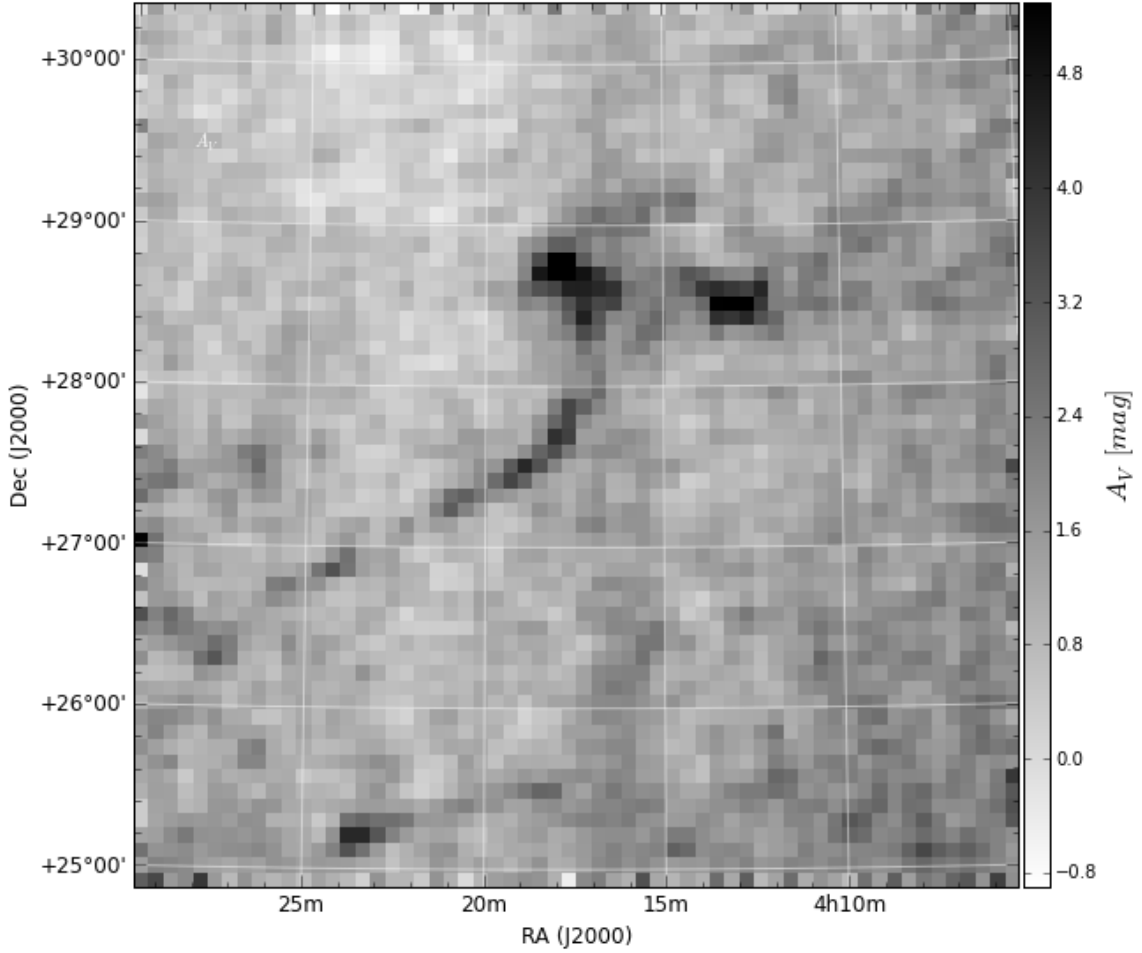


Figure 3: Map of the L1495-B213 region using the star counting technique, generated using the available 2MASS data for the region. We chose the resolution to be $5.5''$ per pixel, the same size used in the oft-cited dust maps by Schlegel et al. (1998) and the preliminary extinction map used by Frerking et al. (1982). The average number of stars per bin was 49 and the maximum 68, leading to a maximum measurable difference in extinction of $A_V = 4.9^m$ for a square with only a single star. This map was generated from the 2MASS catalogue and so has the advantage that many more stars are visible due to the use of Near Infrared (NIR) filters.

of dense molecular clouds, the star count technique suffers from several major problems. Firstly, it is limited by the amount of background stars. Near the plane of the galaxy this isn't a problem but at higher galactic latitudes where star densities fall off exponentially, this becomes a severe limitation. Secondly, as per the relation given by Bok (1956), a reduction in the number of stars by a factor of 100 could be induced by a mere 5 magnitudes of visual extinction. Thus, in order to have enough stars in a riseau square for any meaningfully deep extinction measurements the riseau width must be increased and the resolution reduced.

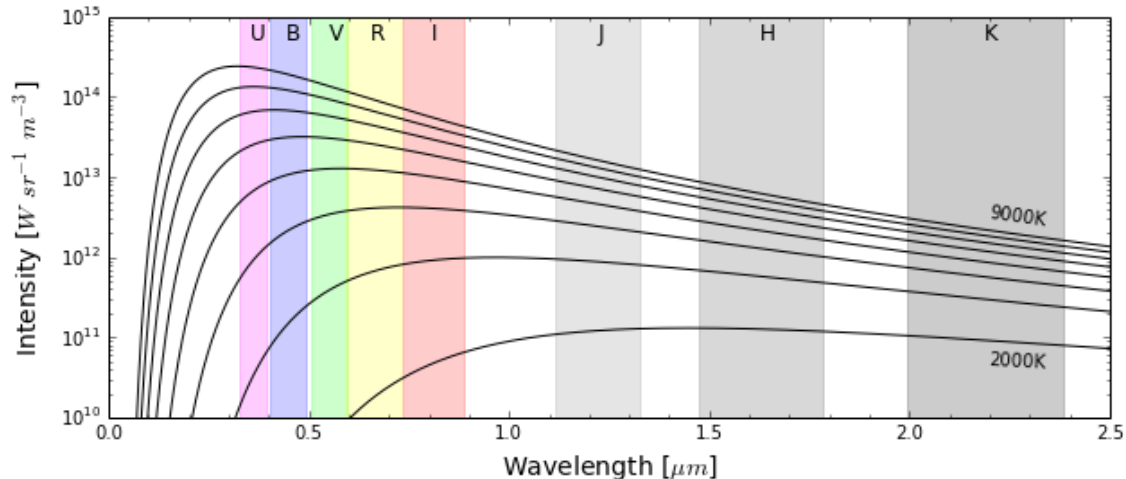


Figure 4: The black-body curves for stars with temperatures between 2000K and 9000K. It can be clearly seen that the scatter in relative intensities increases for bluer wavelengths. This in turn means that the bluer the bandpass, the greater the scatter in intrinsic colour.

Figure 3 shows the region covered in this study with the star counting method applied to it and a riseau square size of 5.5 arcmin. The average number of stars in squares where no extinction is present was 68. This corresponds to a maximum difference in extinction of $A_V = 4.9^m$ using Equation (13). Very little structure is visible and one would be forgiven for assuming that the L1495-B213 complex was nothing more than three small and separate clouds. Furthermore due to the Poisson statistics involved, the error per riseau square goes with \sqrt{N} . An example of this technique is given by Dickman (1978), where they attempt to estimate the masses of several clouds (B133, B134, B335 and B92) using both Blue and Red photographic plates and the star counting technique. For the sake of comparison, Bok (1956) and Frerking et al. (1982) both used riseau squares with a side length of 5.5 arcmin. This puts their extinction measurements on the same scale ($6'$) as the 100 micron dust continuum maps by Schlegel et al. (1998). Therefore it is safe to say that with this technique only large scale structure is mappable.

2.2.2. Extinction by using color excess

Stars radiate in a blackbody fashion. Depending on their surface temperature the peak of the spectral energy distribution (SED) will fall somewhere inside, or just blue- or red-wards of the visual range (Figure 4). This is a very useful attribute as it allows the determination of the apparent surface temperature of a star via the colour observed between two filters. With a little more information, such as narrow band photometric measurements of the H_α or H_β absorption lines, the determination of the

luminosity class and therefore mass and distance is possible. While the differences in spectral energy distributions between hot and cold stars are a great tool for determining characteristics of stars, the large variations through the visual range mean that it is almost impossible to determine accurate extinctions towards stars, without knowing the spectral types precisely. Several authors (e.g. Bok, 1956, Lee, 1968, Dean et al., 1978, Dickman, 1978, Cardelli et al., 1989) undertook this painstaking work of determining the spectral type for stars and then using BVRI photometric measurements to determine line of sight extinctions.

The huge variation in stellar colours in the visual range (particularly U-B and B-V³) is not present in the infrared regime (See Figure 4). Main sequence stars cover a range of around 2 magnitudes in B-V. This scatter drops to around 0.3 magnitudes in H-K_S, due to the fact that all stars with spectral classifications between O and M have the peak of their SED blue-wards of the H filter. Consequently the H-K_S colour effectively traces the beginning of the tail of the black-body curve, which, being exponential in nature, does not vary significantly with temperature. More recent studies have shown that including filters in the mid infrared (like those from the WISE all sky survey: W1, W2 - 3.4 μ m, 4.6 μ m) helps constrain the range of intrinsic colours to around 0.15 magnitudes. (Majewski et al., 2011, Zasowski et al., 2009).

Another advantage of using near infrared photometry is the greater transparency of dust at longer wavelengths. For example, dust attenuates 8.93 times less light (Rieke and Lebofsky, 1985) in the K_S band (2.2 μ m) than in the V band. This means that stars which are completely extinct at visual wavelengths are still visible in the near infrared. While this allows both the dust and hydrogen column density to be determined to a much greater depth, it also reduces the accuracy in A_V by the same amount. A K_S-band photometric uncertainty of $\sigma_{K_S} \approx 0.01$, which are common in the 2MASS catalogue, is equivalent to a V-band uncertainty of $\sigma_V \approx 0.1$.

In order to utilise the low scatter in intrinsic colours in the near infrared (NIR) regime, Lada et al. (1994) developed the Near Infrared Colour Excess (NICE) method. It takes advantage of the large area sky surveys which use the H and K_S filters, such as 2MASS and UKIDSS. The essence of the NICE method is that it divides an area into riseau squares, but instead of simply counting the number of stars in each square, the average colour excess for all stars falling inside the square is found:

$$\langle E(H - K_S) \rangle = \frac{\sum_{i=1}^N E(H_i - K_i)}{N} \quad (14)$$

³That being said, although $E(B-V)$ has been used to determine extinction values, this was only done in conjunction with spectroscopic/spectrophotometric measurements in order to determine the intrinsic luminosity and colours of the stars.

where $E(H - K_S) = (H - K_S)_{obs} - (H - K_S)_{int}$. Using the normal reddening law (Rieke and Lebofsky, 1985), the average H- K_S colour excess can be converted to a visual extinction:

$$\langle A_V \rangle = 15.9 \langle E(H - K_S) \rangle \quad (15)$$

The colour excess $E(H-K_S)$ can be found by either assuming an average intrinsic colour, $(H - K_S)_{int}$, for all field stars as reported in the literature or by defining a control field which suffers from very little extinction (for example away from the galactic plane)⁴. We found values of $(H - K_S)_{int} = 0.13 \pm 0.02$ and $(J - H)_{int} = 0.48 \pm 0.12$ for a control sample of 7013 stars taken from a $1^\circ \times 1^\circ$ region 1 degree north of the B7 sub-region. The region is shown in Figure 2. It is clear from Figure 5 why the NICE method (Lada et al., 1994) uses $E(H-K_S)$ over $E(J-H)$. The scatter amongst stars in the H- K_S colour is by far smaller than the scatter in the J-H colour. The smaller scatter allows a much greater accuracy when calculating the shift in colour due to extinction. However, because dust interacts less with light at longer wavelengths, the colour H- K_S is less sensitive to small variations in column density. This is reflected in Lombardi and Alves (2001) by the greater conversion factor used: $A_V/E(H - K_S) = 15.87$ compared to $A_V/E(J - H) = 9.35$. Nevertheless, large scale maps of regions of the galaxy have been constructed using this technique (Lada et al., 1994, Alves et al., 1999).

2.2.3. Near Infrared Colour Excess Revisited - NICER

If one colour (H- K_S) is good, then two colours (J-H, H- K_S) must be better. Hence Lombardi and Alves (2001) developed the Near Infrared Colour Excess Revisited (NICER) method which utilises the information contained in multiple colours. It is clearly visible in Figure 6 that both colours are affected by extinction. Each colour has advantages and disadvantages (intrinsic scatter vs sensitivity to dust), therefore by combining the information from both, a much more reliable quantification of regional extinction can be achieved. As can be seen in figure 6, as the amount of extinction along a line of sight increases, so too does the epicentre of the data-point cloud for J-H and H- K_S colours for a particular region. The central idea behind the NICER method is to follow the epicentre of the colour-colour cloud and calculate the most likely extinction associated with it. The dotted line depicted in Figure 6 is the theoretical line that the stellar colours should follow for increasing A_V according to Rieke and Lebofsky (1985). This is the primary method used in this study to determine the extinction values towards L1495-B213.

⁴Lada et al. (1994) report an intrinsic colour $(H - K_S)_{int} = 0.13 \pm 0.01$ magnitudes for a control field near IC 5146 ($l \approx 94^\circ$, $b \approx -5.4^\circ$), whereas Alves et al. (1998) report an intrinsic colour $(H - K_S)_{int} = 0.20 \pm 0.13$ magnitudes for a control field much closer to the galactic plane near L977 ($l \approx 89^\circ$, $b \approx +2.2^\circ$). Our value, even further from the galactic plane at $b \approx -16^\circ$ shows the same intrinsic H- K_S colour as that of Lada et al. (1994).

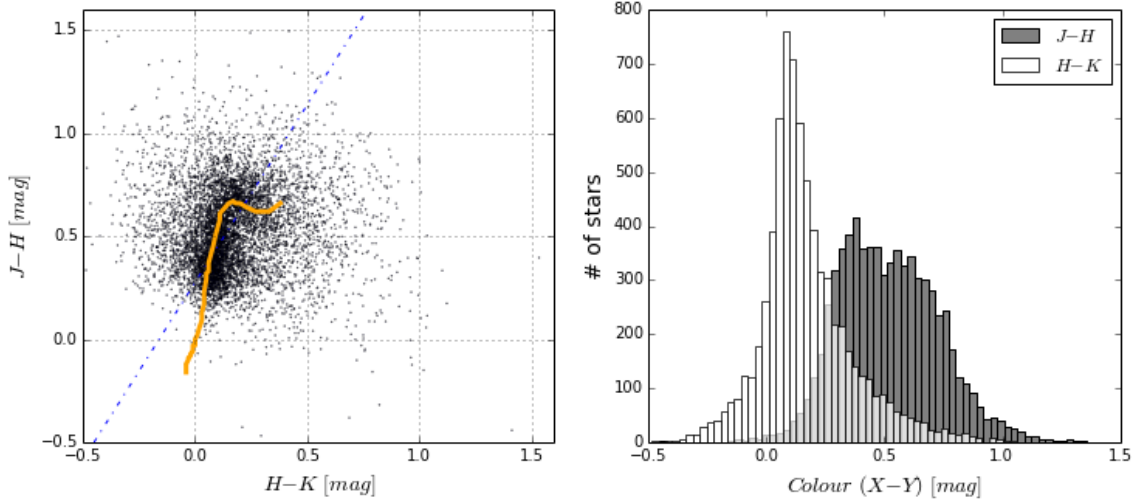


Figure 5: Left: The intrinsic scatter of colours found in the control field 1° north of the B7-10 region. The dotted line represents the direction in which colours will be shifted for increasing extinction. The solid wiggly line represents the intrinsic colours of main sequence stars of spectral types O5V to M8V. It is obvious that the scatter in the $J-H$ colour is much greater than the scatter in $H-K_S$ colour. Right: The spread of the $J-H$ and $H-K_S$ colours. The central peak of the $H-K_S$ colour marks the point that is used for the average intrinsic colour. We find $(H - K_S)_{int} = 0.13 \pm 0.02$ for the $H-K_S$ intrinsic colour. The average of the $J-H$ distribution is found to be $J - H = 0.48 \pm 0.12$.

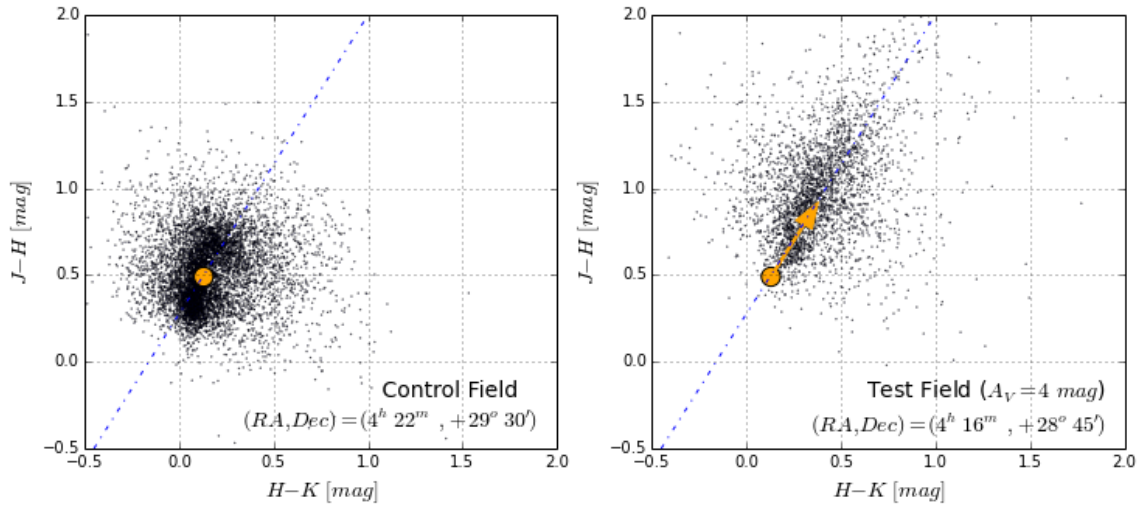


Figure 6: Left: The intrinsic scatter of the control region ($A_V = 0$) is shown. Right: The shift in colours when seen through a cloud with 4 magnitudes of visual extinction. The orange arrow shows the shift in the centre of the cloud from $A_V = 0$ to $A_V = 4$ mag. The dotted line represents the theoretical shift with increasing extinction assuming a normal reddening law (Rieke and Lebofsky, 1985)

One of the main drawbacks of any extinction based method is that it requires the number of visible background stars per riseau square to be much greater than unity. If regions within the cloud are so dense that they don't let any light from background sources through, the method cannot calculate the amount of extinction along that line of sight. Hence holes appear in the map where the H_2 column density is greatest, i.e. where dense cores are present. Consequently a trade-off must be made between spatial resolution and completeness of a map. For example, if one increases the spatial resolution of a map to smaller and smaller pixel sizes in order to better visualise small scale structures in a cloud, then one must be ready to deal with the holes that will form over the regions of highest density. Conversely if one wants to better model the density distribution of clouds and cores, and therefore requires a complete map, one must be ready to accept that the best resolution will be limited by the density of stars visible through the densest regions of the cloud. For the case of a 2MASS data sample at low galactic latitude (like the one used in this study) the best resolution achievable whilst still maintaining complete map coverage was $75''$ per pixel. The follow-up method by Lombardi (2009), known as NICEST, employs a technique of weights and interpolation in order to improve the accuracy of the extinction values for the regions of highest column density.

2.3. NICER in detail

The NICER method is presented and described in detail by Lombardi and Alves (2001). There are however some points that need to be clarified in order to gain a complete understanding of how to transform colours into extinction values. The main point to be clarified is that NICER does not attempt to find a single extinction measurement for each pointing based on the epicentre of colours in the J-H vs H- K_S diagram as portrayed in Figure 6. Instead the method determines extinction values for each individual star regardless of its position on the map and then groups and averages these pre-calculated extinction values to form an average extinction value for the specific line of sight. In general the line of sight pointing (equivalent to a riseau square) will refer to an approximately $1.5' - 2'$ region of the sky at low galactic latitudes if one is limited by the depth of coverage in the 2MASS catalogue. If deep field observations have been acquired from an observing run dedicated to determining the extinction, then a higher depth of field and hence spatial resolution may be achieved.

2.3.1. Definitions

Here we introduce the terms and expressions used in the NICER method. How these quantities are used by the NICER method is presented in the following section.

\hat{A}_V - The estimated extinction value for each star. As the chance that any individual colour combination will be the “ideal” colour combination (as defined by the dotted line in Figure 6) is almost zero, the estimated extinction is essentially the projection of the colour combination of a star onto this “ideal” line. This value is calculated for each star so that the average for a pointing is not biased by the choice of colour over which one averages.

\mathbf{k} - a vector containing the conversion factor from colour excess to visual extinction for each colour; $\mathbf{k}_i = E(X - Y)/A_V$. For the 2MASS colours, $\mathbf{k}_{J-H} = 1/9.35$ and $\mathbf{k}_{H-K} = 1/15.87$. For our study we used the k-vector, $\mathbf{k} = (0.107, 0.063)$. These values can be calculated from Rieke and Lebofsky (1985).

$Cov(\epsilon)$ - The photometric error covariant matrix. This matrix tracks the reliability of each of the individual bandpass measurements for each star. The extinction towards a star with high uncertainties in the K-band will be calculated with additional weight given to the J and H bands to compensate for the poor measurement in the K_S band. As each photometric measurement is different, this matrix must be calculated for each star individually. In general this is a diagonal matrix with the main diagonal equal to the quadrature of the uncertainties for the two photometric bands associated with each colour and the off-diagonals equal to the negative square of the uncertainty for each individual photometric band. The generalised form which can be used for as many colours as are available is:

$$Cov(\epsilon) = \begin{pmatrix} \sigma_W^2 + \sigma_{X^2} & -\sigma_{X^2} & 0 \\ -\sigma_{X^2} & \sigma_{X^2} + \sigma_{Y^2} & -\sigma_{Y^2} \\ 0 & -\sigma_{Y^2} & \sigma_{Y^2} + \sigma_{Z^2} \end{pmatrix} \quad (16)$$

For our study we used the corresponding 2MASS covariance matrix:

$$Cov(\epsilon) = \begin{pmatrix} \sigma_{J^2} + \sigma_{H^2} & -\sigma_{H^2} \\ -\sigma_{H^2} & \sigma_{H^2} + \sigma_{K_S^2} \end{pmatrix} \quad (17)$$

$Cov(c_{int})$ - The intrinsic scatter covariant matrix. Due to the fact that there are many different spectral types, each with a slightly different combination of colours in the J, H and K_S bands, there is an intrinsic scatter in the colour-colour cloud. This is generally the greater source of error when compared to the photometric errors. This matrix is a static matrix however as it describes the global scatter of colours. It can either be calculated for a specific ‘control’ field located near the region of interest or its values can be taken from previous studies. The matrix itself is the covariance associated with the intrinsic colours and so each element is the **expected value** for two of the colours c_i and c_j of the corresponding matrix element, where i and j

represent the matrix axes and c_i represents all the stars in the control field for that one colour.

$$Cov(c_{int}) = \left(\sum_{i,j=1}^N E(c_i \cdot c_j) \right) = const \quad (18)$$

$$E(c_i \cdot c_j) = \langle c_i \cdot c_j \rangle - \langle c_i \rangle \langle c_j \rangle \quad (19)$$

In our study $c_1 = (J - H)$ and $c_2 = (H - K_S)$. The expected value of each colour product is given as:

$$Cov(c_{int}) = \begin{pmatrix} \langle c_1^2 \rangle - \langle c_1 \rangle^2 & \langle c_1 \cdot c_2 \rangle - \langle c_1 \rangle \langle c_2 \rangle \\ \langle c_1 \cdot c_2 \rangle - \langle c_1 \rangle \langle c_2 \rangle & \langle c_2^2 \rangle - \langle c_2 \rangle^2 \end{pmatrix} = const \quad (20)$$

C_{ij} - The combined covariant matrix. This is the sum of the two intrinsic sources of error in this method; the photometric error and the intrinsic scatter in the colours due to the existence of different spectral types. $C_{ij} = Cov(\epsilon) + Cov(c_{int})$ where the intrinsic colour refers to the epicentre of the colour-colour cloud of stars that suffer little to no extinction. It should be made clear that $Cov(\epsilon)$ and $Cov(c_{int})$ represent two completely different aspects of the method. $Cov(c_{int})$ is a static matrix that is calculated once from the average values of **all** the stars in the control field. Once $Cov(c_{int})$ has been calculated it is effectively a constant. $Cov(\epsilon)$, on the other hand, is a measure of the photometric uncertainty for each star and is a quantity that must be calculated for each star individually. For the case of a 2MASS data set we find:

$$C_{ij} = \begin{pmatrix} \sigma_{J^2} + \sigma_{H^2} + c_{int}^{11} & -\sigma_{H^2} + c_{int}^{21} \\ -\sigma_{H^2} + c_{int}^{12} & \sigma_{H^2} + \sigma_{K_S^2} + c_{int}^{22} \end{pmatrix} \quad (21)$$

where c_{int}^{ij} refers to the matrix elements of the $Cov(c_{int})$ matrix

2.3.2. Our implementation of the NICER method

While implementing the NICER method, we found that a user friendly in-depth explanation of the mechanics behind the NICER method was lacking. Here we present a brief explanation of the method and its application with regards to the 2MASS catalogue in the hope that it will serve as a useful introduction for new entrants into the field of extinction mapping.

The NICER method assumes a linear relationship between colour and visual extinction of the form:

$$c_i^{obs} = c_i^{int} + k_i A_V + \epsilon_i \quad (22)$$

where $c_i^{obs} - c_i^{int} \equiv E(c_i)$ and $k_i = E_i/A_V$. ϵ represents the uncertainty in the colours. A weighted average of all colours used in the analysis will result in an estimate for the extinction towards a star. Mathematically this is expressed as:

$$\hat{A}_V = a + \sum_{i=1}^N b_i \cdot c_i^{obs} \quad (23)$$

where N is the number of 'colours' available in the analysis and a and b are determined by the photometric errors for the stars. For our case, which uses the available 2MASS colours, the extinction estimator is:

$$\hat{A}_V = a + b_{JH}(J - H)_{obs} + b_{HK}(H - K_S)_{obs} \quad (24)$$

According to Lombardi and Alves (2001) there are two conditions that need to be placed on the coefficients in order to ensure that the estimator is unbiased and has a minimum variance. These two conditions are:

$$\sum_{i=1}^N b_i k_i = 1 \quad (25)$$

$$a + \sum_{i=1}^N b_i \langle c_i^{int} \rangle = 0 \quad (26)$$

The solution to the minimisation of the variance in the estimator is reduced to only the coefficients b_i .

$$b = \frac{C_{ij}^{-1} \cdot k}{k^T \cdot C_{ij}^{-1} \cdot k} \quad (27)$$

By combining Equations (23) and (26) the optimal estimator for the extinction is:

$$\hat{A}_V = \sum_{i=1}^N b_i \cdot [c_i^{obs} - \langle c_i^{int} \rangle] \quad (28)$$

For the purposes of our study we applied this method to a 2MASS dataset which covers the bands J, H and K_S and the colours J-H and H- K_S . Therefore our final equation for the extinction estimator applied to the case of 2MASS was:

$$\hat{A}_V = \frac{(Cov(c_{int}) + Cov(\epsilon))^{-1} \cdot k}{k^T \cdot (Cov(c_{int}) + Cov(\epsilon))^{-1} \cdot k} \begin{pmatrix} E(J - H) \\ E(H - K_S) \end{pmatrix} \quad (29)$$

For a small data sample the above formula is a neat and elegant programmable solution for the extinction estimator. However for the case where a data set contains many hundreds of thousands of stars, the time needed to compute $2N$ inverse matrices becomes prohibitive. Therefore we took it upon ourselves to optimise the matrix component of the optimal estimator equation. As we were dealing with 2MASS data

finding the inverse covariance matrix was trivial. The presence of the inverse combined covariant matrix, C_{ij} , in both the numerator and denominator meant that the determinants cancelled each other out, leaving only the adjunct matrix of C_{ij} . This small simplification removed the need for a time-intensive inverse matrix operation⁵. Furthermore by using the subset of data depicted in Figure 5 we derived the constants for the intrinsic scatter covariant matrix. Our final equation for the extinction estimator is:

$$\hat{A}_V = \frac{\begin{pmatrix} \sigma_{H^2} + \sigma_{K_S^2} + c_{22} & \sigma_{H^2} - c_{21} \\ \sigma_{H^2} - c_{12} & \sigma_{J^2} + \sigma_{H^2} + c_{11} \end{pmatrix} \cdot k}{k \cdot \begin{pmatrix} \sigma_{H^2} + \sigma_{K_S^2} + c_{22} & \sigma_{H^2} - c_{21} \\ \sigma_{H^2} - c_{12} & \sigma_{J^2} + \sigma_{H^2} + c_{11} \end{pmatrix} \cdot k} \begin{pmatrix} J - H - 0.49 \\ H - K_S - 0.13 \end{pmatrix} \quad (30)$$

where $c_{11} = 0.0281$, $c_{12} = c_{21} = 0.0029$ and $c_{22} = 0.0277$ and $k = (0.107, 0.063)$. The variance for the estimator is given by the simple relation: $Var(\hat{A}_V) = b \cdot C \cdot b$. This method also has the cute built in check that $b \cdot k$ must equal unity. If the product $b \cdot k$ doesn't equal unity for all stars then the implementation should be scrutinized thoroughly. In other words, Belgium⁶.

2.3.3. Star selection and pixel binning

In order to determine which areas of the sky needed to be mapped in extinction, we developed an algorithm which read in the available radio line data for ^{13}CO and $C^{18}O$ (Goldsmith et al., 2008, Hacar et al., 2013) and built up a catalogue of $1^\circ \times 1^\circ$ patches of the sky for which the Infrared Science Archive's GATOR search engine was queried. Stars were downloaded from the 2MASS point source catalogue (Skrutskie et al., 2006) using Astroquery, an affiliated Astropy package (Astropy Collaboration et al., 2013). These were downloaded automatically in $1.1^\circ \times 1.1^\circ$ patches so as to avoid missing any stars falling in between the patches. These individual patches were then combined and grouped by their individual 2MASS identifiers. Double entries were removed from the list⁷.

⁵A quick comparison of the calculation with and without the inverse matrix operation for the whole sample of approximately 578,000 stars showed a speed up of approximately 380x, reducing the computational time to a triviality.

⁶For those familiar with the works of Douglas Adams - "On Earth, Belgium refers to a small country. Throughout the rest of the galaxy, Belgium is the most unspeakably rude word there is."

⁷The NICER method takes the average of the extinction calculated for each star in a pixel. As there are generally many stars in a single pixel, several doubled up stars wouldn't skew the final average extinction for that pixel very much. In the other extreme where a pixel lies well within the overlapping region, most stars would be doubled. As most stars are doubled, the average value would still be the expected value, because twice as many extinction values are being divided by twice as many stars, resulting in the expected value. Either of these two cases is valid for the vast majority of pixels affected by the overlap. Therefore we maintain that the doubling of stars in pixels due to the overlapping regions covered by

Strict selection criteria were placed on the catalogue to filter out stars with questionable detections. We only used stars with quality flags equal to A for at least 2 bands (Skrutskie et al., 2006). The reduced sample (55% of the $\approx 5 \times 10^5$ catalogue of stars for the whole L1495 region) was still more than adequate for our needs. This kept photometric uncertainty for individual stars below 1% for our whole selection. The published 2MASS magnitudes were accompanied by a "goodness of fit" read-flag which described which method was used to determine the apparent magnitude (PSF fitting in 1D or 2D, aperture photometry, etc). We only selected the stars with a read-flag of 1, 2 or 3, corresponding to a fit based on aperture photometry, 2D profile fit or 1D profile fit for bright stars. The fact that the photometric errors in the 2MASS catalogue were O(1%) meant that the majority of the uncertainties involved in this study originated from the determination of the extinction, not from the photometric measurements.

In order to determine which stars belonged to which ^{13}CO or $C^{18}O$ pixel, each star was given a pixel identifier based on its R.A. and Dec coordinates. The sample of 578,000 stars were then sorted according to their allocated pixel identifier. Stars with the same identifier were grouped and their individual extinctions (as per the NICER method) averaged. To increase the accuracy of the extinction values, the pixels were Nyquist sampled with an effective beam-width of $75''$ and weights were assigned based on a star's distance from the centre of the pixel. The final extinction map for the 120 square degrees can be seen in Figure 1. The uncertainties for each pixel were calculated based on the variance in extinction values across all stars included in a pixel ($Var(A_V) = b \cdot C_{ij} \cdot b$).

2.4. Extinction maps used in this study

Due to the intrinsic requirement of the NICER method for more than one star per pixel and the limits on the depth of coverage of the 2MASS catalogue ($\sim 15^m$ in K_S -band), the resolution of the map was restricted to $75''$ FWHM. At resolutions lower than this, our implementation of the NICER method was unable to determine the extinction measurements for the starless dense core regions inside B7/B10 and B211/B213. The result of our NICER pipeline is shown in Figure 1 and our region of interest, the complex L1495-B213, is described in Figure 2. In order to determine the accuracy of our extinction map, we compared it with the extinction map of Taurus generated by Lombardi et al. (2010). Figure 7 presents both our map (NICER) and

the star tables in the vast majority of cases does not alter the outcome significantly. We have however decided to remove any doubles in order to address the minority cases where a pixel falls exactly on the border of two overlapping regions. In this case, only around half of the stars would be doubled, which would skew the subsequent extinction value towards the average of the doubled stars.

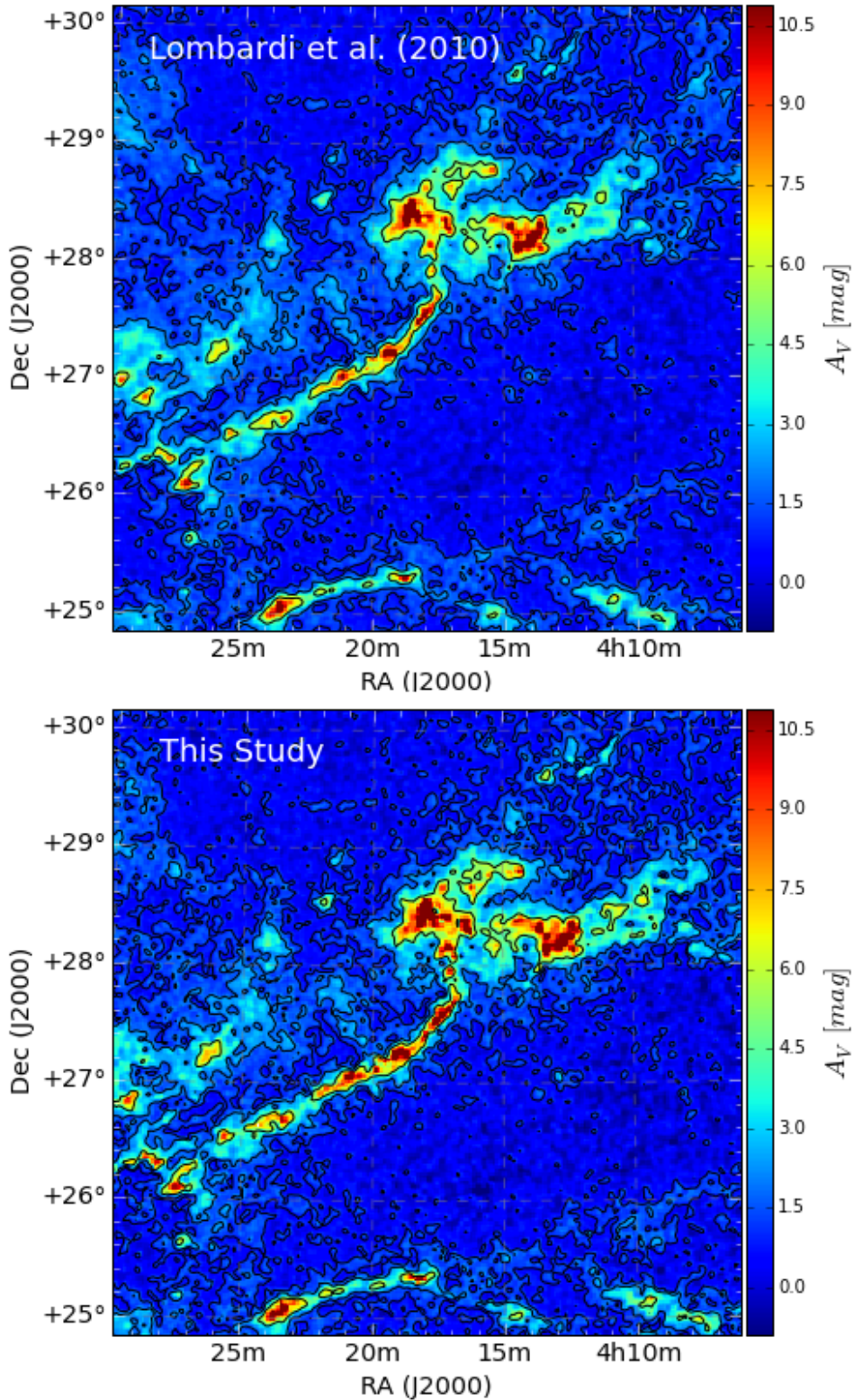


Figure 7: Top: A section of the extinction map as published by Lombardi et al. (2010) with a beam-width of $150''$. Bottom: Our extinction map with a beam-width of $75''$. Contours in both maps are set to $A_V = [1^m, 2^m, 5^m]$ in order to help the eye differentiate between the diffuse background material (dark blue - $A_V < 1^m$), the envelope of the cloud (light blue and turquoise - $1^m < A_V < 5^m$) and the dense regions (yellow and red - $A_V > 5^m$). The increased noise in our map is due to the higher resolution.

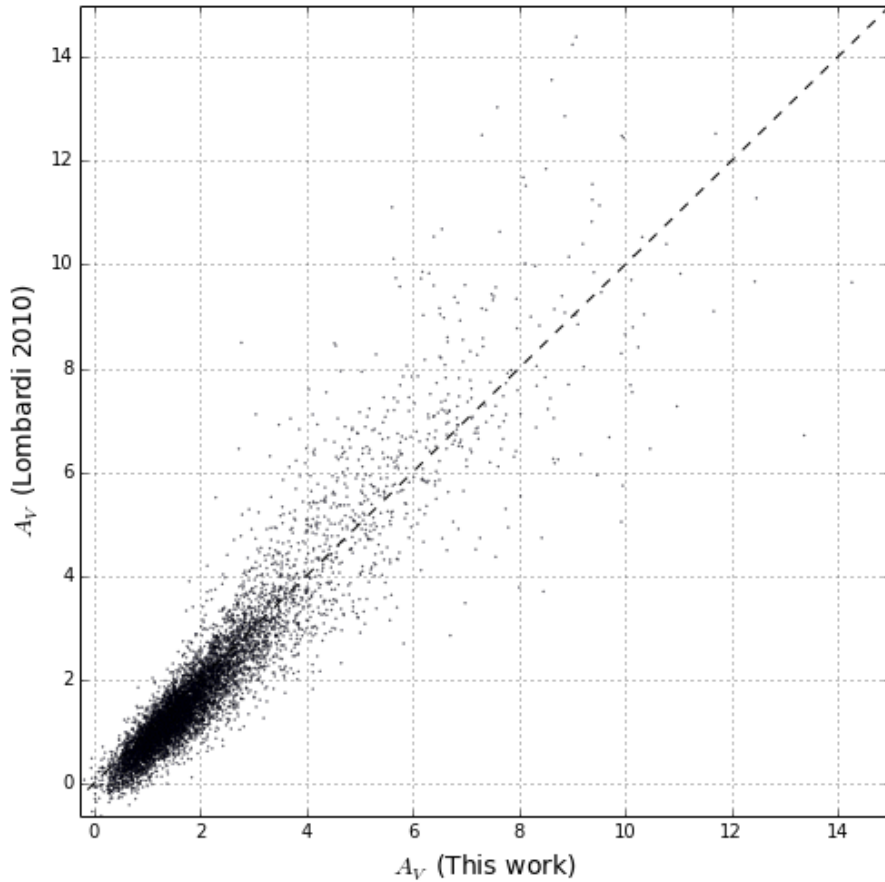


Figure 8: A comparison of the extinction map generated by the author using the NICER method and the extinction map published by Lombardi et al. (2010) of the same region using the NICEST method. The dotted line is the one-to-one correlation. The difference between the two maps is due to the slightly different methods and grid spacing used to generate the maps (NICER vs NICEST) and is consistent with the comparison conducted by Majewski et al. (2011)

Lombardi et al. (2010) (NICEST). Figure 8 shows that there was a good correlation between the two maps, even though the results were not identical. A best fit to the data revealed that NICER slightly overestimated the extinction at low values ($\sim 0.3^m$ around $A_V = 0$) and slightly underestimated the extinction at high values.

The advantage of NICEST over NICER is that it models the densest regions of the clouds much better. Therefore the NICEST map would be more useful for constraining the $^{13}CO - A_V$ and $C^{18}O - A_V$ relationships in the high density ($A_V > 5$) regions. Furthermore the NICEST map published by Lombardi et al. (2010) has been used in other studies and could count as a standard "reference" map. Due to the good correlation between our NICER map and the NICEST map of Lombardi et al. (2010) (Figure 7) we were confident that the extinction values generated using our own

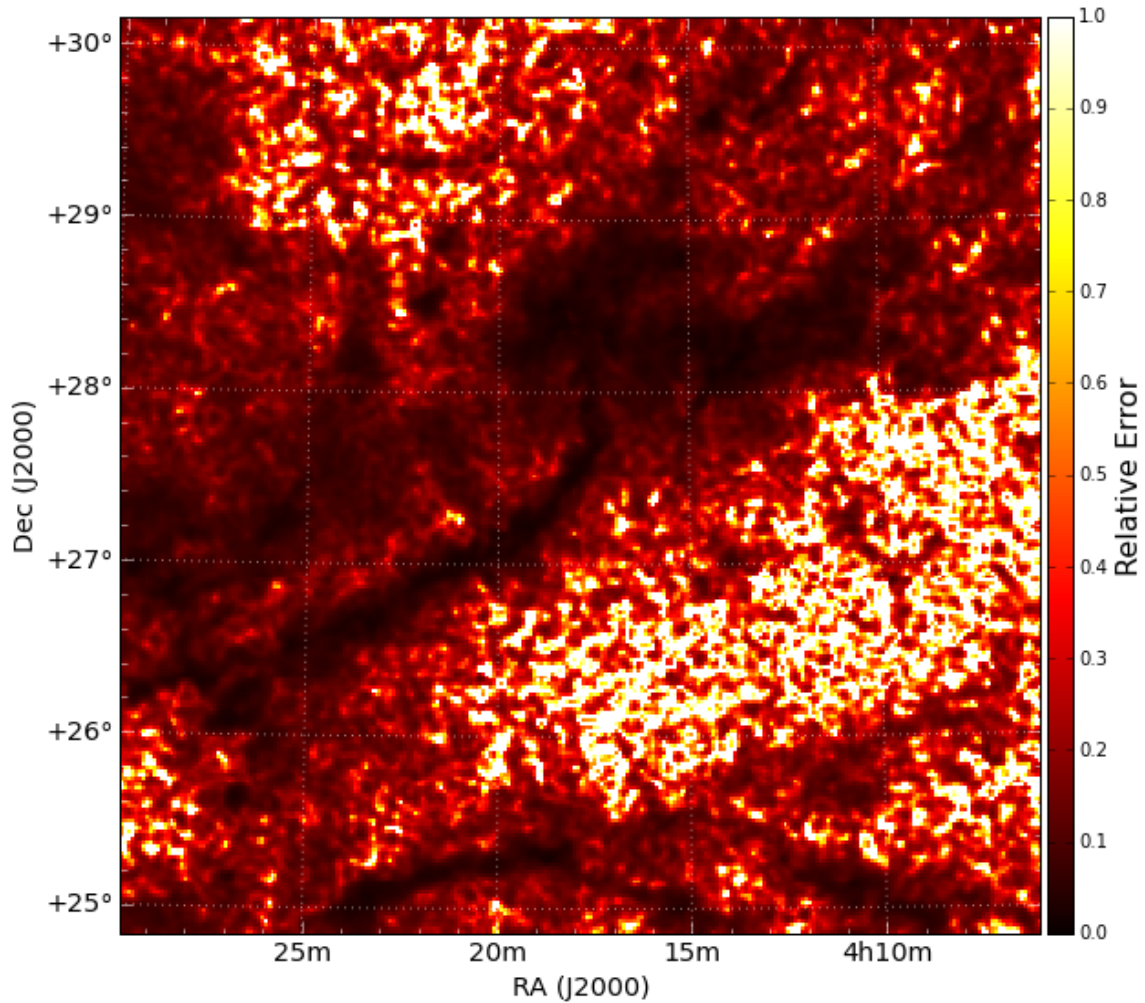


Figure 9: The relative uncertainties for A_V from Lombardi et al. (2010). The majority of uncertainties for any line of sight was 0.43 magnitudes. This was found to be in B7 and corresponded to an extinction value of $A_V = 18^m$.

pipeline represented the true line-of-sight extinction.

As each measurement in the extinction map is the weighted average of the extinction towards numerous stars, it is natural that there will be variations within the group of stars used in each pixel. Sources of these variations include (but are not limited to) cloud structure at a sub pixel scale and intrinsic differences in the sample of background stars and at higher extinctions bias towards giant stars in the background star sample. Photometric uncertainties, as discussed above, can be discounted as a large source of error, as they are on average more than an order of magnitude less significant than the errors invoked by using the NICER method.

Figure 9 shows the average uncertainty for each pixel in our region of interest. When compared to the uncertainties used in Lombardi et al. (2010) the difference is neg-

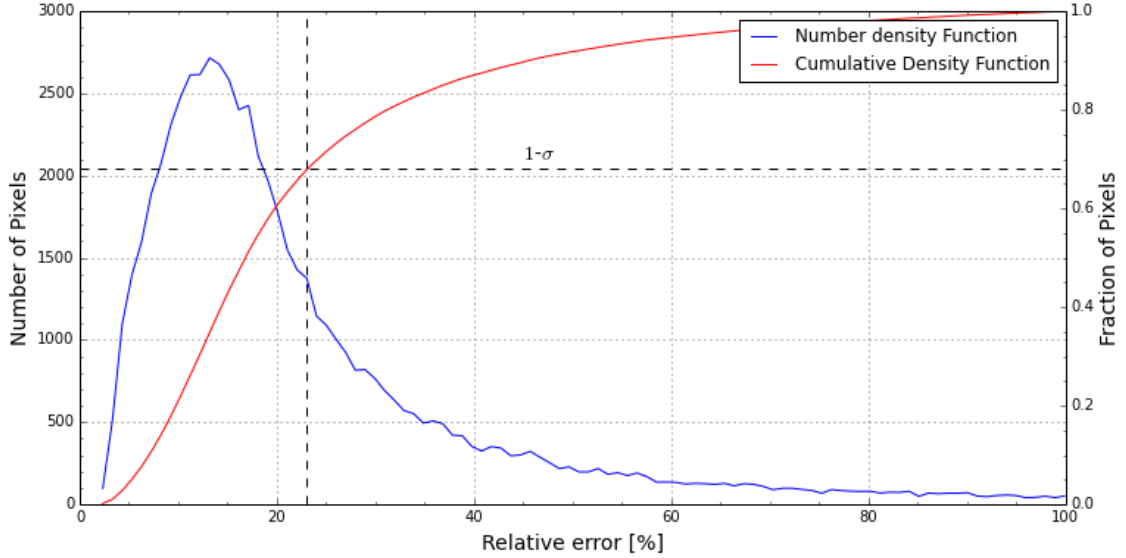


Figure 10: Actual and cumulative distributions of the relative uncertainties associated with each pixel in the extinction map. For this study we have adopted a nominal 1σ error of 23% for the extinction values.

ligible. The vast majority of the map has an extinction uncertainty of less than 0.2 magnitudes. In the densest regions where extinction is at its highest, there may only be a few stars visible for the determination of the extinction value for that pixel. Consequently the uncertainty is higher. However, the greatest uncertainty is 0.43 magnitudes and corresponds to a pixel at the very centre of the B7 region with an extinction of $A_V = 18^m$. All pixels with uncertainties above 0.4 magnitudes correspond to extinction measurements greater than 15 magnitudes and are a result of the small number of stars available for determining the extinction. More important for the sake of the study are the relative uncertainties. The main source of large relative (i.e. $> 50\%$) uncertainties are associated with the sparse medium ($A_V < 1^m$) when photometric uncertainties dominate. In these regions the average uncertainty is on the same order as the average uncertainty, $\sigma_{A_V} \approx A_V \approx 0.2^m$. Figure 10 shows that 68% of points have relative uncertainties of less than 23%.

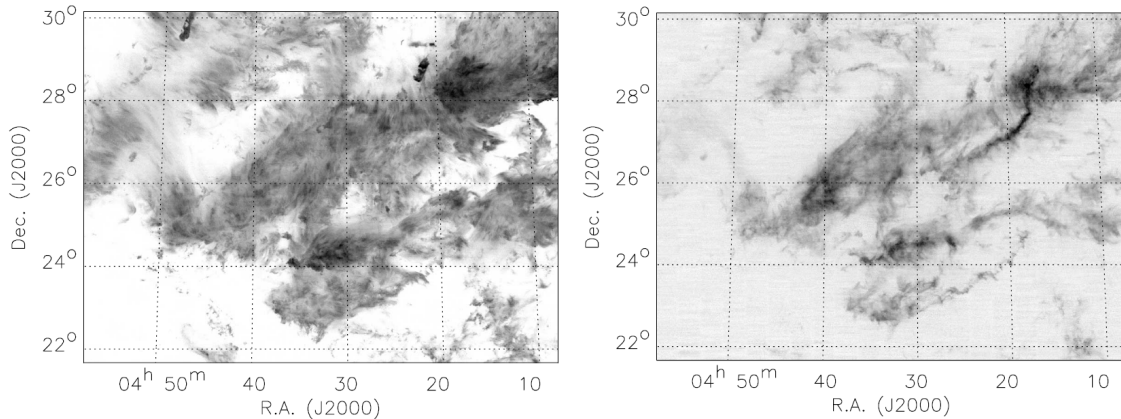


Figure 11: Left: The Taurus molecular cloud in ^{12}CO . Right: The same region in ^{13}CO . This comparison illustrates the short optical depth of ^{12}CO compared to the depth of the cloud and why it cannot be used to probe the interior structure of molecular clouds (images from Goldsmith et al., 2008).

3. Column densities of ^{13}CO and $C^{18}O$ and their role in determining $N(H_2)$

While extinction is the most direct way to determine the dust column density (and by extension $N(H_2)$), its accuracy is limited by the number of background stars. This is primarily due to the fact that it requires the vast majority of stars to be *behind* the cloud itself. The farther away the cloud is, the more stars appear in the foreground, contaminating the extinction estimates. Even if one removed all the known foreground stars from a region, the accuracy is still limited by the depth of the observations. For example, using 2MASS to determine the extinction of a cloud at $D = 1kpc$, the deepest extinction value attainable is $A_V = 20^m$ ⁸. This will however not be the case for the majority of stars, so the best column density measurements of the cloud will be severely less than $A_V = 20^m$. Extinction-based methods are also limited (generally to the arc-minute scale) by the amount of visible background stars. This limits the usefulness of these absorption based methods to clouds near the galactic plane (and inside the Milky Way). An answer to all these problems is to use the emission from a tracer molecule as a proxy for H_2 . The logical choice is the next most abundant species in the ISM: CO .

The atomic weight difference between carbon and oxygen means that the molecule has a weak dipole moment and hence low energy rotational transitions. The lowest rotational transition ($J=1 \rightarrow 0$) emits at a wavelength of 2.6mm (110GHz - Cord et al., 1968) and is easily excited at the low temperatures [O(10K)] found in cold molecular

⁸This is assuming that all stars are (H,K)=10 at 1kpc (i.e. A0V) and that they are detected at the limit of 2MASS sensitivity (i.e. (H,K)=(15,14) mag).

clouds. Fortunately the emission lines fall within an atmospheric transmission window and so CO has become the "workhorse" for tracing the dense ISM⁹ (Dame et al., 1987).

The relative ubiquity of CO in molecular gas is both a blessing and a curse. The high relative abundance ($N(CO)/N(H_2)$) compared to all other molecules means that emission from the most abundant isotopologue, $^{12}C^{16}O$, saturates at relatively low H_2 column densities. Figure 11 shows how $^{12}C^{16}O$ (henceforth referred to as CO) reveals information about the surface of clouds, but very little about the deeper structure. This is an important property for tracing the distribution of H_2 in the diffuse ISM ($A_V < 5^m$) as this is where the majority of the H_2 mass resides. For dense ($A_V > 5^m$) clouds, however, this essentially renders CO useless. Thankfully there are other species of CO which are less abundant and therefore less opaque at greater column densities, namely: $^{13}C^{16}O$ and $^{12}C^{18}O$, which will be referred to as ^{13}CO and $C^{18}O$ for the remainder of the study. According to Wilson and Rood (1994) these isotopologues are 77 and 560 times less abundant than CO respectively, making them much better tracers of the denser regions of the ISM. ^{13}CO for example typically saturates at around $A_V = 5$ and $C^{18}O$ at a much higher density still. The disadvantage is that because they are less abundant, they also produce less emission and are therefore more difficult to detect.

Naturally there are other considerations when using the rarer CO isotopologues. Naked ^{13}CO and $C^{18}O$ molecules are dissociated by the UV component of the interstellar radiation field and therefore need to be shielded by a certain column density worth of dust¹⁰ before they are able to stably exist (van Dishoeck and Black, 1988). Furthermore, the (generally) linear relationship between $C^{18}O$ and H_2 is interrupted at high volume densities ($O(10^4 \text{ cm}^{-3})$) by the depletion of $C^{18}O$ molecules onto dust grains in the central regions of cores. Regardless of these limitations the isotopologues of CO still provide a much greater spatial (sub-arcmin) resolution for the mapping of column densities than most extinction-based method .

3.1. Determining CO column densities

Even at the low temperatures [$O(10\text{K})$] found in molecular clouds, CO molecules exist in several of the least energetic rotational states ($J = 0, 1, 2\dots$). The kinetic energy of the particles is transformed into internal rotational energy via collisions between the molecules. Higher energy rotational states are however unstable and will decay,

⁹In the context of this study "dense" gas refers to regions with $A_V > 5^m$

¹⁰The so-called "turn on" values are around $A_V \approx 0.7^m$ and $A_V \approx 1.2^m$ for ^{13}CO and $C^{18}O$ respectively according to van Dishoeck and Black, 1988

either through stimulated or spontaneous emission of a photon, down to the lowest possible energy state. The spontaneous decay rates for the $J = 1 \rightarrow 0$ transition for ^{13}CO and $C^{18}O$ are on the order of 6 months (See Table 2). It is these photons that allow us to observe the presence of the various CO isotopologues.

The strength of emission from a cloud is based on two variables: The number of molecules and the population of molecules in each energy state. The population of molecules in each of the rotational states is determined by the excitation temperature of the cloud, T_{ex} , and follows a Boltzmann distribution, assuming the gas is in a state of local thermal equilibrium (LTE).

$$\frac{N_j}{N} = \frac{g_j}{Q} \cdot e^{-E_{ij}/kT_{ex}} \quad (31)$$

where N_j is the amount of particles in state j and N is the total amount of particles. g_j is the degeneracy of the state j , E_{ij} is the energy difference between states and Q is the partition function $Q = \sum_{j=0}^{\infty} g_j e^{-E_{ij}/kT_{ex}}$ which for temperatures around 10K can be approximated as a linear function of T_{ex} ¹¹. The linear equations are given in Table 2 (See Rohlfs and Wilson, 2004 for a discussion on the partition function.)

Equation (31) gives the ratio of molecules in state j compared to the total number of molecules. Therefore, we can infer the total amount of molecules by measuring the emission from a single transition. However the amount of radiation that actually leaves the cloud is completely dependent on the optical depth of the cloud, τ_ν . The change in emission is given by the fundamental radiative transfer equation:

$$\frac{dI}{ds} = -\kappa I + \epsilon \quad (32)$$

where κ is the absorption coefficient of the cloud and is related to the optical depth, ϵ is the emission from a population of molecules, I is the intensity of emission and ds is the path length. By demanding that the change in intensity, I , is zero and that the gas is described by Planck's law, Equation (32) becomes:

$$\frac{\epsilon}{\kappa} = \frac{2h\nu^3}{c^2} \frac{1}{e^{h\nu/kT} - 1} \quad (33)$$

The conversion from absorption κ and emission ϵ to our case specific quantities of optical depth τ and upper-level population N_j is given in Rohlfs and Wilson (2004) and so won't be given here. It suffices to say that the condition of LTE allows the calculation of the upper level population using the following relationship:

$$N_j = \frac{8\pi\nu_{ij}^3}{c^3} \frac{1}{A_{ij}e^{h\nu_{ij}/kT} - 1} \int \tau_\nu d\nu \quad (34)$$

¹¹Appropriate values for $Q(T_{ex})$ can be found on the University of Köln's website - <http://www.astro.uni-koeln.de/cdms/entries>.

where A_{ij} is the Einstein coefficient for the decay from state j to i . By combining Equations (31) and (34), we obtain the following relationship for the total population of molecules, N :

$$N = \frac{8\pi\nu_{ij}^3 Q}{c^3 g_j A_{ij}} \frac{e^{-E_{ij}/kT_{ex}}}{e^{h\nu_{ij}/kT} - 1} \int \tau_\nu d\nu \quad (35)$$

We have an equation based on two factors. The excitation temperature T_{ex} and the optical depth τ_ν . By once again using the radiative transfer equation (Rohlfs and Wilson, 2004) we can convert the optical depth into the observable quantity of line temperature (or intensity), $T_{L,\nu}$:

$$T_{L,\nu} = (J(T_{ex}) - J(T_{bg}))(1 - e^{-\tau_\nu}) \quad (36)$$

where $J(T) = \frac{h\nu/k}{e^{h\nu/kT} - 1}$ and T_{bg} is taken to be the universal background temperature, $T_{bg} = 2.7K$. There are two limiting cases that need to be addressed here: When the cloud is optically thick ($\tau_\nu \gg 1$) and when the cloud is optically thin ($\tau_\nu \ll 1$). If we take the optically thick case ($\tau \gg 1$), the line temperature becomes: $T_{L,\nu} = (J(T_{ex}) - J(T_{bg}))$ which doesn't tell us anything about the total population, N , inside the cloud. However if we take the optically thin case ($\tau \ll 1$), the line temperature can be approximated by: $T_{L,\nu} = (J(T_{ex}) - J(T_{bg})) \cdot \tau_\nu$. By integrating the antenna temperature over the whole frequency range in the optically thin case we arrive at an expression for the optical depth:

$$\int \tau_\nu d\nu = \frac{\int T_{L,\nu} d\nu}{(J(T_{ex}) - J(T_{bg}))} \quad (37)$$

By combining Equations (37) and (35) we arrive at an expression that can be used to determine the column density of a molecule based on the excitation temperature, T_{ex} and observed line temperature $T_{L,\nu}$:

$$N = \frac{8\pi\nu_{ij}^3 Q}{c^3 A_{ji}g_j} \frac{e^{E_{ij}/kT_{ex}}}{e^{h\nu_{ji}/kT_{ex}} - 1} \frac{\int T_{L,\nu} d\nu}{J(T_{ex}) - J(T_{bg})} \quad (38)$$

where $J(T) = \frac{h\nu/k_B}{e^{h\nu/k_B T} - 1}$. This equation combines the physics of the micro-scale (the states of the individual molecules) with the macro-scale (the micro-scale conditions averaged over the region covered by the beam of the telescope) under the assumptions of LTE and optical thinness. In simplistic terms equation (38) can be broken up into three main parts: The column density, $N(X)$, the integrated emission, $\int T_{L,\nu} d\nu = W(X)$, and the conversion factor $f(T_{ex})$:

$$N(X) = f(T_{ex}) \cdot W(X)$$

The conversion factor $f(T_{ex})$ is dependent purely on two functions of the excitation temperature: $J(T_{ex})$ and $Q(T_{ex})$. A series expansion approximation of $J(T_{ex})$ results

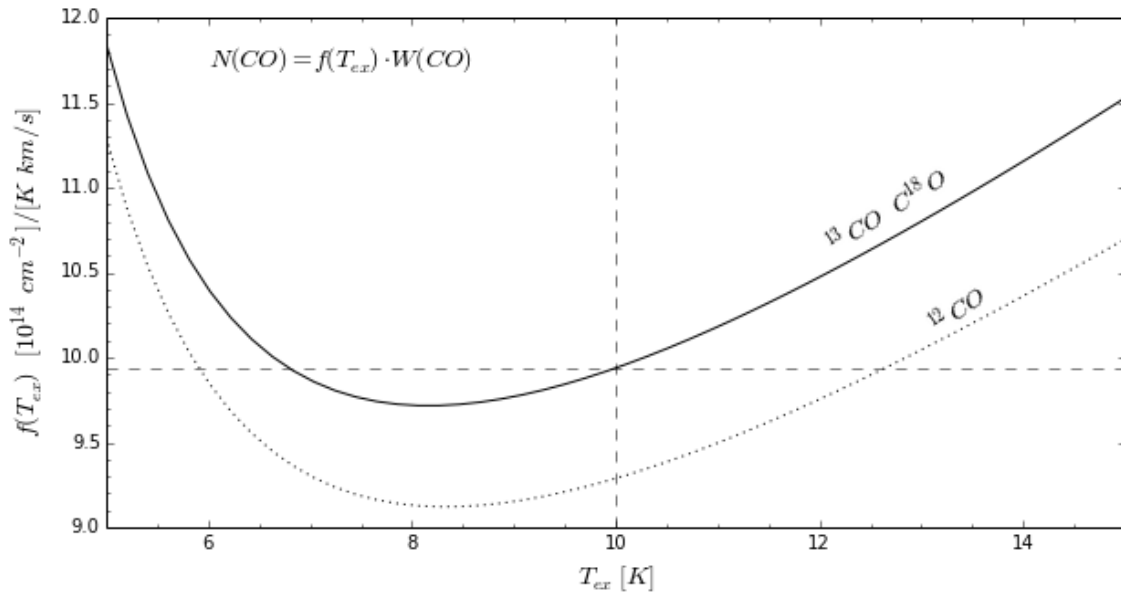


Figure 12: The factor, $f(T_{ex})$, which converts integrated line intensity ($W(X)$) into a column density ($N(X)$) is dependent on the excitation temperature: $N(CO) = f(T_{ex})W(CO)$. The factor changes by 7% over the range $T=[6,12]K$. For our study we assumed a global $T_{ex} = 10K$, giving us conversion factors of $\approx 9.9 \cdot 10^{14}$ for both ^{13}CO and $C^{18}O$. The dotted line represents the conversion factor for ^{12}CO and the solid line for ^{13}CO and $C^{18}O$.

in a $1/T_{ex}$ law for temperatures $T_{ex} < 8K$ and a linear approximation for temperatures $T_{ex} > 10K$. This combined with the partition function, $Q(T_{ex})$, means that $f(T_{ex})$ accounts for the increased emission from a hotter gas and the decrease in emission due to the changing rotational level populations that occur with an increase in temperature.

Using the constants given in Table 2 we calculated the conversion factors, $f(T_{ex})$, for ^{13}CO and $C^{18}O$ to be approximately $9.9 \cdot 10^{14}$ molecules per cm^2 per $K km/s$ for an excitation temperature of $10K$. The exact values are given in Table 2. For our study we have assumed a global excitation temperature of $10K$ because we only had integrated line intensities for the $J = 1 \rightarrow 0$ transition. Pineda et al. (2010) have shown the ^{12}CO temperature of L1495-B213 to be approximately $10K^{12}$ and so we have also assumed this to be the excitation temperature for ^{13}CO and $C^{18}O$. The use of higher energy transition lines, where available, would allow us to determine the relative level populations more accurately and hence the excitation temperature throughout the cloud. Figure 12 shows that these conversion factors don't change by

¹²Pineda et al. (2010) shows that for the regions in Taurus where ^{12}CO is detected 68% of data points have an excitation temperature in the range $7K < T_{ex} < 12K$ and 97% of the points have excitation temperature in the range $5K < T_{ex} < 13K$.

Parameter	^{12}CO	^{13}CO	$C^{18}O$
ν ($J = 1 \rightarrow 0$) [GHz]	115.271	110.201	109.782
T_{ex} [K]	10.0	10.0	10.0
A_{ij} [s^{-1}]	$7.203 \cdot 10^{-8}$	$6.294 \cdot 10^{-8}$	$6.27 \cdot 10^{-8}$
$E_{1,0}$ [K]	5.53	5.29	5.27
g	3	6	3
$Q(T_{ex})$	$0.36(T_{ex} + 1.03)$	$0.76(T_{ex} + 0.97)$	$0.38(T_{ex} + 0.97)$
$f(T_{ex})$ [$cm^{-2}/(K km/s)$]	$9.287 \cdot 10^{14}$	$9.937 \cdot 10^{14}$	$9.919 \cdot 10^{14}$

Table 2: Natural constants required to determine the conversion factor between integrated line intensity and column density in Equation (38). The final conversion factors, $f(T_{ex})$, assume an excitation temperature of $T_{ex} = 10K$. These constants can be found on the university of Köln’s website: <http://www.astro.uni-koeln.de/cdms/entries>

more than 7% over the range $T_{ex} = [6, 12]K$.

3.2. ^{13}CO and $C^{18}O$ maps

The ^{13}CO maps used in this study are based on the integrated intensity data obtained between November 2003 and May 2005 with the FCRAO 14m millimeter-wave telescope. A full description of the data acquisition and reduction process is provided in Goldsmith et al. (2008). The $C^{18}O$ data was also obtained using FCRAO 14m and is described in Hacar et al. (2013). While the full data set contains a great deal of information on the velocity structure of the cloud complex, we have only used the integrated flux intensities for the two molecular lines: ^{13}CO and $C^{18}O$. The reason for this is that we were primarily interested in the total abundances of each of the CO isotopologues and therefore only the total flux was of importance. The corresponding maps are shown in Figure 13 (Left: Middle and Bottom), Figure 14 (Centre) and in Appendix A (A.1.2, A.1.3 and A.2.2).

The full-width-half-maximum (FWHM) of the beams in the original maps was $45''$. Due to the resolution constraints of the extinction mapping technique, namely a FWHM of $75''$, the integrated intensity maps were re-sampled to match this FWHM (i.e. pixel width of $37.5''$). This facilitated an easier comparison with the extinction data. We transformed the integrated intensity values, $W(^{13}CO)$ and $W(C^{18}O)$, into column density values by using the constants given in Table 2. The conversion factors used were $9.937 \cdot 10^{14} cm^{-2}/(K km/s)$ for ^{13}CO and $9.919 \cdot 10^{14} cm^{-2}/(K km/s)$ for $C^{18}O$. Uncertainties in the integrated ^{13}CO and $C^{18}O$ emission maps were taken from the sources, namely Goldsmith et al., 2008 and Hacar et al., 2013. The r.m.s. noise

per pixel of $\sigma(W(^{13}CO)) = 0.18$ K km/s is given by Goldsmith et al., 2008. The rms noise per pixel of $\sigma(W(C^{18}O)) = 0.5$ K km/s is given by Hacar et al., 2013. These were on the order of 1% and 10% respectively for the maximum values in each data set.

4. Mapping ^{13}CO and $C^{18}O$ versus A_V

In order to better visualise the correlation between A_V , ^{13}CO and $C^{18}O$, we plotted all three column density maps (Figure 13, left side) as well as the corresponding abundances - i.e. one column density divided by another (Figure 13, right side). In this section we present a qualitative description of the spatial distribution of the variations and features in these maps. A quantitative comparison of each of these maps will be presented in Section 6 along with our determination of the numerical relationship between A_V , ^{13}CO and $C^{18}O$. In general, we will refer to 3 different extinction regimes throughout this section. Unless otherwise stated, they are: sparse ($A_V < 1^m$), diffuse ($1^m < A_V < 5^m$) and dense ($5^m < A_V$).

4.1. Relationship between ^{13}CO , $C^{18}O$ and A_V inside the L1495-B213 filament

4.1.1. Extinction, A_V

The top right panel of Figure 13 shows the extinction map of the L1495-B213 filament. The lowest contour is set to $A_V = 2^m$ in order to highlight the border to the sparse surrounding ISM. The highest contour is set to $A_V = 5^m$ in order to show the regions of densest gas. The borders between all the sub-regions as described by Barnard et al. (1927) are clearly visible, except for the distinction between B211 and B213. The filamentary structure of L1495 is clear when one takes the $A_V = 2^m$ boundary, implying that it is one coherent structure in space.

4.1.2. ^{13}CO column density and abundance

As can be seen from a brief glance at the middle panels in Figure 13, the relationship between extinction, A_V and the $N(^{13}CO)$ is far from constant. Peaks in extinction are generally more discrete compared to the long drawn out region of peak emission in ^{13}CO . The continuity of the peak ^{13}CO emission can be explained by the increase in opacity to the point of saturation of the emission. This has the effect that any column density fluctuations on a scale $A_V > 5^m$ are invisible in ^{13}CO emission. The region of high extinction in the head of B7 anti-correlates with the region of peak emission. This is quite apparent when looking at the $X(^{13}CO)$ abundance map (Figure 13, middle right) where the blue holes in the abundance correlate with the highest region of extinction. This behaviour can once again be attributed to the fact that ^{13}CO emission saturates at $A_V > 5^m$ and so while the increase in H_2 column density is visible continues linearly with A_V , the extra emission from a higher $N(^{13}CO)$ remains trapped inside the cloud. The highest ^{13}CO abundance exists on the south side of the B211 part of the filament, not along the ridge of peak ^{13}CO emission. ^{13}CO emission is also visible along the whole filament near the edges where the extinction is low ($A_V < 2^m$).

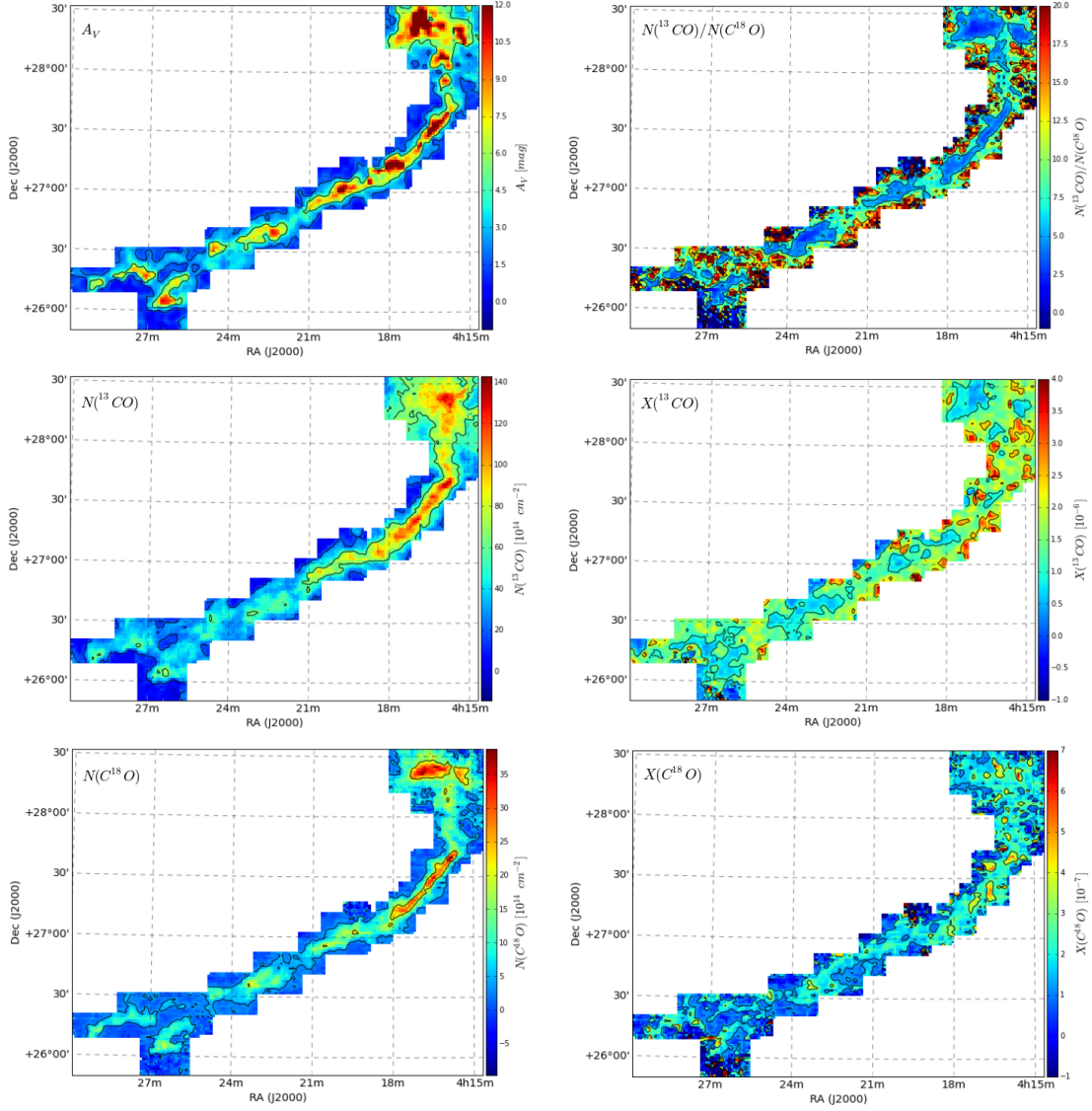


Figure 13: Overview of the L1495-B213 Filament. Full page versions of the individual maps are in Appendix A for clarity (A.1). This figure is solely intended to serve as a tool for a spatial comparison between the main feature in each view of the filament. For example, one can clearly see that the peaks in $X(^{13}CO)$ do not correlate with the peaks in $N(^{13}CO)$. The ^{13}CO and $C^{18}O$ abundance contours are 66% and 150% of the average literature value. The A_V contours correspond to the limits where both ^{13}CO and $C^{18}O$ emission is optically thin.

(Left, Top): Extinction, A_V . Contours: $A_V = [2, 5]$ mag.

(Left, Middle): $N(^{13}CO)$ Column Density. Contours: $[20, 60] \cdot 10^{14} \text{ cm}^{-2}$.

(Left, Bottom): $N(C^{18}O)$ Column Density. Contours: $[4, 20] \cdot 10^{14} \text{ cm}^{-2}$.

(Right, Top): $X(^{13}CO/C^{18}O)$ Isotopologue Ratio. Contours: $[6, 12]$.

(Right, Middle): $X(^{13}CO)$ Abundance. Contours: $[1, 2.25] \cdot 10^{-6}$.

(Right, Bottom): $X(C^{18}O)$ Abundance. Contours: $[1.33, 3] \cdot 10^{-7}$.

4.1.3. $C^{18}O$ column density and abundance

The $C^{18}O$ column density ($N(C^{18}O)$, Figure 13 left, bottom) mirrors the high extinction regions much more closely than $N(^{13}CO)$. This is confirmed by the fact that the abundance of $C^{18}O$ with respect to H_2 ($X(C^{18}O)$ - Figure 13, right bottom), remains largely constant along the whole filament, even though local maxima in the column density exist. Compared to ^{13}CO the abundance of $C^{18}O$ is also more stable along the central part of the filament. The higher extinction values along the filament provide enough shielding from the ISRF for $C^{18}O$ to survive. The dark blue areas in the $X(C^{18}O)$ map (bottom, right) are indicative of either an ISM that is not dense enough to provide adequate shielding or regions of low column density. Islands in $N(C^{18}O)$ are seen in B216, B217 and B218 corresponding to the peaks seen in the extinction map (Figure 13 left, top). An excess of $C^{18}O$ is seen in the B211 sub-region as well as for parts of the B7 and B10 sub-regions. The peak $C^{18}O$ emission in B7 also seems to be better correlated with the region of high extinction where a known cluster of Young Stellar Objects (YSOs) resides (Schmalzl et al., 2010).

4.1.4. Relative isotopologue abundances: $X(^{13}CO/C^{18}O)$

The map of the relative isotopologue abundances (Fig. 13, top, right) has three very distinct regions, with each one telling a different story about the gas:

- The blue regions in the centre of the filament represent an over-abundance of $C^{18}O$ with respect to ^{13}CO . This is primarily because ^{13}CO emission is beginning to or has already saturated. Hence increased emission from ^{13}CO due to the higher column density is not seen, whereas the emission from $C^{18}O$ is. These regions show where the highest column densities are, which, according to Hacar et al. (2013), correlate to the regions of highest volume density. It is in these regions that $C^{18}O$ should be used as a tracer for the H_2 .
- The red regions on the outer edge of the filament represent an under-abundance of $C^{18}O$ with respect to ^{13}CO . These are the regions where the dust column density is not high enough ($A_V < 1.2^m$) to sufficiently shield the $C^{18}O$ molecules from the ISRF¹³, yet it is high enough for the ^{13}CO to exist in a stable state due to self-shielding. It is in these regions that ^{13}CO should be used as a tracer for the H_2 .
- The green/turquoise areas represent the regions where both ^{13}CO and $C^{18}O$ emission is optically thin ($\tau < 1$). Here, the ratio of $N(^{13}CO)$ to $N(C^{18}O)$ is between 80% and 160% of the canonical value $X(^{13}CO/C^{18}O) = 7.3$ as given

¹³The required column density for a stable population of $C^{18}O$ in the Taurus complex is $A_V \approx 1.2^m$ according to the models that van Dishoeck and Black (1988) applied to the data from Frerking et al. (1982).

by Wilson and Rood (1994). 75% of these pointings have extinctions between $A_V = 1^m$ and $A_V = 5^m$. In these regions both ^{13}CO and $C^{18}O$ can be used as a tracer for the H_2 .

Furthermore, all 7 Barnard regions appear as distinct blue regions, showing that the isotopic abundance ratio is a better method to determine the regional borders than extinction.

4.2. Relationship between ^{13}CO and A_V outside the L1495-B213 filament

Figure 14 affords an overview of the variations in the spatial distribution of the $^{13}CO - H_2$ relationship in the region surrounding the L1495-B213 filament. Full sized maps have been included in Appendix A.2.

4.2.1. Extinction, A_V

The extinction map shows that, apart from a denser region west of the L1495-B213 filament (e.g. B209 - not discussed in this study - See Appendix C), the surrounding gas is either diffuse ($1^m < A_V < 5^m$) or sparse ($A_V < 1^m$). The L1495-B213 filament appears to be on the southern-most edge to the cloud. North of the filament there is a large reservoir of diffuse gas.

4.2.2. ^{13}CO column density

As ^{13}CO is not saturated at all in the diffuse ($1^m < A_V < 5^m$) regime, the column density map of ^{13}CO for the region surrounding the L1495-B213 filament shows a much more complete picture of the gas column density than inside the L1495-B213 filament. The B209 sub-region (See Appendix C for a description) is visible to the west of B7 as a peak in the ^{13}CO emission. The region of diffuse gas extending westwards appears much larger in ^{13}CO than in A_V . Owing to the intermediate extinction values in the diffuse gas and the un-saturated behaviour of the ^{13}CO emission, the ^{13}CO to H_2 abundance appears stable for column densities $A_V > 0.6^m$. The local variations in red are artefacts of the noise in the extinction values. The border of the cloud is very distinct in the $X(^{13}CO)$ abundance map, showing the region where the dust column density is high enough to shield the ^{13}CO molecules from the ISRF.

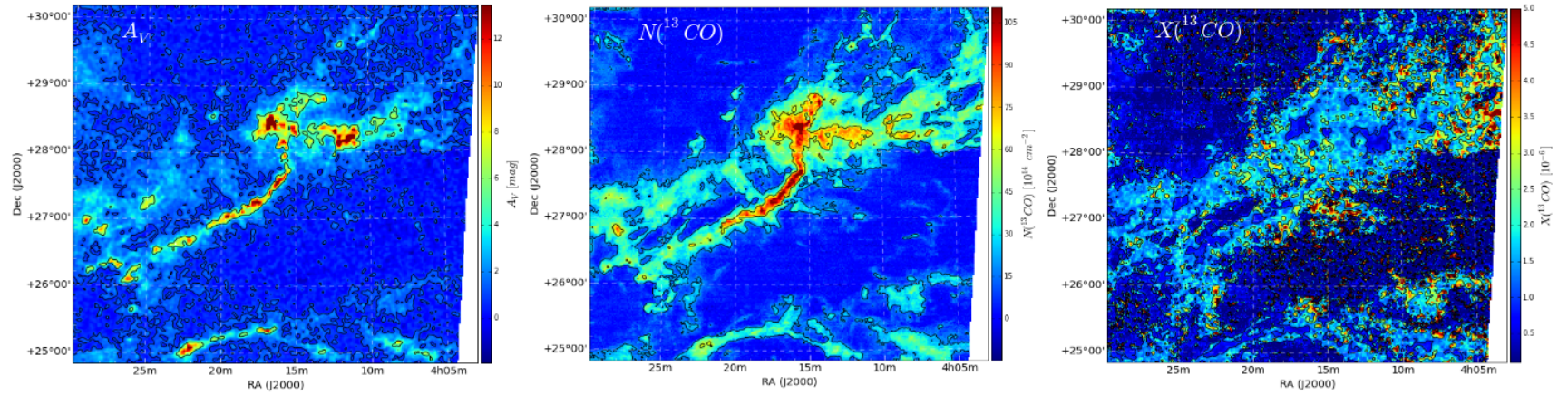


Figure 14: The region surrounding the L1495-B213 Filament: Full page versions of the individual maps are in Appendix A for clarity (A.2). This figure is solely intended to serve as a tool for a spatial comparison of the main features in each view of the filament.

(Left): Extinction, A_V . Contours: $A_V = [1, 5]$ mag.

(Middle): ^{13}CO Column Density, $N(^{13}\text{CO})$. Contours: $N(^{13}\text{CO}) = [20, 60] \cdot 10^{14} \text{ cm}^{-2}$.

(Right): ^{13}CO Abundance. Contours: $X(^{13}\text{CO}) = [1, 2.25] \cdot 10^{-6}$. The contours correspond to 66% and 150% of the literature value for the ^{13}CO abundance.

5. The ridge method for cleaning noisy data

Here we take a brief interlude in order to introduce a method that we developed and used for the following analysis. There is a large scatter in the data for the global ^{13}CO – and $C^{18}O - A_V$ relationships, as can be seen in Section 6 in Figures 15, 16, 17 and 18. Furthermore, the intrinsic uncertainties for the $N(^{13}CO)$ and $N(C^{18}O)$ measurements are on the order of 3%, while the uncertainties in derived extinction measurements are on the order of 20% for the regions where $A_V < 2^m$. These two facts combine to form a very noisy data sample. Regardless of the noise, there are still visible trends in the data. In order to be able to better quantify these trends, we developed a method which sacrificed information about the scatter of the distribution in order to recover the underlying trend. We call it the ridge method as it is akin to following the ridge of a mountain chain to determine where geological boundaries lie.

5.1. Justification

In comparison to the early work on this topic (Frerking et al., 1982) the data set used by this study was enormous. The ^{13}CO data set alone is comprised of almost 400,000 independent comparisons to extinction. Even when plotted at the smallest size, the sheer volume of data points meant that a thick dark cloud appears where there should be a thin line representing the correlation between ^{13}CO and extinction. As so many points were plotted on top of one another, information regarding the centre and direction of this data cloud was lost. This can be seen in the top panel of Figure 15. A naive best fit to the data along the A_V axis yielded a slope that is by no means representative of the data. There are several reasons for this:

- While there is a clear trend in the data, the scatter along the y-axis is so great that it is difficult to find the midpoint. Furthermore, the data points are not evenly distributed within the black cloud. For example one may expect the distribution of the data-cloud density to be Gaussian in nature for any given cross-section. This is certainly true for a horizontal cross-section of the data, however, in the vertical direction the distribution is far from ideal. In the case of our data set, in order to take advantage of the Gaussian density distribution, we would have had to fit the data along the ^{13}CO axis, which has its own set of associated problems.
- The relationship between ^{13}CO and extinction saturates after $A_V > 5^m$. The data points at high extinction have a softening effect on the fit, dragging the steep slope down. This results in the over-estimation of the ^{13}CO column density at low extinctions and under-estimation at higher extinctions.
- There are several sub-regions of the data cloud which correspond to different physical environments. This means that a linear fit in either axis will aim for

different regions and miss a significant portion of the data. For example, a linear fit along the extinction axis means that the dense trunk at low A_V is not adequately modelled. A linear fit along the ^{13}CO axis has the effect of completely missing the saturation of ^{13}CO at $A_V > 5^m$. Consequently either two or more linear fits or a non-linear function are needed to describe the data properly.

Given that the vast majority of unsaturated ^{13}CO is found in the more diffuse regions of molecular clouds, i.e. not in the dense cores, and that the diffuse regions of clouds make up a large percentage of the total cloud mass, it seems prudent that the $^{13}CO - A_V$ relationship should be accurately described. To this end we have applied this rudimentary ridge-finding technique to follow that region of greatest density in the $^{13}CO - A_V$ plane in order to find the underlying relationship.

5.2. The ridge method algorithm

The ridge method is a double binning method. We bin the plot area along both axes and then calculate the density of points in each bin. In doing so we utilise information about the correlation of the data in two dimensions simultaneously. The density values then form a three dimensional surface in $N(^{13}CO) - A_V$ space. The central idea here is that the path of least decline represents the best correlation to the data. In other words, best correlation is where the most data points are. A computer algorithm finds the “peak” of the data mountain and then finds the shallowest route down the mountain side. In pseudo-code the algorithm looks like this:

```
x,y = find_peak(map[:,:])

while (map[x,y] > height_threshold):
    saved_xy = saved_xy + (x,y)
    dx,dy = find_shallowest_step(map[x-1:x+1, y-1:y+1])
    x,y = x+xy, y+dy

return saved_xy
```

The threshold conditions used in our analysis were: the height at any position must be greater than 5 (a density of 5 points per bin) and that there must be a slope, i.e. once the algorithm reaches flat ground it stops trying to find a slope. In order to test the robustness of this method we binned the data using 250 different bin sizes, in the range $[0.1^m, 0.6^m]$ in extinction and $[0.4, 2.4] \cdot 10^{14} \text{ cm}^{-2}$ in $N(^{13}CO)$. We then plotted the routes found for each individually binned map. Figure 15 (Bottom) shows that the route down the density mountain remained constant regardless of the bin size used. Therefore assumed that we were looking at a real phenomenon rather than an

artefact of the binning process. Knowing that the ridge remained constant we found a good linear fit to the two main regions of the data for ^{13}CO and to the single region for $C^{18}O$.

While the reduction of the giant cloud of data points down into a thin, easy-to-deal-with data set seems too good to be true, it should be noted that in doing so we lose information about the data set. The true measure of the scatter is no longer visible. Furthermore, any small scale or local effects are lost anyway due to the nature of the huge data set. However, as we are more interested in global trends when using such a large data set (and global trends by nature are a superposition of many local phenomena), this is the effect for which we are looking. In essence this method trades information on the small-scale structure for information about the large-scale structure. It should also be noted that this method of analysis is reserved for data sets that are prohibitively big ($> 10^4$ data points) . As the amount of data points decreases, so too does the resolution of the 2-D bins, thus increasing the error in any functional fit to the data. Consequently we have only used this analysis for the global trends in $N(^{13}CO)$ and $N(C^{18}O)$ presented in this study.

6. The X_{CO} factor - Comparing the column densities of ^{13}CO and $C^{18}O$ with extinction A_V

In this section we present the relationships between the column densities of H_2 and the two CO isotopologues as well as their abundances relative to A_V ($\propto N(H_2)$). In essence dependence of these relationships on A_V reveals the depth of gas which each molecule is able to trace. We have also investigated the relative isotopologue ratio for $C^{18}O$ and ^{13}CO . The following analysis has been conducted under the assumption that the excitation temperature in these regions does not differ significantly from $T_{ex} = 10K$. While a homogeneous temperature through out the cloud is unrealistic, deviations of up to $\pm 40\%$ in T_{ex} introduce errors of $< 10\%$ into the column density measurements. Hence the assumption that $T_{ex} \approx 10K$ remains valid.

6.1. Relationship between ^{13}CO and A_V

6.1.1. The global relationship as derived from the ISM surrounding L1495-B213

Figure 15 shows how the ^{13}CO column density changes with extinction. ^{13}CO is saturated at extinctions higher than $A_V > 5^m$. Therefore it is a much better tracer of the diffuse gas ($A_V < 5^m$) than of the dense gas. In order to study the global $^{13}CO - A_V$ relationship we have a sample of $\approx 400,000$ points with 65% of points having $A_V < 2^m$. Figure 15 shows the data in the $N(^{13}CO) - A_V$ plane. The colours in Figure 15 (Top) shows the density of points. The highest density (dark red) region is centred around the point $(0.48^m, 1.6 \times 10^{14} \text{ cm}^{-2})$. Here there are in excess of 10^3 points per $0.1^m \times 0.4 \cdot 10^{14} \text{ cm}^{-2}$ bin. Over 300,000 points are contained inside this colourful region, showing that the vast majority of the ^{13}CO is found in the sparse and diffuse ISM ($A_V < 5^m$).

The distinct S-shape present in the data cloud is similar to that discussed by Lombardi et al. (2006) for ^{12}CO . The S-curve is a product of the effects of photodissociation by the ISRF at low A_V and emission saturation at high A_V . Consistent with the models by van Dishoeck and Black (1988) four distinct regimes are visible:

1. $A_V < 0.6^m, \tau \ll 1$: The small exponential increase seen between $A_V = 0^m$ and $A_V = 0.6^m$ is due to the increase in shielding afforded the ^{13}CO molecules by the dust as the density of the surrounding ISM increases.
2. $0.6^m < A_V < 2^m, \tau < 1$: In this regime ^{13}CO is still optically thin enough so that the emission increases linearly with column density. In other words, the vast majority of photons escape the cloud without being re-absorbed by intervening ^{13}CO molecules.

Table 3: $N(^{13}CO)$ and $N(C^{18}O)$ are in units of $[10^{14} cm^{-2}]$ and limiting A_V magnitudes are in $[mag]$

Paper	Location	Extinction Method	Res ($''$)	$N(^{13}CO) =$	Limit	$N(C^{18}O) =$	Limit	$X(^{13}CO)$	$X(C^{18}O)$
Dickman	Many	R-band Counts	93	25(A_V)	11			2.66×10^{-6}	
	Orphiucus	E(J-K)	330	27($A_V - 1.6$)	15	1.7($A_V - 3.9$)	15	2.87×10^{-6}	1.7×10^{-7}
Ferking	Taurus	E(J-K)	330	14($A_V - 1.0$)	5	1.7($A_V - 1.3$)	21	1.49×10^{-6}	1.7×10^{-7}
	Duvert	R-band Counts	150	22($A_V - 0.6$)	6			2.34×10^{-6}	
L1489	L1489	R-band Counts	150	22($A_V - 0.3$)	6	2.5($A_V - 1.1$)	6	2.34×10^{-6}	2.66×10^{-7}
	L1495	R-band Counts	150	22($A_V - 0.3$)	6			1.91×10^{-6}	
L1517	L1517	R-band Counts	150	18($A_V - 0.3$)	6			2.32×10^{-6}	2.45×10^{-7}
	Lada	NICE	90	22(A_V)	5	2.3(A_V)	15		
Alves	IC5146	NICE	50			2.1($A_V - 1.19$)	20		2.23×10^{-7}
	L977	NICE	50			2.0($A_V - 1.15$)	20		2.13×10^{-7}
Hayakawa	Cha I	J-band Counts	60-150	10($A_V + 1.0$)	10	3.2($A_V - 4.4$)	10	1.06×10^{-6}	3.40×10^{-7}
	Cha II	J-band Counts	60-150	17($A_V - 0.4$)	10	2.5($A_V - 2.0$)	10	1.81×10^{-6}	2.66×10^{-7}
Kainulainen	Cha III	J-band Counts	60-150	26($A_V - 1.8$)	6	2.3($A_V - 0.3$)	6	2.77×10^{-6}	2.45×10^{-7}
	Cha I	NICER	120			1.9($A_V - 2.5$)			2.02×10^{-7}
This study	Cha III	NICER	90			2.0($A_V - 2.0$)			2.13×10^{-7}
	B7	NICER	75	18($A_V - 0.3$)	5	2.20($A_V - 1.20$)	23	1.39×10^{-6}	1.80×10^{-7}
B10	B10	NICER	75	19($A_V - 0.0$)	5	2.10($A_V - 0.65$)	15	1.83×10^{-6}	1.95×10^{-7}
	B211	NICER	75	19($A_V - 0.1$)	5	2.68($A_V - 0.75$)	17	1.89×10^{-6}	2.34×10^{-7}
B213	B213	NICER	75	16($A_V - 0.2$)	5	2.00($A_V - 0.86$)	14	1.60×10^{-6}	1.79×10^{-7}
	B216	NICER	75	13($A_V - 0.4$)	5	2.22($A_V - 1.36$)	10	1.18×10^{-6}	1.42×10^{-7}
B217	B217	NICER	75	13($A_V - 0.4$)	5	1.97($A_V - 1.17$)	11	1.12×10^{-6}	1.36×10^{-7}
	B218	NICER	75	12($A_V - 0.1$)	5	1.82($A_V - 0.84$)	9	1.26×10^{-6}	1.32×10^{-7}
All	All	NICER	75	22($A_V - 0.5$)	< 1.8	2.25($A_V - 1.07$)	23	1.45×10^{-6}	2.15×10^{-7}
				10($A_V + 1.2$)	> 1.8				

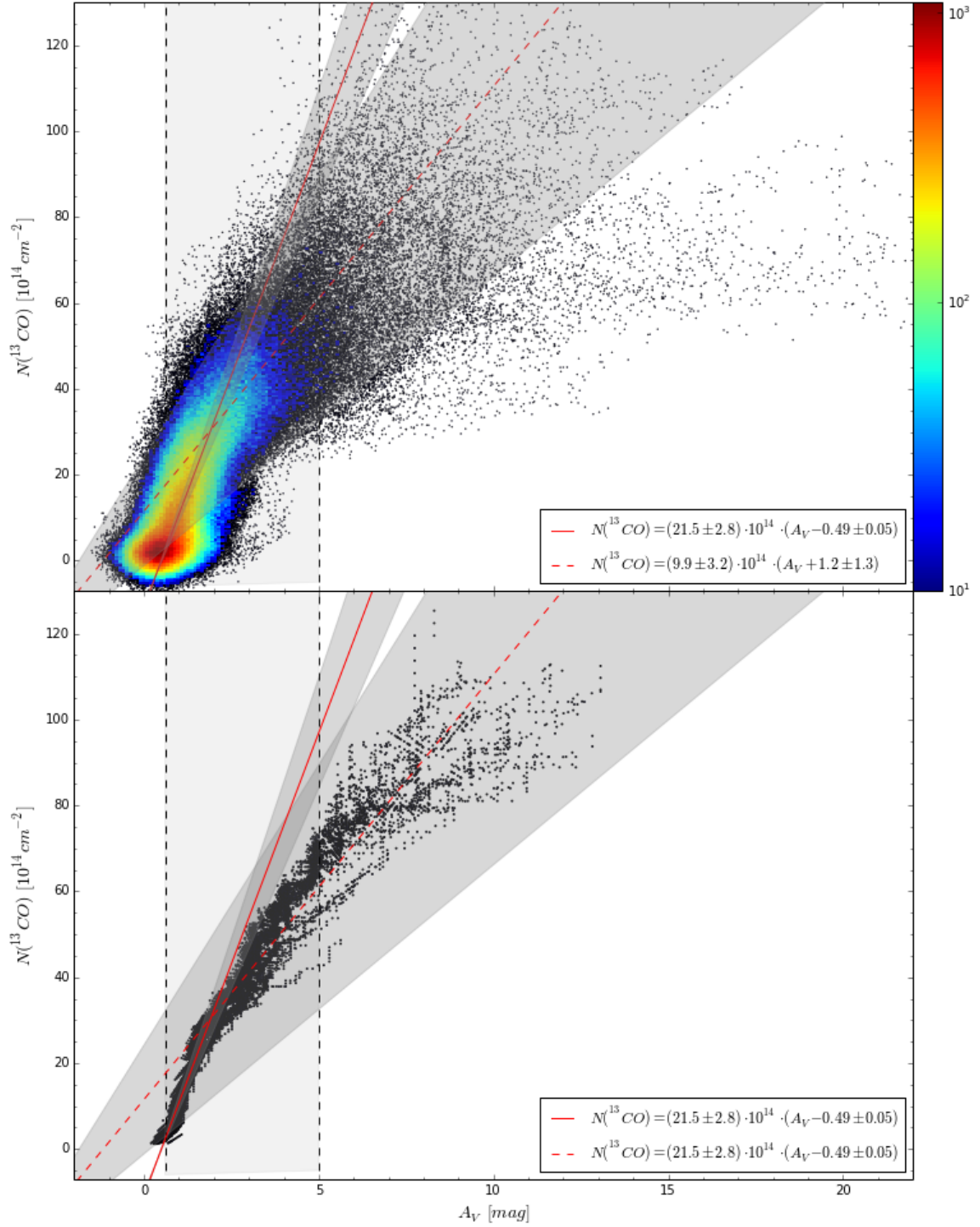


Figure 15: Top: The straight lines are best fits to the ridge line of the data set. The solid line is valid for the data trunk ($0.6^m < A_V < 2^m$) and the dashed line is valid for the turnover towards saturation ($1^m < A_V < 5^m$). The coloured region is used to show the density of points within $0.1^m \times 0.4 \cdot 10^{14} \text{ cm}^{-2}$ bins in the data clouds. The dark red regions represent a data density of over 10^3 points per bin. Over 65% of the data is within the thick trunk between $-0.5^m < A_V < 2^m$. Bottom: The position of the ridge pixels for each of the 250 different bin configurations. The solid and dotted lines are the best fits to each side of the knee around $A_V = 1.8^m$. The fork in the ridge path is an artefact of the ridge method and not a physical process revealing itself.

3. $2^m < A_V < 5^m$, $\tau \approx 1$: The optical depth along the column of ^{13}CO has increased to the point where the mean-free-path for photons emitted in the innermost regions of the cloud is on the same length of the cloud itself. At these high column densities an increasing amount of photons are absorbed by other ^{13}CO molecules before escaping the confines of the cloud. This has the effect of reducing the overall emission seen along that line of sight.
4. $5^m < A_V$, $\tau > 1$: The column density is great enough that effectively no photons emitted in the inner regions of the cloud can reach the surface without being re-absorbed by another molecule. Only photons from the surface regions ($\tau < 1$) escape. The cloud in these regions is optically thick. Here ^{13}CO can only be used to trace the mass in the outer envelope of the cloud.

We have refrained from fitting the S-curve based on the equation in Lombardi et al. (2006) to the data for two reasons. Firstly, the scatter is too great to be able to fit any curve with confidence and, secondly, the noise in the measurements near the origin makes it almost impossible to distinguish where the curve crosses the origin. Instead we applied the ridge method for 250 different configurations¹⁴ to find where the highest density of points lies. As discussed in §5, although it sacrifices information about the scatter in the data, the ridge method allows us to better constrain the underlying trend in the data by only looking at the regions with the highest density of points in the $^{13}CO - A_V$ plane. The greatest concentration of points was found to be at $[A_V, N(^{13}CO)] = [0.48^m, 1.6 \cdot 10^{14} \text{ cm}^{-2}]$. The ridge appears to follow an $N(^{13}CO) \propto 1 - e^{-A_V}$ relationship which is consistent with Equations (36) and (38) and the saturation of ^{13}CO for $A_V > 5^m$. We found linear fits to the data for the two regimes:

1. $0.6^m < A_V < 2^m$ - This regime was where the increase in $N(^{13}CO)$ was the strongest and most linear, due to the fact that $\tau \ll 1$ for those lines of sight. More than 65% of all the data points are located within this regime.

$$N(^{13}CO) [\text{cm}^{-2}] = 21.5 \pm 2.8 \cdot 10^{14} \cdot (A_V - 0.49 \pm 0.06) \quad (39)$$

An assumed $T_{ex} = 10 \text{ K}$ was used here. The slight variations in the ridge position in this regime are due only to the shift in the bin centre used for the ridge. This explains the tight correlation of ridge points in Figure 15 (Bottom). The slope for this regime is consistent with that found by Duvert et al. (1986) for L1495 and by other authors for several other clouds (See Table 3). The A_V -intercept is also consistent with these previous studies.

¹⁴The 250 different configuration included varying the bin sizes between $dA_V = [0.1^m, 0.6^m]$ and $dN(^{13}CO) = [0.4, 2.4] \cdot 10^{14} \text{ cm}^{-2}$.

2. $2^m < A_V < 5^m$ - This regime is where ^{13}CO emission loses linearity due to an ever increasing optical depth. In this regime the scatter is much greater than below $A_V = 2^m$ and the transition to a saturated state is not immediately apparent. There are also many points above the saturation limit seen at higher extinction. As discussed later in this section, this may occur because the environmental factors (e.g. age as determined by the number of YSOs) differ from sub-region to sub-region. For this regime we find:

$$N(^{13}CO) [cm^{-2}] = 9.9 \pm 3.2 \cdot 10^{14} \cdot (A_V + 1.2 \pm 1.3) \quad (40)$$

A similar slope has only been seen in one other study: Chameleon I by Hayakawa et al. (2001) for $2^m < A_V < 8^m$. The A_V -intercept is also completely unrealistic as it implies that even without any extinction the column density of ^{13}CO should be on the order of $15 \times 10^{14} cm^{-2}$. It should be noted that the apparent fork in Figure 15 (Bottom) is an artefact of the ridge method due to the large scatter in the data, not a physical process revealing itself.

6.1.2. Regional variations in ^{13}CO along the L1495-B213 filament

As is seen in the global data set (Figure 15), there is a large amount of scatter in the $^{13}CO - A_V$ relationship. Hence, in order to try to explain this we investigated each of the Barnard regions individually. We found that each region had its own distinctive slope and A_V -intercept. This implies that the local environment plays a large role in the apparent correlation between extinction and ^{13}CO column density (See Figure 16).

We attempted to find a single linear fit to the ^{13}CO data for each of the Barnard regions over the range $A_V = [0.6^m, 5^m]$. The fits shown in figure 16 represent the R^2 weighted combination of least squares fits to the data in both the ^{13}CO and A_V axes. Each region's coverage of the $N(^{13}CO) - A_V$ plane was unique. Here we give a brief description of their interesting characteristics. It should be noted that we have only fitted a single linear function to the data in the range $0.6^m < A_V < 5^m$. This is because in several cases there was insufficient data below $A_V < 2^m$ to determine a separate fit for the optically thin regime.

- B7: The most striking feature is the split in column density trends at around $N(^{13}CO) = 70 \times 10^{14}$ molecules per cm^2 . One branch heads towards a state of saturation, while the other branch continues along the line of growth set by the lower density regions. These two regions are also visible in the $C^{18}O$ data (presented in the next section), though not to the same extent. These two regions are spatially separated. The flat branch corresponds to a peak on the extinction map which is $20'$ eastward of the peak in ^{13}CO emission (the tall

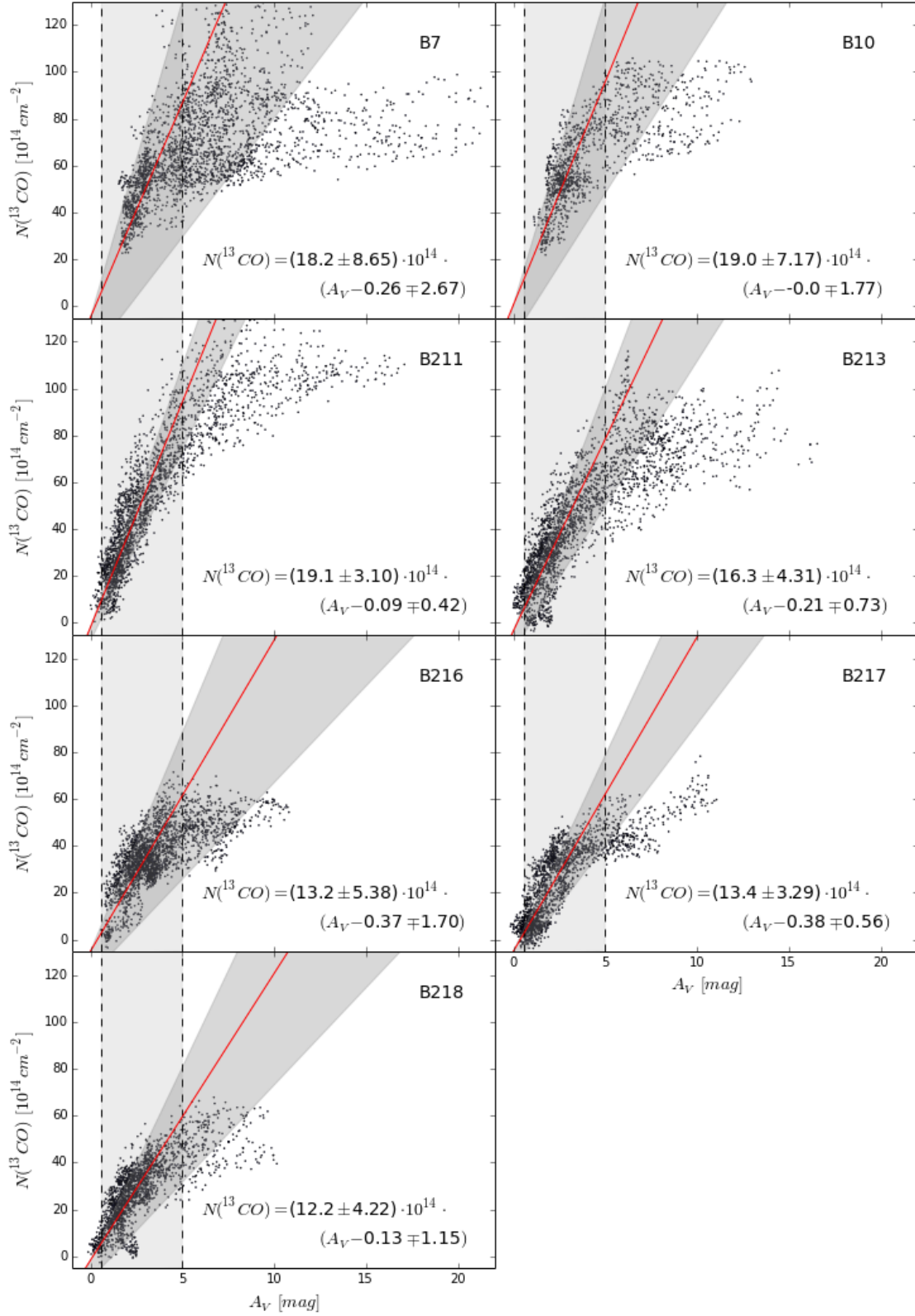


Figure 16: ^{13}CO column densities vs. A_V for the 7 Barnard regions. The solid line represents the highest R^2 weighted best fit. The grey regions show the extremes of the best fits along the ^{13}CO and A_V axes. The best fits only apply to the range $0.6^m < A_V < 5^m$.

branch). The A_V is in the same area of a known cluster of YSOs (Rebull et al., 2010). This region can be recognised in the $X(^{13}CO)$ panel of Figure 13 (Middle Right) as a blue region. The ^{13}CO abundance here is lower than average. The lack of data points at low column densities is due to the fact that the $C^{18}O$ observations (on which this data set is based) only cover the central region and none of the surrounding diffuse ISM. The best linear fit was:

$$N(^{13}CO) [cm^{-2}] = (18.2 \pm 8.65) \cdot 10^{14} \cdot (A_V - 0.26 \mp 2.67) \quad (\text{B7}) \quad (41)$$

- B10: This region shows a similar saturation rate to B7, with saturation occurring in two branches around column densities of 70 and $90 \times 10^{14} cm^{-2}$. These two apparently different populations can be reconciled two different ways. Either by assuming a difference of excitation temperature of 6-7 K between the regions, or by assuming a superposition of emission from multiple velocity components inside the sub-region (See Hacar et al., 2013).

$$N(^{13}CO) [cm^{-2}] = (19.0 \pm 7.17) \cdot 10^{14} \cdot (A_V - 0.0 \mp 1.77) \quad (\text{B10}) \quad (42)$$

- B211: This region shows a strong correlation towards a linear fit inside the regime ($0.6^m < A_V < 5^m$). This is probably due to the fact that B211 is still unbesmirched by star formation and the gas is still in a pristine state (as shown by the lack of YSOs - See Table 4 or Hacar et al., 2013). The slope for B211 ($19.1 \times 10^{14} A_V$) is the steepest slope in the L1495-B213 filament. Although the slope for B7 in our analysis is similar to the slope for B211, we cannot reliably compare these two slopes because of the forking nature of the B7 data. The best linear fit was:

$$N(^{13}CO) [cm^{-2}] = (19.1 \pm 3.1) \cdot 10^{14} \cdot (A_V - 0.09 \mp 0.42) \quad (\text{B211}) \quad (43)$$

- B213: The B213 data set is similar to the data set for the diffuse regions surrounding the L1495-B213 filament. The steep increase in ^{13}CO column density with extinction between $A_V = [0, 1.8]$ is visible, as is the slow turnover towards a state of saturation. A similar branching pattern to B7 is also visible, though it is not nearly as pronounced. This may be due to variations in the excitation temperature in different areas of B213. The increased local radiation field from the 14 YSOs (Rebull et al., 2010) in B213 may cause a change in excitation temperature in the surrounding ISM. An increase to $T_{ex} \approx 13K$ (Fig. 12) would increase the "apparent" column density by 10%, bringing the outliers in line

with the rest of the data cloud. The best linear fit was:

$$N(^{13}CO) [cm^{-2}] = (16.3 \pm 4.31) \cdot 10^{14} \cdot (A_V - 0.21 \mp 0.73) \quad (\text{B213}) \quad (44)$$

- B216/217/218: The tail region of the L1495-B213 filament is mainly dominated by low column density regions and extinctions of less than 5^m . B216, B217 and B218 all show a pretty linear trend, however, they also appear to saturate at much lower column densities ($40 \times 10^{14} cm^{-2}$) than those seen in B7, B10, B211 and B213.

$$N(^{13}CO) [cm^{-2}] = (13.2 \pm 5.38) \cdot 10^{14} \cdot (A_V - 0.37 \mp 1.70) \quad (\text{B216}) \quad (45)$$

$$N(^{13}CO) [cm^{-2}] = (13.4 \pm 3.29) \cdot 10^{14} \cdot (A_V - 0.38 \mp 0.56) \quad (\text{B217}) \quad (46)$$

$$N(^{13}CO) [cm^{-2}] = (12.2 \pm 4.22) \cdot 10^{14} \cdot (A_V - 0.13 \mp 1.15) \quad (\text{B218}) \quad (47)$$

According to the velocity analysis by Hacar et al. (2013) the sub-regions B216, B217 and B218 have very few velocity-coherent components, and those which are visible, aren't superposed. This leads to a situation where the emission in these sub-regions is due to only a single component. In other words, these regions show the simple underlying $^{13}CO - A_V$ relationship where ^{13}CO emission saturates around column densities of $N(^{13}CO) = 50 \times 10^{14} cm^{-2}$. The other sub-regions (B7, B10, B211 and B213) each contain several velocity coherent components, many of which are positioned in front of each other. However due to their different individual velocities, ^{13}CO emission from each component is generally not absorbed by the other components. Therefore, while the emission from each one may already be saturated, the total emission that is received from the whole sub-region is a superposition of each velocity components' emission. This is another possible explanation for why saturation in B7, B10, B211 and B213 occurs at much larger column densities than for B216, B217 and B218.

It is clear from Figure 16 that the quality of linear fits to the $N(^{13}CO)$ data is not very high. The fact that ^{13}CO saturates after $A_V > 5^m$ means that any line that is fitted to the data is only valid between $0.6^m < A_V < 5^m$. However even for these regions it is difficult to filter out the noise to find an adequate fit. It is also quite visible that local ^{13}CO column densities are very regionally dependent and even then, processes inside those regions lead to large differences on scales smaller than the region itself.

One might even go so far as to say that due to the size of these variations on sub-parsec scales and due to the limited range of extinction that ^{13}CO is able to probe, it would be foolish to determine a “global” relationship between H_2 column density and ^{13}CO emission. It would be even more foolish to blindly use it to make assumptions about the structure of molecular clouds and their cores.

6.2. Relationship between $C^{18}O$ and A_V

As seen in the previous section, ^{13}CO has a very narrow usable range due to its short optical depth relative to the depth of molecular clouds. $C^{18}O$ on the other hand is much less abundant and is consequently much less opaque, allowing us to see much further into the heart of clouds than with either ^{12}CO or ^{13}CO . According to Hacar et al. (2013) $C^{18}O$ emission is optically thin in the A_V range available to us ($2^m < A_V < 25^m$ - Figure 17). This confirms that it is a much better tracer of dense gas in molecular clouds than ^{13}CO . Therefore a calibration of the abundance of $C^{18}O$ is needed for obtaining meaningful estimates of cloud masses.

6.2.1. The global relationship

In Figure 17 we see that there is a large spread to the data points, however, a clear trend is visible. The large scatter is consistent with that reported by previous studies (e.g. Frerking et al., 1982). The scatter is evenly distributed around the line of best fit. Contrary to the work by Frerking et al. (1982) we don’t see a discontinuity in the flow of data points (See Figure 24 in §6.6). Furthermore, we see a large clump at $A_V < 3^m$ corresponding to the more diffuse regions of L1495-B213. It is interesting to note that the so-called “turn-on” value¹⁵ for $C^{18}O$ is close to unity ($A_V = 1.07$). This is very close to the value published by Duvert et al. (1986) for the same region ($A_V = 1.10$) and not too far from the value found by other authors for different regions, like Alves et al. (1999) for IC5146 ($A_V = 1.19$) and L977 ($A_V = 1.15$) and Hayakawa et al. (2001) for Chameleon. The oft-cited work by Frerking et al. (1982) found a value of ($A_V = 1.3$) which is within uncertainties of our results. The models of van Dishoeck and Black (1988) predict a turn-on value of $A_V = 1.2$ for $C^{18}O$. Figure 17 shows the best fit for the global relationship between $N(C^{18}O)$ and A_V . We find:

$$N(C^{18}O) = (2.25 \pm 0.37) \cdot 10^{14} \cdot (A_V - 1.07 \pm 0.60) \quad (48)$$

This equation was found by using the ridge technique described in §5. The grey area in Figure 17 describes the variation in the slopes and A_V -axis intercepts found for different binning configurations. It doesn’t describe the spread of the data point

¹⁵The turn-on value is the value at which dust shielding becomes effective enough to allow the molecule to survive the UV component of the interstellar radiation field.

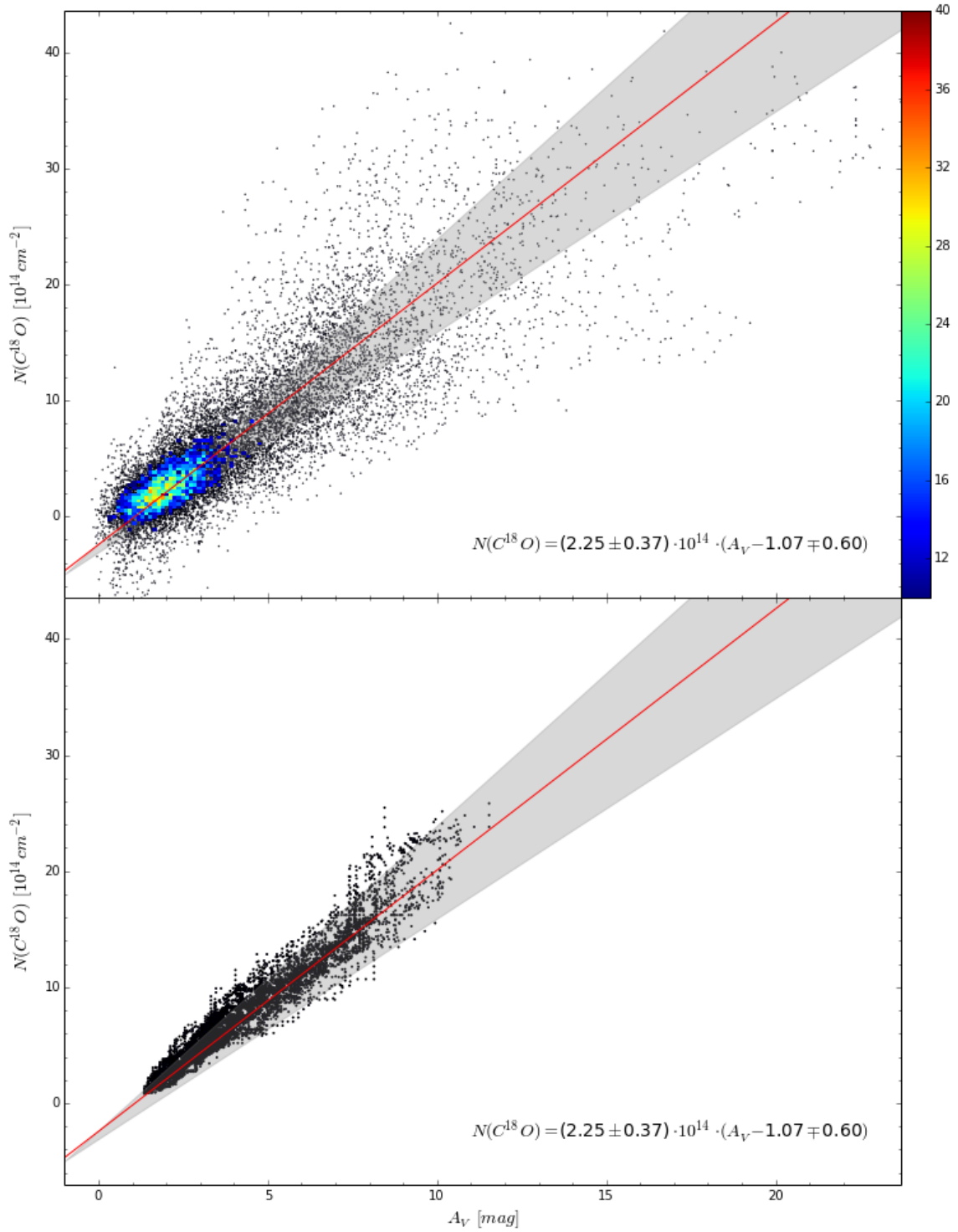


Figure 17: $N(C^{18}O)$. Top: The solid line represents the best fit to the data using the ridge method. The grey region represents the region bounded by the naive ridge-less single axis linear regressions. These fits from the ridge method fell inside the grey region. Bottom: The points along the ridges found for each of the 250 different bin configurations.

cloud. Ridges were found for 250 different 2D histograms with bin-widths in the range $dA_V = [0.1^m, 0.6^m]$ and $dN(C^{18}O) = [0.16, 1.0] 10^{14} \text{ cm}^{-2}$. To determine the slope of the ridges we tried several different linear fitting algorithms involving one and two axes. All fits to the data were within the grey region (i.e. the region bounded by the naive ridge-less single axis linear regressions) shown in Figure 17. Therefore we decided to take the best fit to all ridge paths generated by the ridge method.

6.2.2. Regional variations in $C^{18}O$

In order to better quantify which sub-regions were contributing most to the large scatter present in the global trend for $C^{18}O$ and to possibly explain why this scatter exists, we split up the data set up into its constituent regions: B7, B10, B211, B213, B216, B217 and B218 (as shown in Figure 2). Each of these regions respectively contained 2490, 1155, 2370, 2494, 2306, 1808 and 1966 data points. The slopes of the best linear fits to the individual regions vary by up to 0.43×10^{14} molecules/cm²/mag from the global trend (Table 3 summarises the best fit equations for each region). For example, the slope of the most under-developed region B211 (Hacar et al., 2013) has a gradient of 2.68×10^{14} molecules/cm²/mag, compared to the global average of 2.25×10^{14} molecules/cm²/mag. According to Hacar et al. (2013) B211 contains no YSOs and only 1 dense core, hence, it can be argued that it is the least disturbed region along the L1495 filament. B218 on the other hand has the shallowest slope of 1.82×10^{14} molecules/cm²/mag and 3 embedded YSOs. B7, which is by far the largest region spatially and contains a young cluster, is found to have a moderate slope of 2.2×10^{14} molecules/cm²/mag, very close to the average slope for the whole filament.

In general all the regions follow a strictly linear fit with no evidence that $C^{18}O$ undergoes any saturation in the regime $A_V < 15^m$. This is expected as the lower abundance of $C^{18}O$ means that the H_2 column density needs to be much higher to become opaque. B7 shows a curious scatter in higher regions of the envelope. It appears to be split into three regions. One follows the linear best fit, another bends upwards towards a higher $C^{18}O$ abundance and another downwards towards a lower abundance, possibly signalling that the molecule is beginning to deplete or that the excitation temperature of the ISM is greater than 10K in that region. The presence of N_2H^+ cores as reported by Hacar et al. (2013) indicates that the B7 sub-region is chemically older than several of the other sub-regions. The N_2H^+ cores show that the abundance of $C^{18}O$ in the densest inner regions is much lower than in the envelope. This is because N_2H^+ can only survive if $C^{18}O$ has frozen onto the surface of grains. We therefore suggest that the slope is indicative of the history and large scale chemical development of each region (Bergin and Tafalla, 2007).

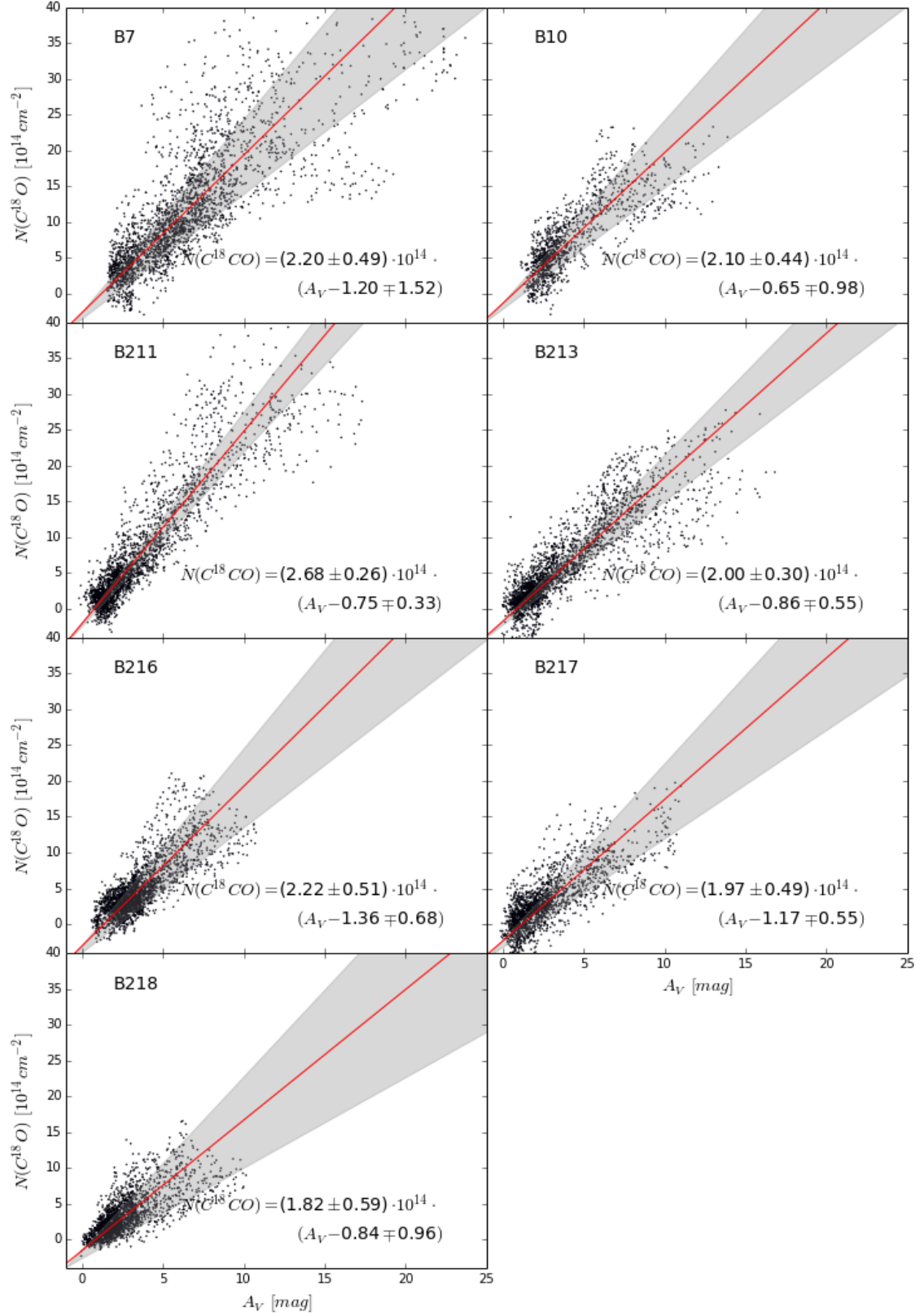


Figure 18: $N(C^{18}O) - A_V$ relationships for B7, B10, B211, B213, B216, B217 and B218.

The solid line represents the best fit to the data using a weighted average of the best fits along each axis. The grey region shows the region bounded by the individual single axis fits. This can be taken as a measure of the uncertainty in each fit.

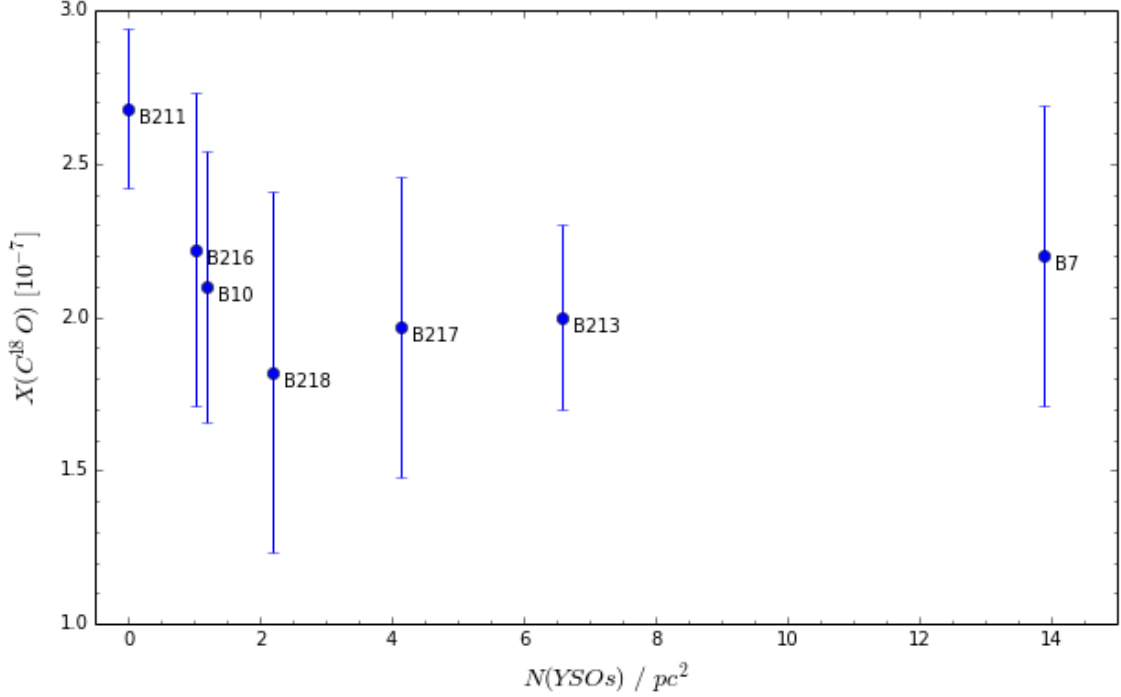


Figure 19: The average local abundance of $C^{18}O$ versus the surface density of YSOs for all 7 Barnard regions. There is a loose correlation between the surface density of YSOs and the $C^{18}O$ abundance.

In Figure 19 we show the relationship between the YSO surface density¹⁶ and slope of the best fit to the $A_V - N(C^{18}O)$ relationship for each sub-region. A loose correlation is visible between the two, showing that more evolved regions have a lower $C^{18}O$ abundance. This is probably due to $C^{18}O$ freezing onto the surface of grains at the centre of the cores. The more cores present, the more $C^{18}O$ is removed from the cloud.

6.3. Relative abundances of ^{13}CO and $C^{18}O$ compared to H_2

6.3.1. Global relationships along the filament and around L1495-B213

The abundances of ^{13}CO and $C^{18}O$ relative to H_2 were calculated for the L1495-B213 filament and for ^{13}CO for the surrounding region (Figure 20). In order to only include data with less than 20% combined error ($\sigma_{A_V} + \sigma_{N(X)}$) we excluded all data below $A_V = 1^m$ when calculating the best fits. We also excluded all ^{13}CO and $C^{18}O$ data with an integrated intensity $W(X) < 0.5 [K km/s]$ in order to remove points with a low signal to noise ratio (Hacar et al., 2013). Only regions which were dense enough to ensure no photo-disassociation by the interstellar radiation field were used

¹⁶The YSO surface density is calculated by dividing the number of known YSOs in the sub-region by the area of the sub-region. This gives us a measure of the amount of YSOs per square parsec.

Region	Cores	YSOs	Slope	A_V -Intercept
B7	3	25	2.20 ± 0.49	1.20 ± 1.52
B10	5	1	2.10 ± 0.44	0.65 ± 0.98
B211	1	0	2.68 ± 0.26	0.75 ± 0.33
B213	7	14	2.00 ± 0.30	0.86 ± 0.55
B216	0	2	2.22 ± 0.51	1.36 ± 0.68
B217	0	5	1.97 ± 0.49	1.17 ± 0.55
B218	3	3	1.82 ± 0.59	0.84 ± 0.96

Table 4: The number of dense cores (based on H_2H^+ condensations - (Hacar et al., 2013)) and YSOs (based on Spitzer colour-colour cuts - Rebull et al., 2010) are given for each of the sub-regions: B7, B10, B211, B213, B216, B217 and B218. A weak correlation can be seen between the number of YSOs and the slope of the $C^{18}O - A_V$ relationship. This can be interpreted to mean that the more developed a region is, the lower the $C^{18}O$ abundance is.

to calculate the abundances, thus providing a more robust measurement of the actual abundance ratios: $X(^{13}CO)$, $X(^{18}CO)$ and $X(^{13}CO/C^{18}O)$ ¹⁷. The asymptotic behaviour of the $X(^{13}CO)$ data points in Figure 20 is justification for removing the data points at low A_V . In the upper right frame of Figure 20 one can also see how much of an influence the large number of points near the origin (representing the exposed, un-shielded diffuse gas) have on the determination of the average abundance.

We found that for $C^{18}O$ the abundance stayed relatively constant over the range $A_V > 2^m$ at around $X(C^{18}O) = (2.1 \pm 0.64) \cdot 10^{-7}$. This is $\sim 25\%$ greater than the value proposed by Frerking et al. (1982) ($X(C^{18}O) = 1.7 \cdot 10^{-7}$) for Taurus and within the range given by most other sources (See Table 3). As $C^{18}O$ does not suffer from saturation over the range that we observe, the derived abundance stays mostly constant over the whole A_V range.

Over the un-saturated range ($1^m < A_V < 5^m$) for ^{13}CO we see no difference between the ^{13}CO abundance in the filament ($X(^{13}CO) \approx (1.45 \pm 0.53) \cdot 10^{-6}$) and the ^{13}CO abundance in the surrounding diffuse medium ($X(^{13}CO) \approx (1.41 \pm 0.51) \cdot 10^{-6}$). These values are similar to the ^{13}CO abundance for Taurus as derived by Frerking et al. (1982) ($X(^{13}CO) = 1.49 \cdot 10^{-6}$). The $1/A_V$ dependence of abundances is apparent in both the ^{13}CO plots in Figure 20. Above $A_V > 5^m$ the average ^{13}CO abundance drops steadily with increasing A_V . This is consistent with the fact that ^{13}CO is no longer optically thin and reiterates the assertion that ^{13}CO is a poor tracer of high column density ($A_V > 5^m$) molecular gas.

¹⁷Here we define the ratios $N(^{13}CO)/N(H_2)$, $N(C^{18}O)/N(H_2)$ and $N(^{13}CO)/N(C^{18}O)$ as $X(^{13}CO)$, $X(^{18}CO)$ and $X(^{13}CO/C^{18}O)$

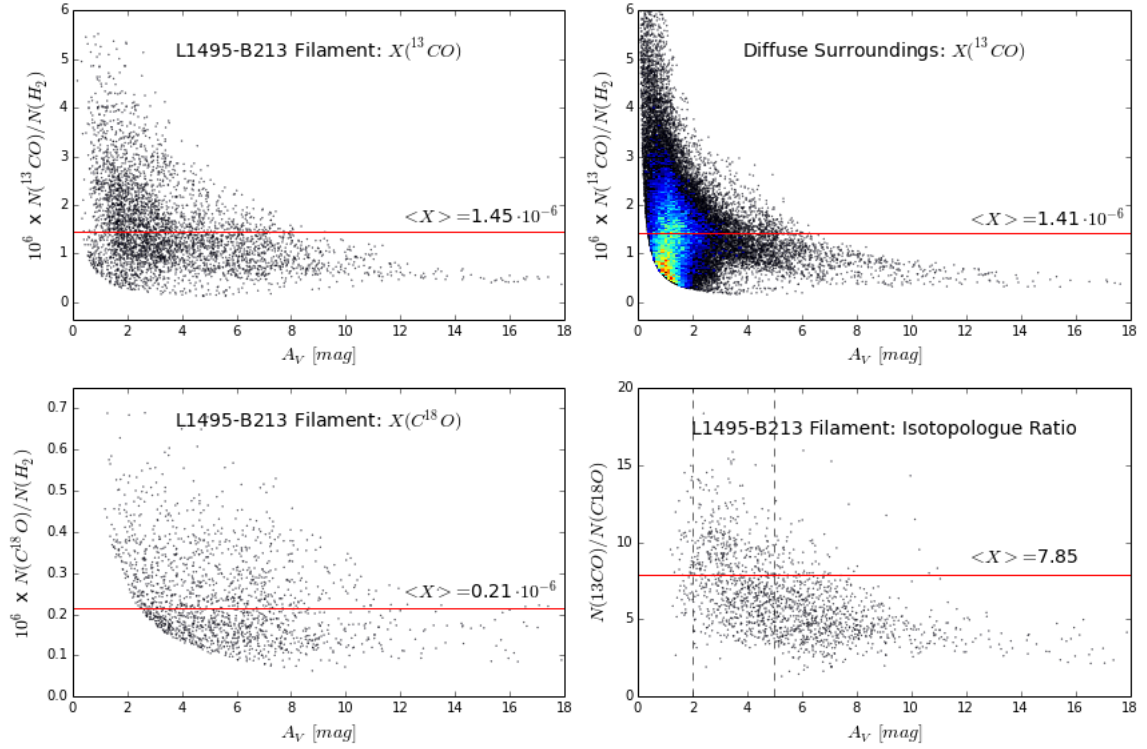


Figure 20: The solid lines represent the average ^{13}CO or $C^{18}O$ abundance along the length of the filament. The average for $X(^{13}CO)$ has been calculated from points in the range $1^m < A_V < 5^m$ whereas for the determination of $X(C^{18}O)$ all data points above $A_V > 2^m$ have been used. For the isotopologue ratio only the region between $2^m < A_V < 5^m$ was used so that data affected by ^{13}CO saturation ($A_V > 5^m$) and $C^{18}O$ photodissociation ($A_V < 2^m$) did not skew the average. The coloured regions of the $X(^{13}CO)$ graph for the filament show the increasing density of points in that area. The highest density, red, has 800 points per pixel.

6.3.2. Local variations of $X(^{13}CO)$, $X(C^{18}O)$ and $X(^{13}CO/C^{18}O)$

In order to get a better picture of what is happening inside the L1495-B213 filament on parsec scales, we mapped the abundances along the filament (See Figure 13 and Appendix A.1). The regions B216, B217 and B218 appear to have an average ^{13}CO abundance about 20% lower than the canonical abundance ($X(^{13}CO) \approx 1.5 \times 10^{-6}$, $X(C^{18}O) \approx 2 \times 10^{-7}$) while B7, B10, B211 and B213 show an increased average ^{13}CO abundance. The same discrepancy between the northern (B7-B213) and southern (B216-B218) regions is found for the $C^{18}O$ abundance ratio. The edges of the filament show an under-abundance of $C^{18}O$ due to the low column densities and consequent lack of shielding from the ISRF.

In the wider area outside the filament there is a stark contrast between regions of average and under abundance in ^{13}CO . This makes the phenomena of self-shielding

and/or sub-thermal excitation easily visible. The dark blue regions have column densities too low for the survival of ^{13}CO against the ISRF. This fact could be used to accurately define the boundaries of the L1495 cloud complex.

Table 5 gives a summary of the average isotopologue abundances with respect to H_2 and each other. Individual abundances differ by up to 50% from the global average, while the isotopologue ratio generally remains between 6 and 9 (which is within uncertainties of the canonical value of 7.3 from Wilson and Rood (1994)).

Region	$X(^{13}CO)$ [10^{-6}]	$X(C^{18}O)$ [10^{-7}]	$X(^{13}CO/C^{18}O)$
B7	1.86 ± 0.57	1.80 ± 0.56	6.59 ± 1.87
B10	2.10 ± 0.60	1.95 ± 0.68	8.76 ± 1.87
B211	2.08 ± 1.41	2.34 ± 0.79	8.02 ± 1.95
B213	1.92 ± 3.13	1.79 ± 0.60	7.46 ± 1.43
B216	1.27 ± 0.26	1.43 ± 0.67	7.91 ± 1.22
B217	1.26 ± 0.22	1.36 ± 0.70	5.80 ± 1.19
B218	1.32 ± 0.37	1.32 ± 0.68	8.32 ± 1.13
Average along L1495	1.45 ± 0.53	2.15 ± 0.64	7.9 ± 2.5

Table 5: ^{13}CO and $C^{18}O$ abundances and the $^{13}CO - C^{18}O$ Isotopologue ratio for the Barnard regions.

6.4. Confirmation of the ratio of the isotopologues ^{13}CO to $C^{18}O$ - $X(^{13}CO/C^{18}O)$ and departures therefrom

As the calculation was trivial, we also determined the average relative abundances of the isotopologues of ^{13}CO to $C^{18}O$ for L1495-B213. This was done by taking the ratio of ^{13}CO to $C^{18}O$ for each pixel along the filament and then plotting the relative occurrence of different ratios on a histogram. This showed that the large variations in the relative abundances along the L1495-B213 filament (Figure 13 (Bottom-right)) are not isolated occurrences. From this histogram we were able to see how much the saturated ($A_V > 5^m$) regions were reducing the average isotopologue ratio. After excluding these regions, we found the average of the isotopologue ratio to be $\langle X(^{13}CO/C^{18}O) \rangle \approx 7.9 \pm 2.5$ for all pixels in the range $2^m < A_V < 5^m$. This value is roughly 10% greater than the literature value of 7.3 (Wilson and Rood, 1994).

6.5. The $X(CO/H_2)$ ratio and conversion to $N(^{12}CO)$

By assuming the isotopic ratios given by Wilson and Rood (1994) for $C^{18}O$ and ^{13}C of 560 and 77 respectively we find the abundance of ^{12}CO over the L1495-B213 filament

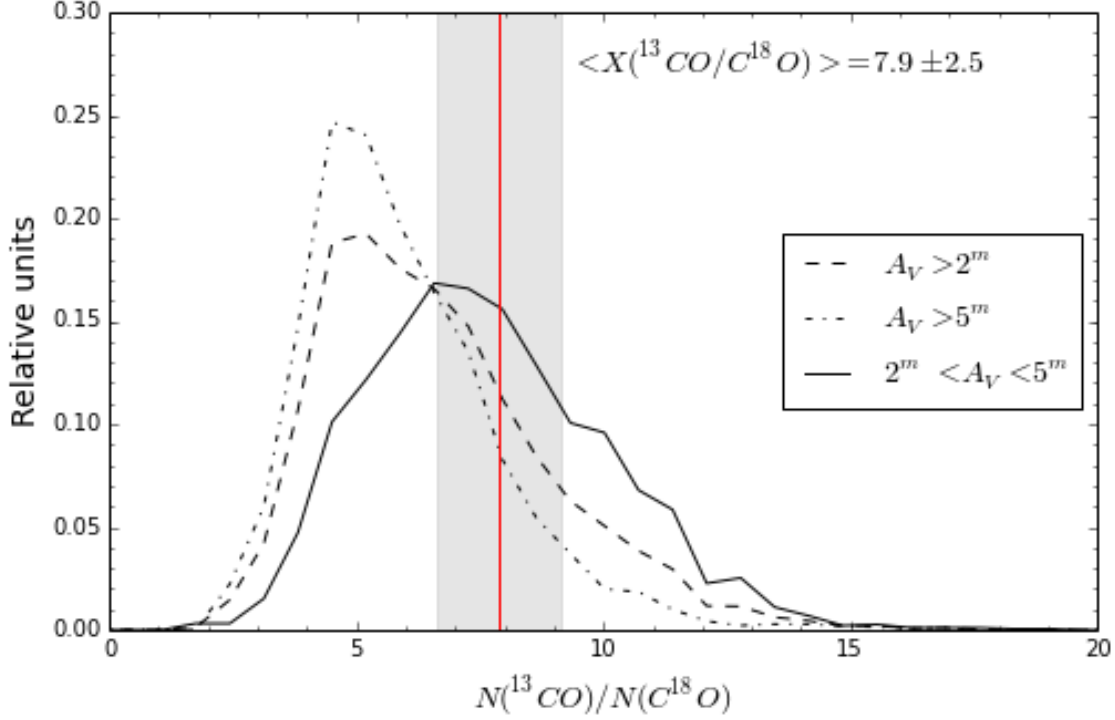


Figure 21: The ratio of ^{13}CO to $C^{18}O$ was calculated for each pixel along the filament and the relative occurrence of different ratios are plotted here. This shows that there are large variations in the relative abundances along the L1495-B213 filament. The average isotopologue ratio in the range $2^m < A_V < 5^m$ is shown by the vertical line - $\langle X(^{13}CO/C^{18}O) = 7.9 \pm 2.5 \rangle$. The dot-dashed line is indicative of the ^{13}CO to $C^{18}O$ ratio for high column density regions $A_V > 5^m$ where ^{13}CO has already begun to saturate. The dashed line has been plotted in order to show how the saturation of ^{13}CO will reduce the average ratio between isotopologues if the data for $A_V > 5^m$ is not excluded from the average. It is also clear that no single, constant isotope ratio is visible along the filament, but rather a wide variation in the range 8 ± 3 .

to be:

$$X_{CO} = (1.20 \pm 0.36) \cdot 10^{-4} \quad (\text{based on } C^{18}O \text{ in the filament}) \quad (49)$$

$$X_{CO} = (1.08 \pm 0.39) \cdot 10^{-4} \quad (\text{based on } ^{13}CO \text{ in the surrounding medium}) \quad (50)$$

As a quick comparison to the literature, Frerking et al. (1982) put forward the ratio $N(^{12}CO)/N(H_2) = 0.85 \cdot 10^{-4}$ based on a conversion factor of $X(^{12}CO/C^{18}O) = 500$ (the accepted value at the time of publication). A recalculation using the currently accepted value of 560 would result in $X(^{12}CO/H_2) = 1.01 \cdot 10^{-4}$.

Turning our $^{12}CO - H_2$ relationship around so that it is useful to those in the extragalactic astronomy circles, the conversion factor for turning CO measurements into H_2 masses becomes:

$$N(H_2) = (0.83 \pm 0.25) \cdot 10^4 \cdot N(^{12}CO) \text{ (based on } C^{18}O \text{ inside the filament)}$$

$$N(H_2) = (0.92 \pm 0.33) \cdot 10^4 \cdot N(^{12}CO) \text{ (based on } ^{13}CO \text{ outside the filament)}$$

We favour the conversion factor based on $C^{18}O$ because of its greater linearity over the observed range of extinction and the lower scatter in the data points. This conversion factor, however, is limited to describing the diffuse medium where ^{12}CO is not saturated. However as that pertains to the majority of a galactic disk and ^{12}CO is by far the strongest observable CO isotopologue, this conversion factor is the best way to constrain the mass of molecular hydrogen outside the Milky Way.

6.6. Comparison to the literature

The importance of CO as a tracer of molecular hydrogen has led many previous authors to attempt to determine the ratio $X(A) = N(A)/N(H_2)$ for the two isotopologues ^{13}CO and $C^{18}O$ for different nearby molecular clouds (See Table 3). Figure 25 graphically shows the $N(C^{18}O)/A_V$ relationship of 6 previous studies (as given in Table 3) combined with the new data from this study.

6.6.1. Comparison to the study by Frerking et al. (1982)

One of the major references in this area is the study by Frerking et al. (1982) which has been cited over 700 times. Due to the proximity of the region in Taurus studied by Frerking et al. (1982) we have used their data for comparison. There are however some fundamental differences in the techniques used. Frerking et al. (1982) used the spectra of 14 stars in Taurus to determine the ^{13}CO and $C^{18}O$ emission and extinction along those lines of sight. We have a data set of almost 400,000 data points in the $^{13}CO - A_V$ plane and 14,800 in the $C^{18}O - A_V$ plane from dedicated ^{13}CO and $C^{18}O$ emission and extinction maps of the L1495-B213 complex. The uncertainties presented in Frerking et al. (1982) represent the uncertainties in the line widths of individual spectra, not the intrinsic scatter inherent in the emission from the various CO isotopologues over a large area. The scatter present in our work is due to spatial variations in the column densities of H_2 , ^{13}CO and $C^{18}O$. Remarkably, the $C^{18}O$ to A_V correlation presented by Frerking et al. (1982) is similar to the one which we have derived for the whole L1495-B213 filament, namely:

$$N(C^{18}O) = 1.7 \cdot 10^{14} \cdot (A_V - 1.3)$$

compared to the relationship from our analysis:

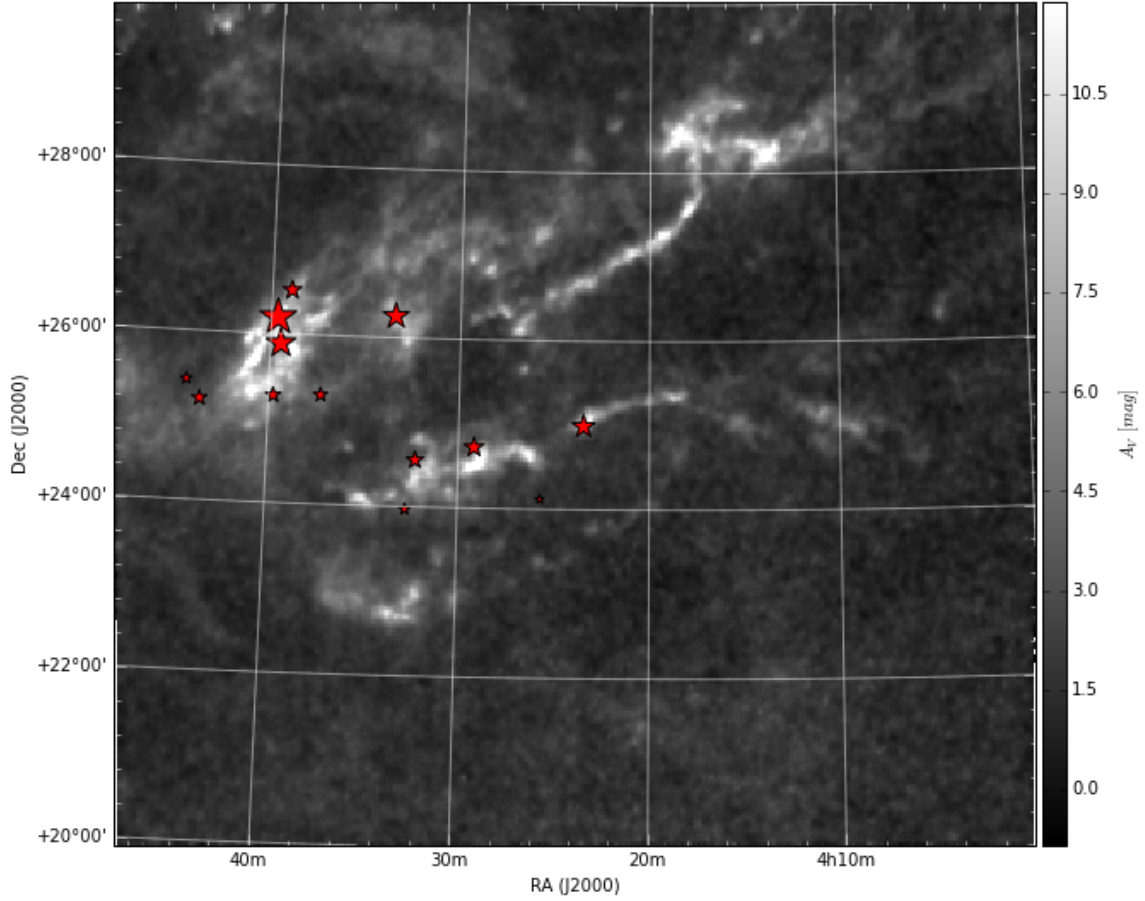


Figure 22: Location of the sources used by Frerking et al. (1982). The size of the stars indicate the amount of extinction along the line of sight as reported by Frerking et al. (1982). The L1495-B213 complex is located in the upper centre of the image, while sources observed by Frerking et al. (1982) are mostly in the neighbouring region.

$$N(C^{18}O) = (2.25 \pm 0.37) \cdot 10^{14} \cdot (A_V - 1.07 \pm 0.60)$$

In Figure 24 we show the 14 data points from Frerking et al. (1982) alongside the 14,800 points using in this study. While the uncertainty in these points covers the same range as our data, their best fit quite clearly underestimates the true relationship between $C^{18}O$ and A_V by about 25%.

In order to be able to better explain differences between our work and the work of Frerking et al. (1982), we compared the regions used by both studies. Figure 22 shows the Taurus region and the location of the source used by Frerking et al. (1982). It is clear that we were not looking at exactly the same clouds. Frerking et al. (1982) observed sources located in L1521, Heiles' Cloud 2 and B18. These clouds are generally taken to be relatively evolved, which explains the low abundances derived by Frerking

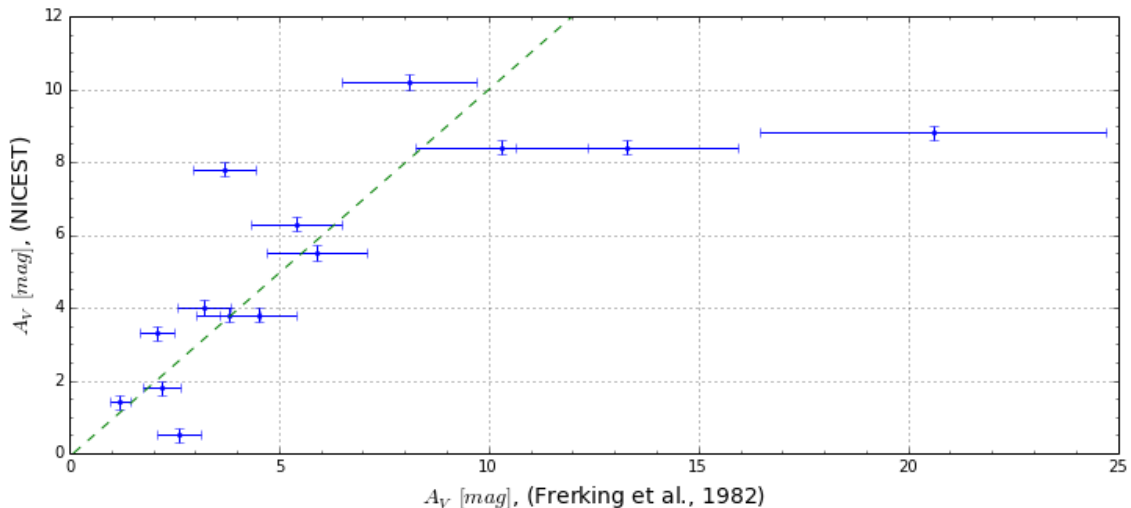


Figure 23: The extinction measured by Frerking et al. (1982) towards the 14 sources compared to the corresponding extinction values from the map by Lombardi et al. (2010). The horizontal error bars represent the error for each pixel based on the corresponding error map. The vertical error bars represent an assumed 20% error in the extinction values derived by Frerking et al. (1982) as the actual uncertainties were unpublished.

et al., 1982. Furthermore, by sampling various cloud, their study did not trace the variation of $C^{18}O$ inside a single cloud, but reflected the state of $C^{18}O$ under various different (evolved) environments.

Using the coordinates given in Frerking et al. (1982), we also compared their extinction values to those published by Lombardi et al. (2010) - See Figure 23. In general the two data sets are close to following a one-to-one correlation. At higher extinction, though, the Frerking et al. (1982) A_V measurements increase at a greater rate than those from the NICEST map. This is probably due to the fact that the NICEST values have been calculated using an average extinction derived from several background stars and have therefore smoothed out any local over-densities, while the Frerking et al. (1982) extinction values were derived from the colour excess of a single star and are susceptible to any small scale sub-pixel structure present in dense clouds. The sub-region B218 was had the closest slope (1.82) to Frerking et al. (1982) (1.7), however, comparing the two is a moot point as the Frerking et al. (1982) analysis combined data from several different regions in Taurus.

We take the fact that our data set reproduces the $C^{18}O - A_V$ relationship published by Frerking et al. (1982) as confirmation that our methods are sound. The advantage of having a data set 3 orders of magnitude larger than Frerking et al. (1982) has allowed us to refine the $C^{18}O - A_V$ relationship to that given in Equation (48) as well

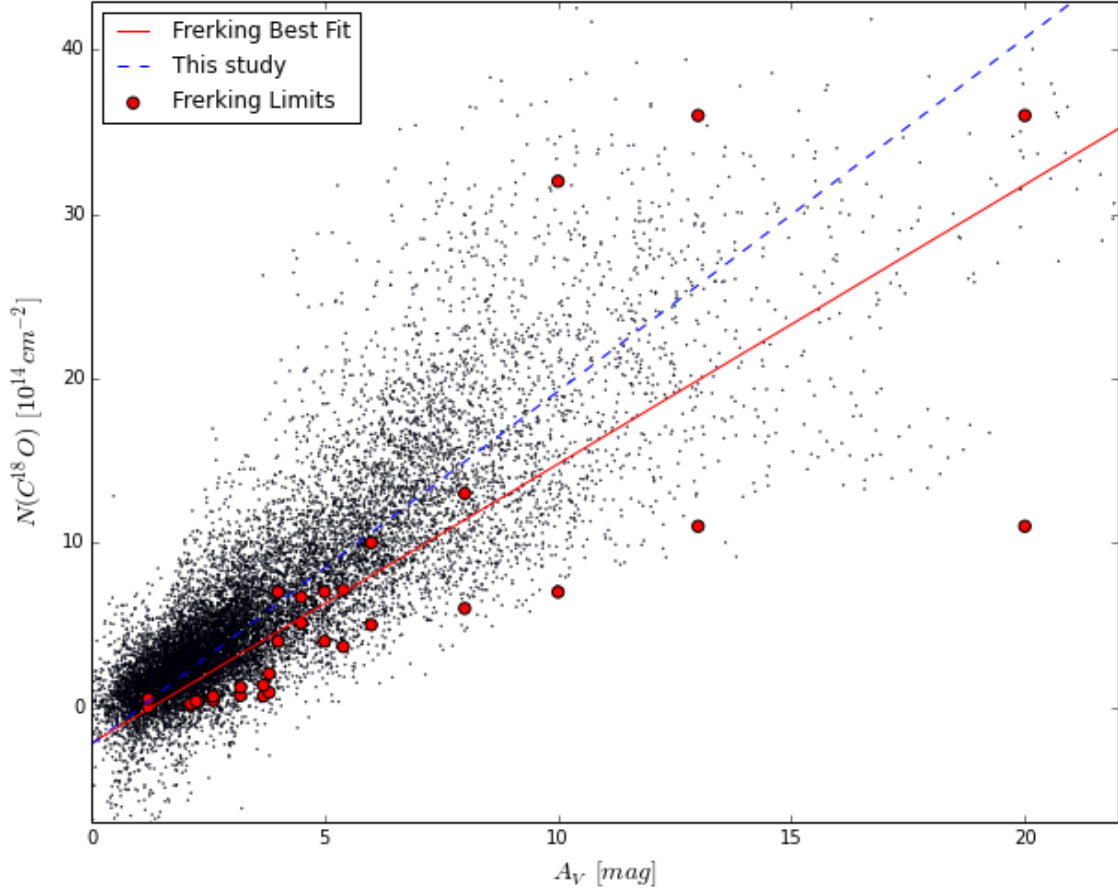


Figure 24: The solid line is the relationship described by Frerking et al. (1982). The dashed line is our best fit to the $C^{18}O$ - A_V relationship. The black dots are the pixel values along the whole L1495-B213 filament.

as explain the large uncertainties published by Frerking et al. (1982).

6.6.2. Comparison with other authors

Aside from Frerking et al. (1982) we have also looked at various works published by other authors. We found that the $C^{18}O - A_V$ relationship varied by almost a factor of two over the 5 other studies under consideration (Duvert et al., 1986, Lada et al., 1994, Alves et al., 1999, Hayakawa et al., 2001 and Kainulainen et al., 2006). The large spread in the $C^{18}O$ abundances is also apparent in the work by Hayakawa et al. (2001). This means that looking for a universal law that converts any CO isotopologue intensity into an H_2 mass will never be more accurate than a factor of 2 unless one has more information about the intra-cloud environment.

What is clearly visible in Figure 25 is that the variation in $N(C^{18}O)$ is not due to systematic errors or differences in techniques between the various studies. We have

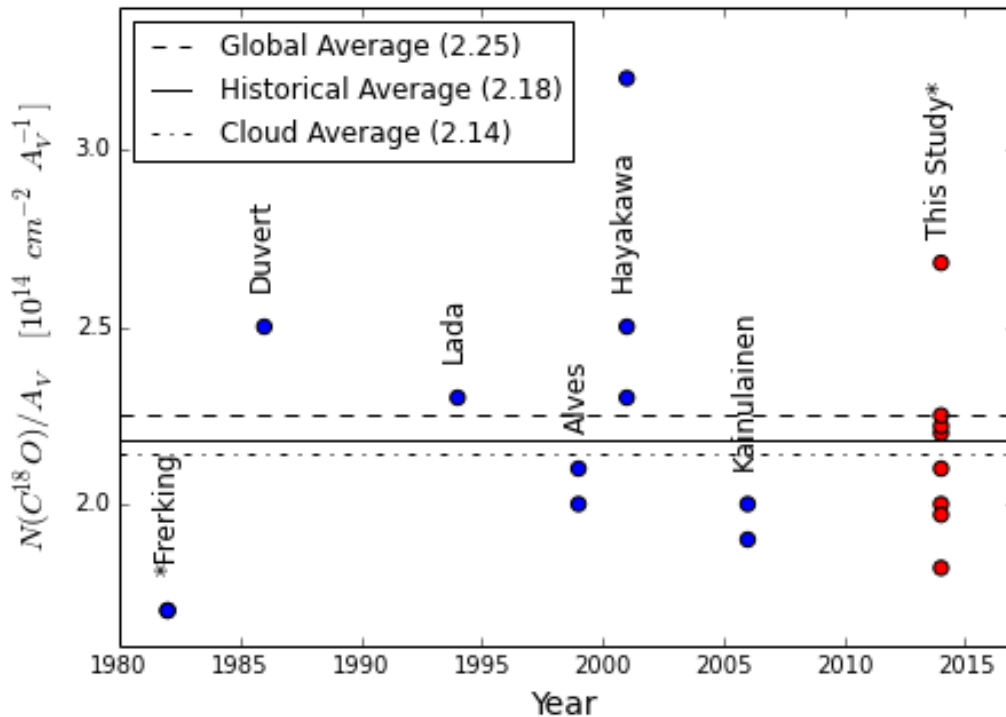


Figure 25: The $N(C^{18}O)/A_V$ relationship of 6 previous studies as given in Table 3 and the 7 regions from this study. The points show the gradient of the $C^{18}O - A_V$ relationship as found by the different studies. The solid line represents the historical average. The dashed line represents the global fit to all $C^{18}O$ data along the L1495-B213 filament, while the dashed-dotted line is the average of the gradient for each of our sub-regions. The differences between the gradients found in previous studies are mirrored in the sub-regions of the L1495-B213 filament. This suggests that both the extra- and intra-cloud environments play a role in determining the strength of the local relationship between $C^{18}O$ and A_V .

shown that all but two¹⁸ of the previously reported $C^{18}O$ abundances fall within the range observed in L1495-B213. The 7 regions that we observed cover the range $1.8 \times 10^{14} < N(C^{18}O)/A_V < 2.7 \times 10^{14} [\text{cm}^{-2} \text{mag}^{-1}]$. This suggests that both the extra- and intra-cloud environments are responsible for the scatter in the previously reported correlations between $C^{18}O$ and H_2 . The average $N(C^{18}O) - A_V$ relationship in L1495-B213, averaged over 7 sub-regions is $N(C^{18}O) = (2.25 \times 10^{14}) \cdot A_V$. Our average value differs by less than 4% from the median of the other studies, namely: 2.25×10^{14} vs $2.18 \times 10^{14} [\text{cm}^{-2} \text{mag}^{-1}]$. We would, therefore, recommend a value of

¹⁸The two are the well-known study by Frerking et al. (1982) and the Chameleon I cloud in Hayakawa et al. (2001).

$2.2 \times 10^{14} [\text{cm}^{-2} \text{ mag}^{-1}]$ for the slope of the $N(C^{18}O) - A_V$ relationship.

Furthermore, our value for $X(^{13}CO/C^{18}O)$ is consistent with previous studies. The isotopologue ratio between the two molecules ^{13}CO and $C^{18}O$ is derived by comparing the two isotopologue ratios $^{12}CO/^{13}CO$ and $C^{16}O/C^{18}O$. For these ratios van Dishoeck and Black (1988) found 55 and 500 respectively, Langer et al. (1987) proposed $^{12}CO/^{13}CO = 80$ and a more recent study (Wilson and Rood, 1994) proposed 77 and 560, giving an $^{13}CO/C^{18}O$ isotopologue ratio of $X(^{13}CO/C^{18}O) = 7.3$. We found a similar value within uncertainties of $X(^{13}CO/C^{18}O) \approx 7.9 \pm 2.5$. If we were to use a naive approach and simply divide the average values along the filament ($X(^{13}CO) = 1.45 \cdot 10^{-6}$ and $X(C^{18}O) = 0.21 \cdot 10^{-6}$), we would find an isotopologue ratio of 6.9. This is still within the uncertainties of the $X(^{13}CO/C^{18}O)$ ratio due to the large scatter seen in figure 20.

7. Summary and conclusions

In this study we aimed to re-investigate the relationship between ^{13}CO , $C^{18}O$ and H_2 in the molecular cloud complex L1495-B213 in Taurus. To this end we have compared extinction maps using the NICER method and the 2MASS catalogue with those published by Lombardi et al. (2010) as well as with maps of $N(^{13}CO)$ and $N(C^{18}O)$ for the L1495-B213 filament and with an $N(^{13}CO)$ map of 30 square degrees surrounding the filament. We found different relationships for $N(^{13}CO) - A_V$ and $N(C^{18}O) - A_V$ for each of the 7 sub-regions studied along the filament. A detailed analysis of why certain clouds have different $N(^{13}CO) - A_V$ and $N(C^{18}O) - A_V$ relationships will be left to later work. Here we have mainly concentrated on describing what we have found along the filament. The main results of our study are summarised below:

1. As described in Section 2 we developed a pipeline that automatically downloads $1^\circ \times 1^\circ$ patches of sky from the 2MASS Point Source Catalogue corresponding to the regions covered by an input table of radio fluxes and coordinates. The pipeline uses the NICER method to determine the average extinction along the lines of sight in the input table. The accuracy of our extinction measurements were very high when compared to the published maps of Lombardi et al. (2010) using the upgraded NICEST technique.
2. Section 5 describes the ridge method for identifying trends that have become hidden by large amounts of noise in a data set. The technique uses the simple assumption that if many measurements are clustered around a single point, then there must be something special about that point. To this end the method creates a surface density for measurements in any 2D plane and searches for the highest density region. From there it follows the path of least gradient, where the path of least gradient in an ideal world is the path taken by a noiseless data set. We applied this technique to the large and extremely noisy data sets for $N(^{13}CO)$ and $N(C^{18}O)$ in order to find the most likely relationship between $N(^{13}CO)$, $N(C^{18}O)$ and A_V . This worked remarkably well for such a simple algorithm. The author intends to develop this method into a robust trend finding algorithm in the future.
3. Although we found several different relationships between $C^{18}O$ and A_V for different sub-regions of the L1495-B213 filament, the best fit to the global data set was:

$$N(C^{18}O) [cm^{-2}] = (2.25 \pm 0.37) \cdot 10^{14} \cdot (A_V - 1.07 \pm 0.60) \quad (51)$$

This is one of our "take home" messages. By using over 14,800 pointings along 4.25 degrees of the filament L1495-B213 and covering 7 individual and very different environments we determined a global average relationship between the

reliable, not easily saturatable $C^{18}O$ and A_V , allowing an easy conversion from $C^{18}O$ ($J = 1 \rightarrow 0$) integrated line intensity to H_2 column density. Furthermore Equation 51 is (to within 4%) the same equation that one finds if one averages out many of the $C^{18}O - A_V$ relationships found by the various different studies from 1982 up to the present day (Table 3 and Figure 25).

4. For the case of the $N(^{13}CO) - N(H_2)$ relationship outside the main body of the filament we found the following two correlations:

$$N(^{13}CO) [cm^{-2}] = (21.5 \pm 2.8) \cdot 10^{14} \cdot (A_V - 0.49 \pm 0.06) \quad (0.6^m < A_V < 1.8^m)$$

$$N(^{13}CO) [cm^{-2}] = (9.9 \pm 3.2) \cdot 10^{14} \cdot (A_V + 1.2 \pm 1.3) \quad (1.8^m < A_V < 5^m)$$

The inner correlation between $N(^{13}CO)$ and A_V for $A_V < 2^m$ was very tight and implied a consistent underlying trend for regions where ^{13}CO emission is optically thin. The outer correlation was reminiscent of the internal scatter seen along the L1495-B213 filament. Along the filament the $^{13}CO - A_V$ best fits varied by up to a factor of 3. This added further weight to the argument that even though ^{13}CO is a more sensitive tracer of dense gas ($A_V > 5^m$) than ^{12}CO and is also almost an order of magnitude more abundant than $C^{18}O$, it is still close to useless at tracing the dense ($A_V > 5^m$) regions of clouds. Its strength lies in tracing the diffuse surroundings of cores and filaments where a large portion of the molecular hydrogen is located.

5. Given that CO and its isotopologues are used to trace H_2 column density inside and outside the Milky Way, the issue of calibrating it is of great importance. Although the quality of data and observations over the last 30 year have increased in leaps and bounds, the fact remains that between clouds and even within clouds there are many different physical processes that alter the appearance of the $^{13}CO - A_V$ and $C^{18}O - A_V$ ratios. This is evident in the large variation in these relationships between different authors. Although tracing methods may be improved by the use of extra information about a cloud's local environment, we have shown through our study of 7 sub-regions that ^{13}CO and $C^{18}O$ line intensities cannot be relied upon for precise ($\sigma < 20\%$) measurements of the H_2 column density for $A_V < 5^m$ and $A_V < 20^m$ respectively.
6. We also determined the average abundances for: $X(^{13}CO) = (1.45 \pm 0.53) \cdot 10^{-6}$ and $X(C^{18}O) = (2.15 \pm 0.64) \cdot 10^{-7}$ inside the filament and $X(^{13}CO) = (1.41 \pm 0.53) \cdot 10^{-6}$ for the diffuse medium surrounding the filament. These abundances are consistent with those found by the other authors listed in Table 3. Figure 13 (Bottom right) shows how the abundances change depending on the cloud location.

7. Throughout the L1495-B213 filament the ratio of ^{13}CO to $C^{18}O$ appears to hover around $X(^{13}CO/C^{18}O) = 7.9$, which is within uncertainties of the literature value of 7.3. There are some local deviations from this value in the different sub-regions but the departure from the average isn't greater than 25%. Furthermore, by using these isotopologue ratios we were able to corroborate the currently held view that the ^{12}CO abundance is approximately $N(^{12}CO)/N(H_2) \approx 10^{-4}$. Our findings showed $N(^{12}CO)/N(H_2)$ equal to $(1.08 \pm 0.39) \cdot 10^{-4}$ for the diffuse surroundings and $(1.2 \pm 0.36) \cdot 10^{-4}$ for the filament.

8. Future work

Our primary goal at the beginning of this study was to revisit the long held standard set down by Frerking et al. (1982) for the relationship between extinction (and by extension hydrogen column density) and the isotopologues ^{13}CO and $C^{18}O$. We hoped to determine whether modern techniques were able to better constrain the relationship, and if not, why not. While the author feels that the results of this study have met these goals, he acknowledges the fact that it has opened a can of worms with regard to directions that this line of research could take in the future. Possible avenues include expanding the field of study and applying the pipeline developed for L1495 to as many other $C^{18}O$ and ^{13}CO data sets as possible. The author would also like to look into using mid infrared photometry from the ALLWISE catalogue (the RJCE method - Majewski et al., 2011) to help constrain the extinction values. Further investigation into the ridge method is also warranted to determine how robust the method is. As of February 2014 dabbling with the method has already produced some encouraging results.

Another avenue the author is investigating is the relationship between the interstellar radiation field and the column density of H_2 required to adequately shield CO and its isotopologues. L1495-B213 is generally accepted to be a very quiet region with little star formation occurring. The small number of YSOs in several of the Barnard regions attests to this. Hence L1495-B213 could almost be seen as a pristine example of the $A_V - C^{18}O$ in molecular clouds. The work by Frerking et al. (1982) showed that in highly irradiated environments (i.e. near ρ Ophiuchii) the $A_V - C^{18}O$ relationship is shifted along the A_V axis. Van Dishoeck and Black (1988) showed that this may be due to the increased UV component of the local radiation field (due to several B-type stars), however, to date this has not been thoroughly investigated. In March 2014 the author submitted a proposal¹⁹ to APEX to take measurements of the $C^{18}O$ emission at 5 points along the L1729 filament in order to determine the radial dependence of the shielding parameter $A_{V,0}$. The author hopes that this may prove to be a viable way to the determine the local radiation field outside a molecular cloud without the need for satellite based UV observations.

¹⁹Proposal 094.C-0844 for the SHFI instrument on APEX

9. Acknowledgements

9.1. Official acknowledgements

This publication makes use of data products from the Two Micron All Sky Survey, which is a joint project of the University of Massachusetts and the Infrared Processing and Analysis Center/California Institute of Technology, funded by the National Aeronautics and Space Administration and the National Science Foundation. This research made use of Astropy, a community-developed core Python package for Astronomy (Astropy Collaboration et al., 2013). This research made use of Montage, funded by the National Aeronautics and Space Administration’s Earth Science Technology Office, Computation Technologies Project, under Cooperative Agreement Number NCC5-626 between NASA and the California Institute of Technology. Montage is maintained by the NASA/IPAC Infrared Science Archive. This research made use of TOPCAT, developed by the Astrophysics Group of the School of Physics, at the University of Bristol, UK (Taylor, 2005).

9.2. Personal acknowledgements

The author wishes to thank Dr A. Hacar and Prof. J. Alves for the numerous hours of discussion, explanations and general motivational talks over the course of this Master’s thesis. Without their help and encouragement this thesis would have taken much much longer to complete. Further thanks are due to Dr J. Forbrich and Dr P. Teixeira for their help with many non-trivial matters as well as to S. Lindner for several insightful discussions regarding code optimization. The author also wishes to thank R. and C. Leschinski, because without their support and encouragement over the past 27 years this thesis would never have become a reality. Last but not most definitely not least are the thanks that I afford E. M. Lindner for her constant, continued and unwaivering support in all things non-astronomical.

“So long and thanks for all the fish” - Douglas Adams

References

- [1] J. Alves, C. J. Lada, and E. A. Lada. “Correlation between Gas and Dust in Molecular Clouds: L977”. In: *The Astrophysical Journal* 515 (Apr. 1999), pp. 265–274. DOI: 10.1086/307003. eprint: astro-ph/9809027.
- [2] J. Alves et al. “Dust Extinction and Molecular Cloud Structure: L977”. In: *The Astrophysical Journal* 506 (Oct. 1998), pp. 292–305. DOI: 10.1086/306243. eprint: astro-ph/9805141.
- [3] Astropy Collaboration et al. “Astropy: A community Python package for astronomy”. In: *Astronomy and Astrophysics* 558, A33 (Oct. 2013), A33. DOI: 10.1051/0004-6361/201322068. arXiv: 1307.6212 [astro-ph.IM].
- [4] E. E. Barnard, E. B. Frost, and M. R. Calvert. *A photographic atlas of selected regions of the Milky way*. 1927.
- [5] E. A. Bergin and M. Tafalla. “Cold Dark Clouds: The Initial Conditions for Star Formation”. In: *Annual Review of Astronomy and Astrophysics* 45 (Sept. 2007), pp. 339–396. DOI: 10.1146/annurev.astro.45.071206.100404. arXiv: 0705.3765.
- [6] R. C. Bohlin, B. D. Savage, and J. F. Drake. “A survey of interstellar H I from L-alpha absorption measurements. II”. In: *The Astrophysical Journal* 224 (Aug. 1978), pp. 132–142. DOI: 10.1086/156357.
- [7] B. J. Bok. “Dark Nebulae, Globules, and Protostars”. In: *Publications of the Astronomical Society of the Pacific* 89 (Oct. 1977), p. 597. DOI: 10.1086/130172.
- [8] B. J. Bok. “Palomar Schmidt star counts for two heavily obscured fields.” In: *Astronomical Journal* 61 (1956), pp. 309–316. DOI: 10.1086/107350.
- [9] B. J. Bok and C. S. Cordwell. “A Study of Dark Nebula”. In: *Molecules in the Galactic Environment*. Ed. by M. A. Gordon and L. E. Snyder. 1973, p. 54.
- [10] B. J. Bok and E. F. Reilly. “Small Dark Nebulae.” In: *The Astrophysical Journal* 105 (Mar. 1947), p. 255. DOI: 10.1086/144901.
- [11] I. A. Bonnell, M. R. Bate, and H. Zinnecker. “On the formation of massive stars”. In: *Monthly Notices of the Royal Astronomical Society* 298 (July 1998), pp. 93–102. DOI: 10.1046/j.1365-8711.1998.01590.x. eprint: astro-ph/9802332.
- [12] J. A. Cardelli, G. C. Clayton, and J. S. Mathis. “The relationship between infrared, optical, and ultraviolet extinction”. In: *The Astrophysical Journal* 345 (Oct. 1989), pp. 245–256. DOI: 10.1086/167900.
- [13] M. S. Cord, M. S. Lojko, and J. D. Petersen. *Microwave spectral tables, spectral line listing*. 1968.
- [14] I. Dabrowski. “The Lyman and Werner bands of H₂”. In: *Canadian Journal of Physics* 62 (Dec. 1984), pp. 1639–1664. DOI: 10.1139/p84-210.

- [15] T. M. Dame, D. Hartmann, and P. Thaddeus. “The Milky Way in Molecular Clouds: A New Complete CO Survey”. In: *Astrophysical Journal* 547 (Feb. 2001), pp. 792–813. DOI: 10.1086/318388. eprint: astro-ph/0009217.
- [16] T. M. Dame et al. “A composite CO survey of the entire Milky Way”. In: *Astrophysical Journal* 322 (Nov. 1987), pp. 706–720. DOI: 10.1086/165766.
- [17] J. F. Dean, P. R. Warren, and A. W. J. Cousins. “Reddenings of Cepheids using BVI photometry”. In: *Monthly Notices of the Royal Astronomical Society* 183 (June 1978), pp. 569–583.
- [18] R. L. Dickman. “Star counts and visual extinctions in dark nebulae”. In: *Astronomical Journal* 83 (Apr. 1978), pp. 363–372. DOI: 10.1086/112212.
- [19] G. Duvert, J. Cernicharo, and A. Baudry. “A molecular survey of three dark clouds in Taurus”. In: *Astronomy and Astrophysics* 164 (Aug. 1986), pp. 349–357.
- [20] J. H. Elias. “A study of the IC 5146 dark cloud complex”. In: *The Astrophysical Journal* 223 (Aug. 1978), pp. 859–861. DOI: 10.1086/156319.
- [21] J. H. Elias. “A study of the Taurus dark cloud complex”. In: *The Astrophysical Journal* 224 (Sept. 1978), pp. 857–872. DOI: 10.1086/156436.
- [22] M. A. Frerking, W. D. Langer, and R. W. Wilson. “The relationship between carbon monoxide abundance and visual extinction in interstellar clouds”. In: *The Astrophysical Journal* 262 (Nov. 1982), pp. 590–605. DOI: 10.1086/160451.
- [23] P. F. Goldsmith et al. “Large-Scale Structure of the Molecular Gas in Taurus Revealed by High Linear Dynamic Range Spectral Line Mapping”. In: *The Astrophysical Journal* 680 (June 2008), pp. 428–445. DOI: 10.1086/587166. arXiv: 0802.2206.
- [24] A. Hacar et al. “Cores, filaments, and bundles: hierarchical core formation in the L1495/B213 Taurus region”. In: *Astronomy and Astrophysics* 554, A55 (June 2013), A55. DOI: 10.1051/0004-6361/201220090. arXiv: 1303.2118 [astro-ph.GA].
- [25] L. Hartmann, J. Ballesteros-Paredes, and E. A. Bergin. *Rapid Formation of Molecular Clouds and Stars in the Solar Neighborhood*. Vol. 562. Dec. 2001, pp. 852–868. DOI: 10.1086/323863. eprint: astro-ph/0108023.
- [26] T. Hayakawa et al. “CO Column Density and Extinction in the Chamaeleon II–III Dark-Cloud Complex”. In: *Publications of the Astronomical Society of Japan* 53 (Dec. 2001), pp. 1109–1118.
- [27] K. B. Jefferts et al. “Interstellar carbon monoxide.” In: *IAU Circulars* 2231 (1970), p. 1.
- [28] J. Kainulainen, K. Lehtinen, and J. Harju. “The ratio of $N(C^{18}O)$ and A_V in Chamaeleon I and III-B. Using 2MASS and SEST”. In: *Astronomy and Astrophysics* 447 (Feb. 2006), pp. 597–607. DOI: 10.1051/0004-6361:20053593. eprint: astro-ph/0510342.

- [29] M. R. Krumholz, A. K. Leroy, and C. F. McKee. “Which Phase of the Interstellar Medium Correlates with the Star Formation Rate?” In: *The Astrophysical Journal* 731, 25 (Apr. 2011), p. 25. DOI: 10.1088/0004-637X/731/1/25. arXiv: 1101.1296 [astro-ph.CO].
- [30] C. J. Lada et al. “Dust extinction and molecular gas in the dark cloud IC 5146”. In: *The Astrophysical Journal* 429 (July 1994), pp. 694–709. DOI: 10.1086/174354.
- [31] W. D. Langer, A. E. Glassgold, and R. W. Wilson. “Radio observations of carbon monoxide toward Zeta Ophiuchi - Velocity structure, isotopic abundances, and physical properties”. In: *The Astrophysical Journal* 322 (Nov. 1987), pp. 450–462. DOI: 10.1086/165741.
- [32] T. A. Lee. “Interstellar extinction in the Orion association”. In: *The Astrophysical Journal* 152 (June 1968), p. 913. DOI: 10.1086/149607.
- [33] M. Lombardi. “nicest, a near-infrared color excess method tailored to small-scale structures”. In: *Astronomy and Astrophysics* 493 (Jan. 2009), pp. 735–745. DOI: 10.1051/0004-6361:200810519. arXiv: 0809.3383.
- [34] M. Lombardi and J. Alves. “Mapping the interstellar dust with near-infrared observations: An optimized multi-band technique”. In: *Astronomy and Astrophysics* 377 (Oct. 2001), pp. 1023–1034. DOI: 10.1051/0004-6361:20011099. eprint: astro-ph/0109135.
- [35] M. Lombardi, J. Alves, and C. J. Lada. “2MASS wide field extinction maps. I. The Pipe nebula”. In: *Astronomy and Astrophysics* 454 (Aug. 2006), pp. 781–796. DOI: 10.1051/0004-6361:20042474. eprint: astro-ph/0606670.
- [36] M. Lombardi, C. J. Lada, and J. Alves. “2MASS wide field extinction maps. III. The Taurus, Perseus, and California cloud complexes”. In: *Astronomy and Astrophysics* 512, A67 (Mar. 2010), A67. DOI: 10.1051/0004-6361/200912670.
- [37] B. T. Lynds. “Catalogue of Dark Nebulae.” In: *The Astrophysical Journal Supplements* 7 (May 1962), p. 1. DOI: 10.1086/190072.
- [38] S. R. Majewski, G. Zasowski, and D. L. Nidever. “Lifting the Dusty Veil with Near- and Mid-infrared Photometry. I. Description and Applications of the Rayleigh-Jeans Color Excess Method”. In: *The Astrophysical Journal* 739, 25 (Sept. 2011), p. 25. DOI: 10.1088/0004-637X/739/1/25. arXiv: 1106.2542 [astro-ph.GA].
- [39] T. Onishi et al. “A C 18O Survey of Dense Cloud Cores in Taurus: Core Properties”. In: *The Astrophysical Journal* 465 (July 1996), p. 815. DOI: 10.1086/177465.
- [40] F. Palla and S. W. Stahler. “Star Formation in Space and Time: Taurus-Auriga”. In: *The Astrophysical Journal* 581 (Dec. 2002), pp. 1194–1203. DOI: 10.1086/344293. eprint: astro-ph/0208554.
- [41] P. Palmeirim et al. “Herschel view of the Taurus B211/3 filament and striations: evidence of filamentary growth?” In: *Astronomy and Astrophysics* 550, A38 (Feb. 2013), A38. DOI: 10.1051/0004-6361/201220500. arXiv: 1211.6360 [astro-ph.SR].

- [42] G. L. Pilbratt et al. “Herschel Space Observatory. An ESA facility for far-infrared and submillimetre astronomy”. In: *Astronomy and Astrophysics* 518, L1 (July 2010), p. L1. DOI: 10.1051/0004-6361/201014759. arXiv: 1005.5331 [astro-ph.IM].
- [43] J. E. Pineda, P. Caselli, and A. A. Goodman. “CO Isotopologues in the Perseus Molecular Cloud Complex: the X-factor and Regional Variations”. In: *The Astrophysical Journal* 679 (May 2008), pp. 481–496. DOI: 10.1086/586883. arXiv: 0802.0708.
- [44] J. L. Pineda et al. “The Relation Between Gas and Dust in the Taurus Molecular Cloud”. In: *The Astrophysical Journal* 721 (Sept. 2010), pp. 686–708. DOI: 10.1088/0004-637X/721/1/686. arXiv: 1007.5060 [astro-ph.GA].
- [45] L. M. Rebull et al. “The Taurus Spitzer Survey: New Candidate Taurus Members Selected Using Sensitive Mid-Infrared Photometry”. In: *The Astrophysical Journal Supplement* 186 (Feb. 2010), pp. 259–307. DOI: 10.1088/0067-0049/186/2/259. arXiv: 0911.3176 [astro-ph.SR].
- [46] G. H. Rieke and M. J. Lebofsky. “The interstellar extinction law from 1 to 13 microns”. In: *The Astrophysical Journal* 288 (Jan. 1985), pp. 618–621. DOI: 10.1086/162827.
- [47] K. Rohlfs and T. L. Wilson. *Tools of radio astronomy*. 2004.
- [48] D. J. Schlegel, D. P. Finkbeiner, and M. Davis. “Maps of Dust Infrared Emission for Use in Estimation of Reddening and Cosmic Microwave Background Radiation Foregrounds”. In: *The Astrophysical Journal* 500 (June 1998), p. 525. DOI: 10.1086/305772. eprint: astro-ph/9710327.
- [49] M. Schmalzl et al. “Star Formation in the Taurus Filament L 1495: From Dense Cores to Stars”. In: *The Astrophysical Journal* 725 (Dec. 2010), pp. 1327–1336. DOI: 10.1088/0004-637X/725/1/1327. arXiv: 1010.2755 [astro-ph.GA].
- [50] S. Schneider and B. G. Elmegreen. “A catalog of dark globular filaments”. In: *The Astrophysical Journal Supplements* 41 (Sept. 1979), pp. 87–95. DOI: 10.1086/190609.
- [51] F. H. Shu. “Self-similar collapse of isothermal spheres and star formation”. In: *The Astrophysical Journal* 214 (June 1977), pp. 488–497. DOI: 10.1086/155274.
- [52] F. H. Shu, F. C. Adams, and S. Lizano. “Star formation in molecular clouds - Observation and theory”. In: *Annual reviews of Astronomy and Astrophysics* 25 (1987), pp. 23–81. DOI: 10.1146/annurev.aa.25.090187.000323.
- [53] M. F. Skrutskie et al. “The Two Micron All Sky Survey (2MASS)”. In: *Astronomical Journal* 131 (Feb. 2006), pp. 1163–1183. DOI: 10.1086/498708.
- [54] M. B. Taylor. “TOPCAT STIL: Starlink Table/VOTable Processing Software”. In: *Astronomical Data Analysis Software and Systems XIV*. Ed. by P. Shopbell, M. Britton, and R. Ebert. Vol. 347. Astronomical Society of the Pacific Conference Series. Dec. 2005, p. 29.
- [55] R. J. Trumpler. “Absorption of Light in the Galactic System”. In: *Publications of the Astronomical Society of the Pacific* 42 (Aug. 1930), p. 214. DOI: 10.1086/124039.

- [56] E. F. van Dishoeck and J. H. Black. “The photodissociation and chemistry of interstellar CO”. In: *The Astrophysical Journal* 334 (Nov. 1988), pp. 771–802. DOI: 10.1086/166877.
- [57] P. J. van Rhijn. “Distribution of Stars According to Apparent Magnitude, Galactic Latitude and Galactic Longitude”. In: *Publications of the Kapteyn Astronomical Laboratory Groningen* 43 (1929), pp. 1–104.
- [58] R. W. Wilson, K. B. Jefferts, and A. A. Penzias. “Carbon Monoxide in the Orion Nebula”. In: *The Astrophysical Journal* 161 (July 1970), p. L43. DOI: 10.1086/180567.
- [59] T. L. Wilson and R. Rood. “Abundances in the Interstellar Medium”. In: *Astronomy and Astrophysics Annual Reviews* 32 (1994), pp. 191–226. DOI: 10.1146/annurev.aa.32.090194.001203.
- [60] G. Zasowski et al. “Lifting the Dusty Veil with Near- and Mid-Infrared Photometry. II. A Large-Scale Study of the Galactic Infrared Extinction Law”. In: *The Astrophysical Journal* 707 (Dec. 2009), pp. 510–523. DOI: 10.1088/0004-637X/707/1/510. arXiv: 0910.4403 [astro-ph.GA].

Appendices

A. Maps

A.1. L1495-B213 filament maps

The maps presented here are the full page versions of those shown in Figure 13.

A.1.1. Extinction map - A_V

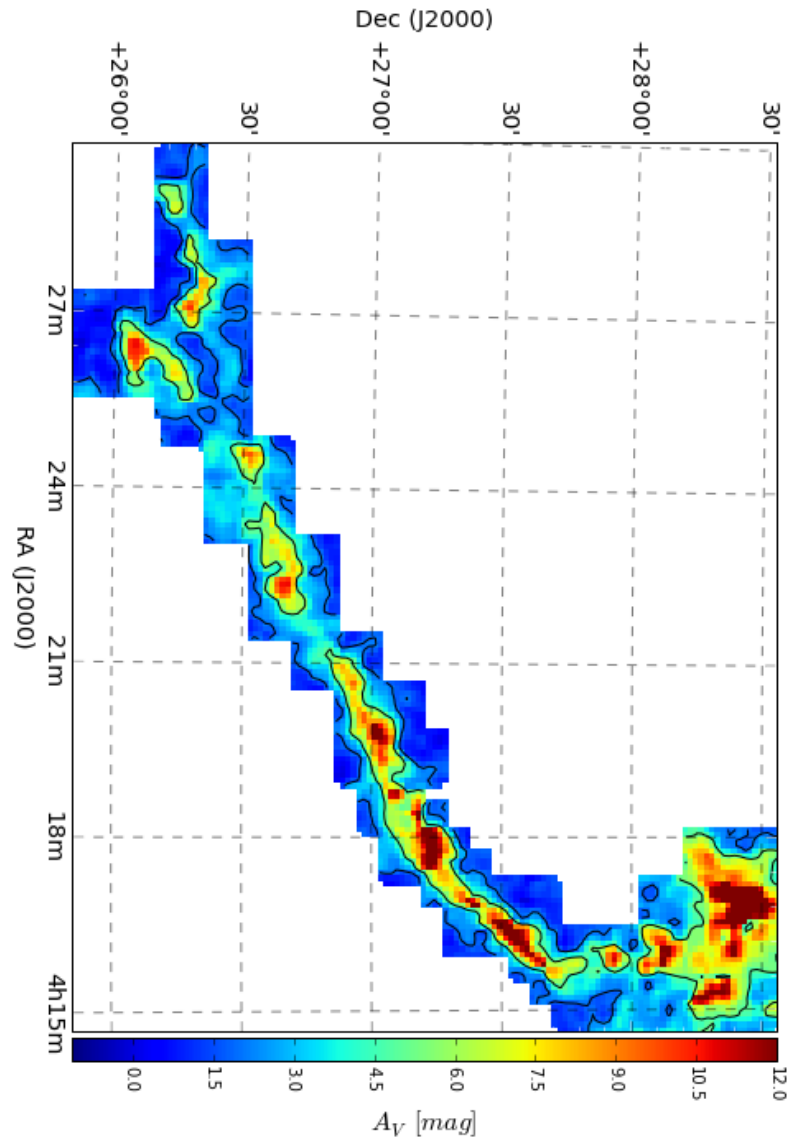


Figure 26: Extinction, A_V . Contours: $A_V = [2^m, 5^m]$. The section of the extinction map corresponding to the L1495-B213 filament as published by Lombardi et al. (2010). Contours are set to help the eye differentiate between regions where; the ISM is sparse ($A_V < 2^m$) - dark blue, the ISM is diffuse ($2^m < A_V < 5^m$) in the envelope of the cloud - light blue and turquoise, and where the cloud is at its densest ($A_V > 5^m$) - yellow and red.

A.1.2. Column density map - $N(^{13}CO)$

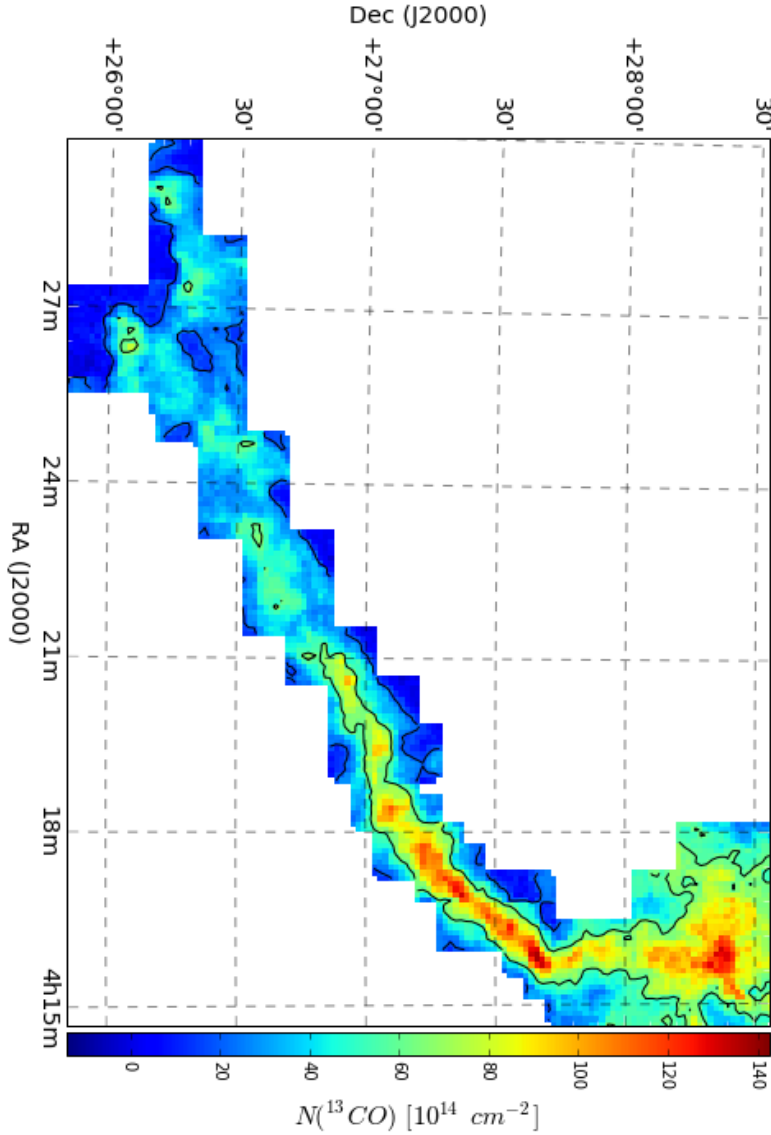


Figure 27: ^{13}CO Column Density. Contours: $N(^{13}CO) = [20, 60] \times 10^{14} \text{ cm}^2$. $N(^{13}CO)$ column densities were derived from the integrated flux measurements from Goldsmith et al., 2008. The contours show the usable limits ^{13}CO emission. The lower limit ($N(^{13}CO) = 20 \cdot 10^{14} \text{ cm}^2$) corresponds to the density need to adequately shield ^{13}CO from the ISRF. The upper limit ($N(^{13}CO) = 60 \cdot 10^{14} \text{ cm}^2$) shows the regions where ^{13}CO is no longer optical thin ($A_V > 5^m$) and no longer be trusted to show a linear correlation to $N(H_2)$.

A.1.3. Column density map - $N(C^{18}O)$

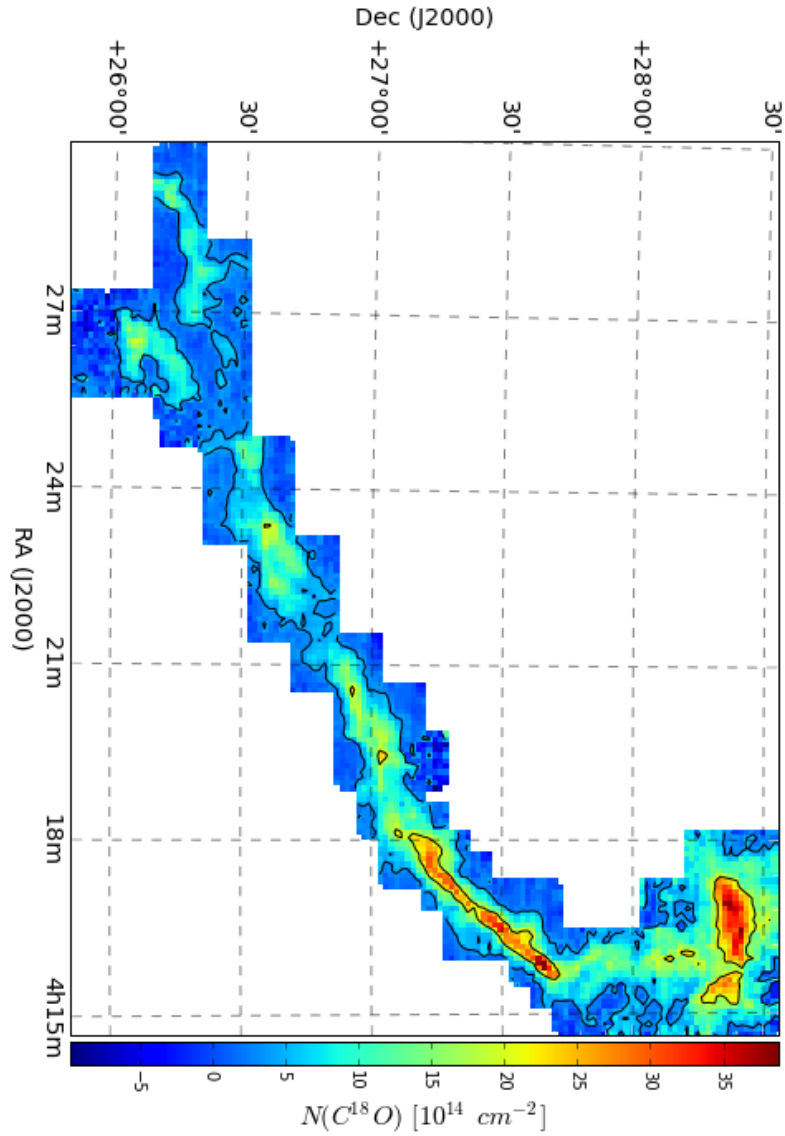


Figure 28: $C^{18}O$ Column Density. Contours: $N(C^{18}O) = [4, 20] \times 10^{14} \text{ cm}^{-2}$. $N(C^{18}O)$ column densities were derived from the integrated flux measurements from Hacar et al. (2013). The lowest contour shows the border between the regions where the $C^{18}O$ is not sufficiently shielded from the ISRF (blue) and where it is sufficiently shielded (turquoise). This corresponds to an extinction of $A_V \approx 2^m$. The upper contour shows the truly dense gas $A_V > 8^m$. The higher dynamic range of $C^{18}O$ is seen by the spatial thinness of the densest regions when compared to ^{13}CO , however the usable region is by far smaller in size than that of ^{13}CO .

A.1.4. Abundance map - $X(^{13}CO)$

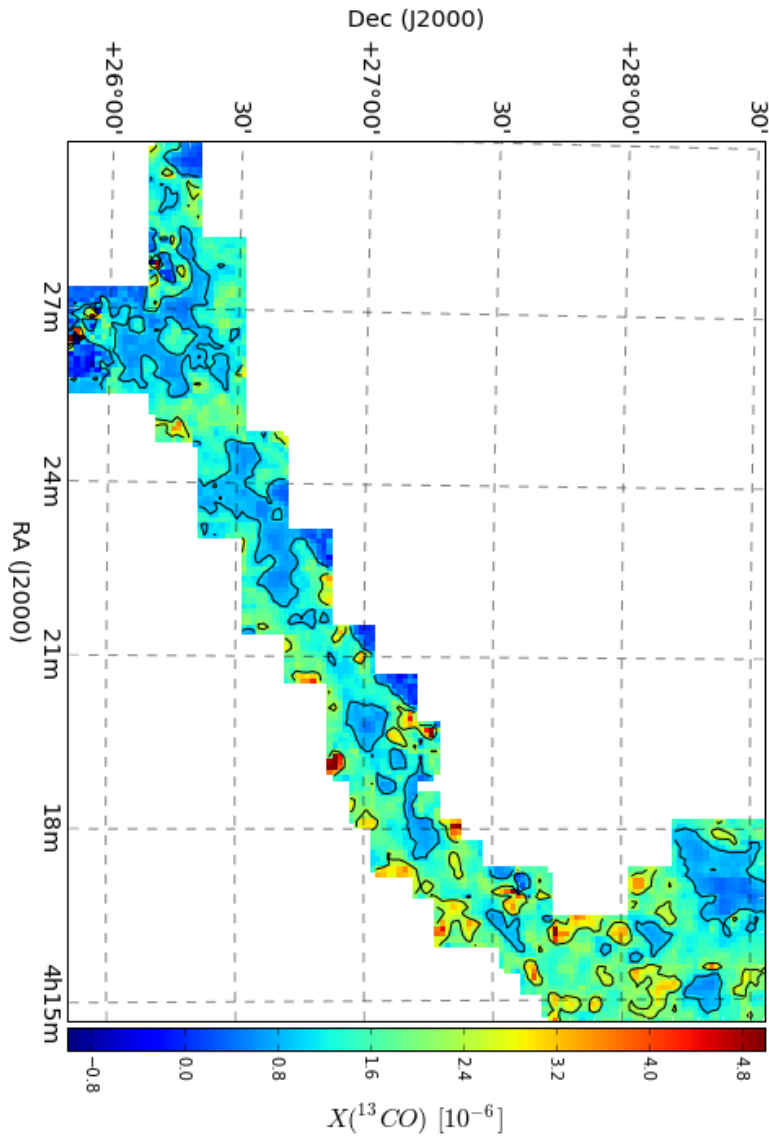


Figure 29: ^{13}CO Abundance. Contours: $X(^{13}CO) = [1, 2.25] \times 10^{-6}$. The contours are set to 66% and 150% of the average abundance along the L1495-B213 filament. The blue regions are areas where $X(^{13}CO)$ is lower than 66% of the average. These regions correspond to the peaks in extinction and are caused by the saturation of ^{13}CO .

A.1.5. Abundance map - $X(C^{18}O)$

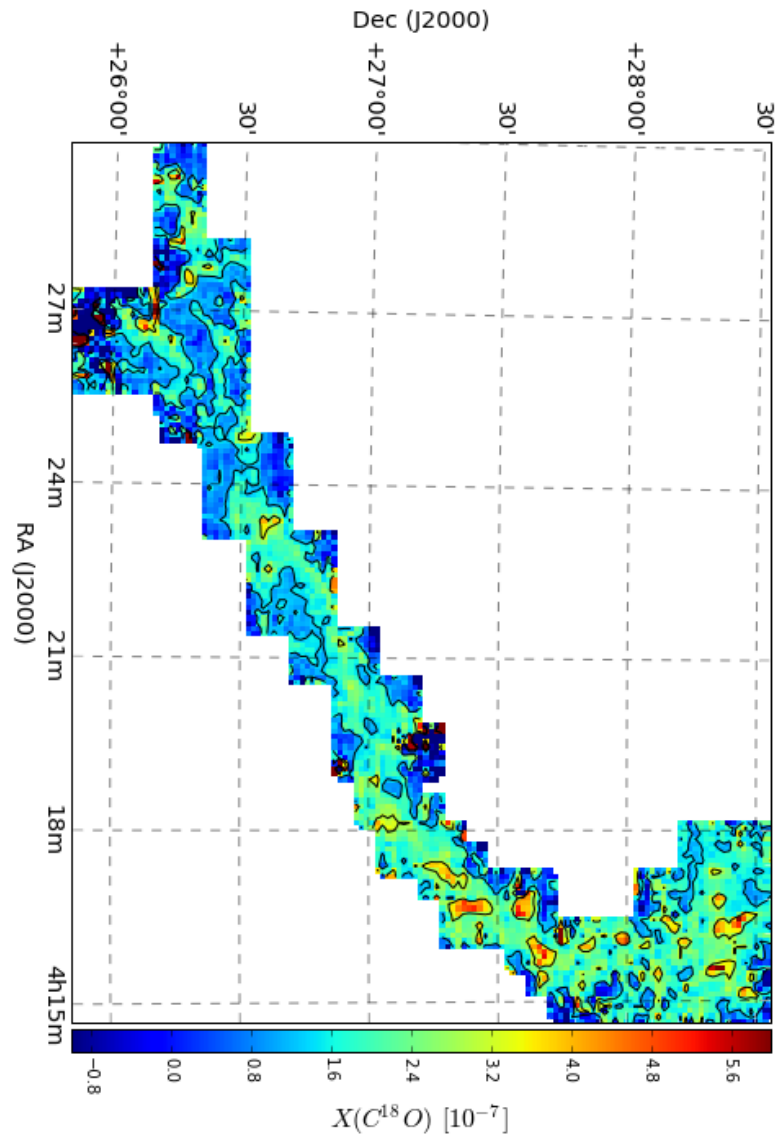


Figure 30: $C^{18}O$ Abundance. Contours: $X(C^{18}O) = [1.33, 3] \times 10^{-7}$. The contours are set to 66% and 150% of the average abundance along the L1495-B213 filament. $C^{18}O$ doesn't saturate in the regime that we are able to probe ($A_V < 25^m$) and consequently $X(C^{18}O)$ is more constant along the L1495-B213 filament.

A.1.6. Isotopologue abundance map - $N(^{13}CO)/N(C^{18}O)$

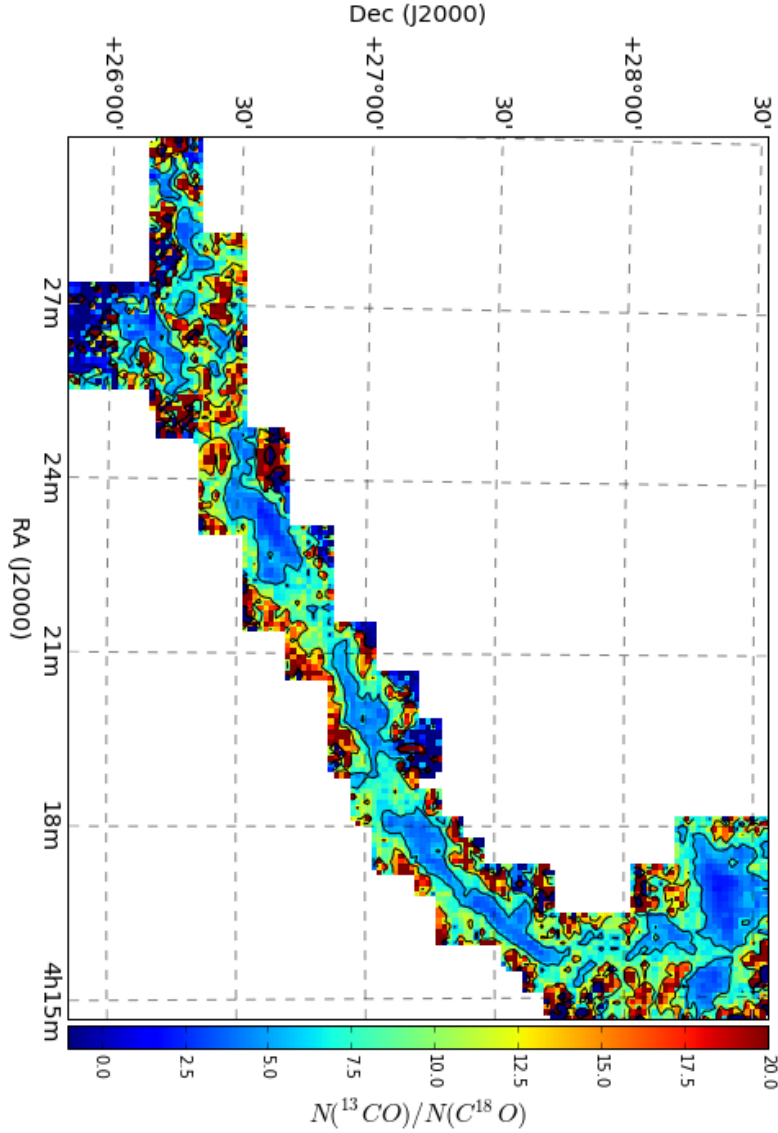


Figure 31: Isotopologue Ratio. Contours: $X(^{13}CO/C^{18}O) = [6, 12]$. The dark blue regions are where ^{13}CO is saturated. The dark red regions are regions of sparse and very diffuse gas ($A_V < 2$) where $C^{18}O$ abundances suffer due to the interstellar radiation field. Turquoise shows the thin regions at the edge of the filament where ^{13}CO is not yet saturated, but the column density is high enough for $C^{18}O$ to be shielded from the ISRF. In these turquoise regions, both isotopologues are protected from the ISRF and are optically thin, making only these regions suitable for determining the relative abundance ratio between the two species.

A.2. Surrounding region maps

The maps presented here are the full page versions of those shown in Figure 14.

A.2.1. Extinction Map - A_V

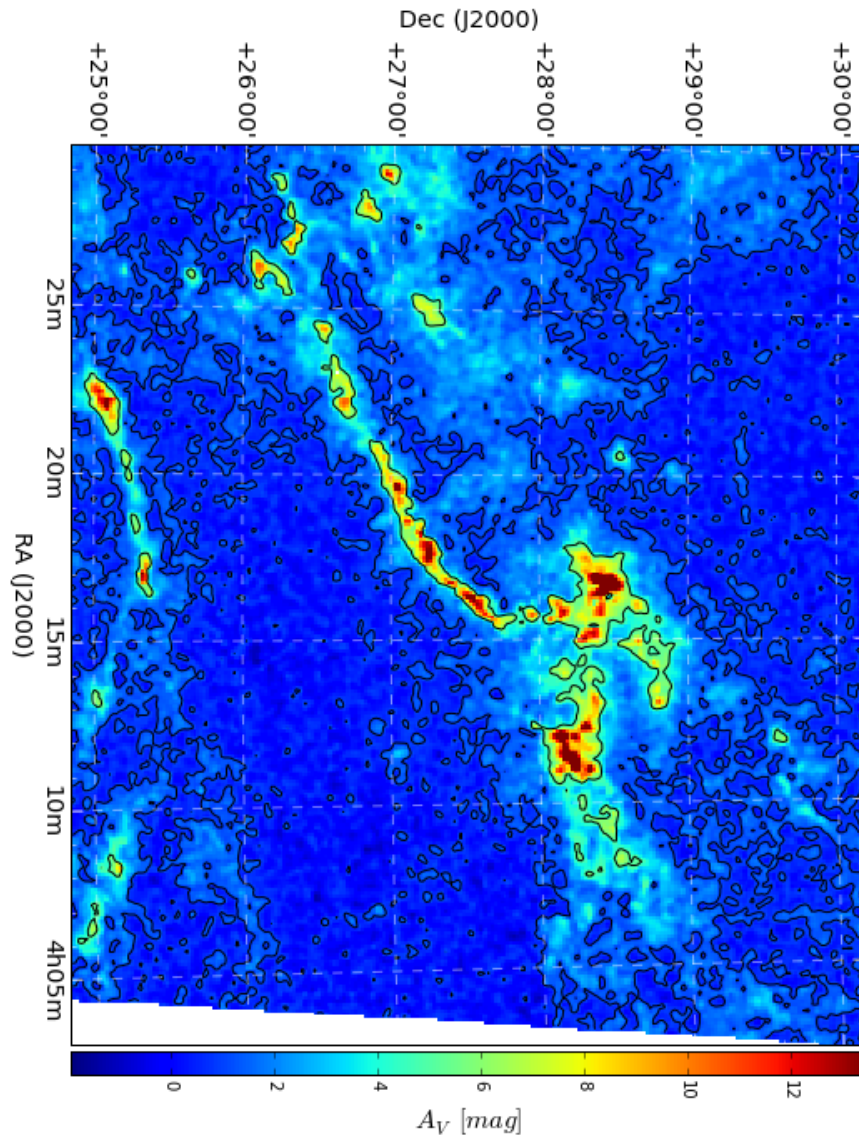


Figure 32: Extinction, A_V . Contours: $A_V = [1, 5]$ mag. The section of the extinction map surrounding the L1495-B213 filament as published by Lombardi et al. (2010). As with the extinction map in Appendix A.1.1, the contours are set to help the eye differentiate between regions where; the ISM is sparse ($A_V < 1^m$) - dark blue, the ISM is diffuse ($1^m < A_V < 5^m$) in the envelope of the cloud - light blue and turquoise, and where the cloud is at its densest ($A_V > 5^m$) - yellow and red.

A.2.2. Column density map - $N(^{13}CO)$

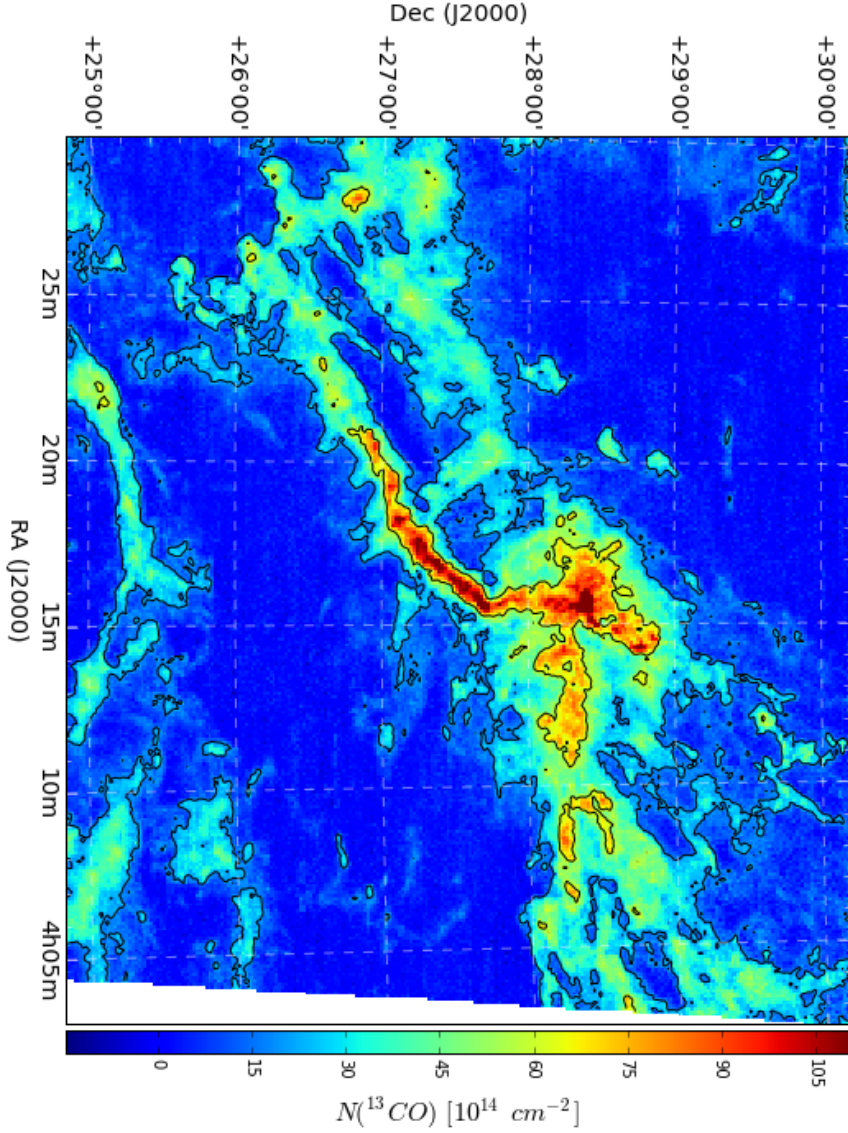


Figure 33: ^{13}CO Column Density. Contours: $N(^{13}CO) = [20, 60] \times 10^{14} \text{ cm}^2$. $N(^{13}CO)$ column densities were derived from the integrated flux measurements from Goldsmith et al., 2008. The contours show the usable limits ^{13}CO emission. The lower limit ($N(^{13}CO) = 20 \times 10^{14} \text{ cm}^2$) corresponds to the density need to adequately shield ^{13}CO from the ISRF. The upper limit ($N(^{13}CO) = 60 \times 10^{14} \text{ cm}^2$) shows the regions where ^{13}CO is no longer optical thin ($A_V > 5^m$) and no longer displays a linear correlation to $N(H_2)$.

A.2.3. Abundance map - $X(^{13}CO)$

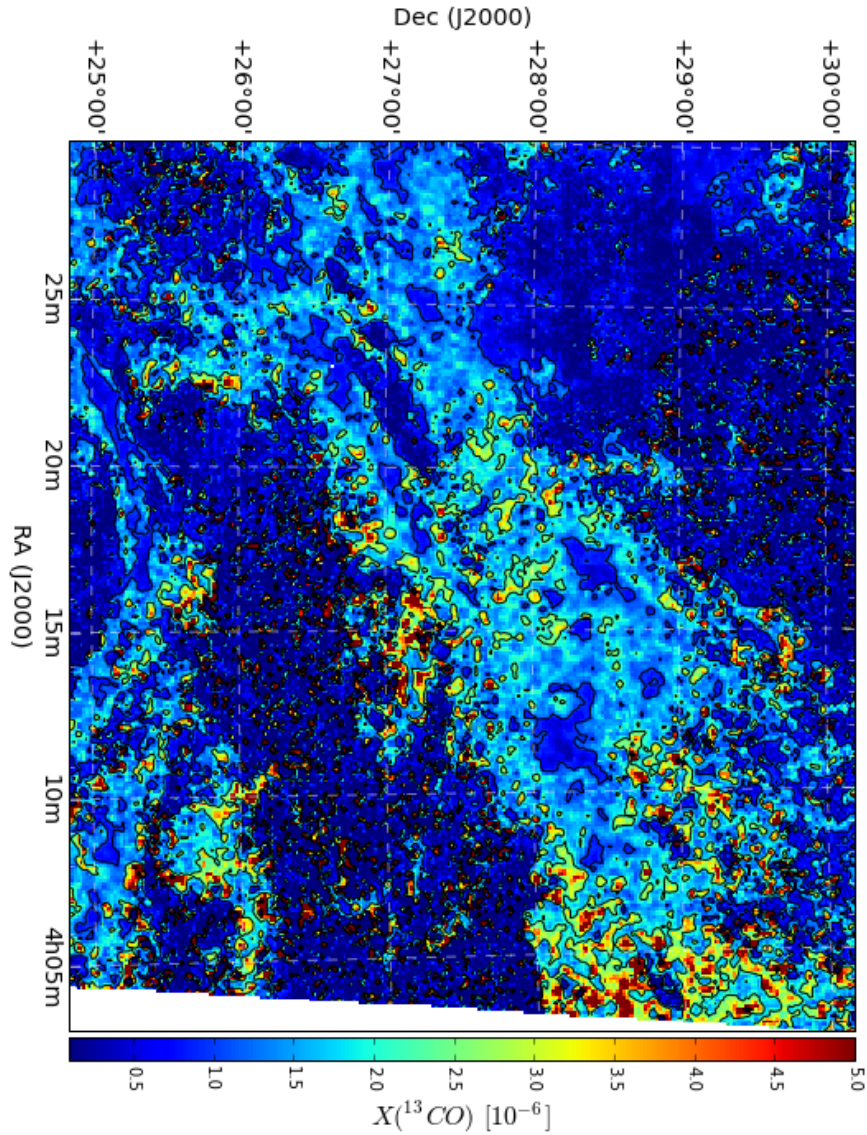


Figure 34: ^{13}CO Abundance. Contours: $X(^{13}CO) = [1, 2.25] \times 10^{-6}$. The contours are set to approximately 66% and 150% of the average abundance around the L1495-B213 filament. The blue regions are areas where $X(^{13}CO)$ is lower than 66% of the average. As expected in the range $1^m < A_V < 5^m$, $X(^{13}CO)$ remains relatively constant, effectively displaying the regions where the ISM is dense enough for a stable population of ^{13}CO to be sufficiently shielded against the ISRF.

B. Python notebook for generating extinction values and comparative data sets

Pipeline A - Find A_V for a CO dataset using NICER

+++++

Before using this pipeline, all functions at the bottom of the file need to be executed

+++++

Taking a single CO data set, consisting of 3 columns: RA, Dec and Flux, this script generates extinction values for the same pointings. The steps in this process are:

- 1 - Read in the CO data table
- 2 - Find the spatial extremes of the CO data and work out which 1 deg x 1 deg tiles need to be accessed
- 3 - Check to see if they exist on the hard drive. If not, download them from IRSA
- 4 - Create an extinction value for each pointing based on stars within a radius "res" of the pointing
- 5 - Output a table with the values: RA, Dec, CO, A_V , dA_V , NCO, NH₂, XCO

User Input

CO data set file name: "CName"

Resolution (in deg): "res"

Central RA and Dec coords (in deg): "centre"

Flag for plotting (1 or 0): "test"

```
In [8]: CName="L1495_C180_75_raw.dat"
        res=75/3600.                #[in degrees]
        centre=(15.*(4+17/60.+47.08/3600.),27.+37/60.+18.4/3600.)  #[in degrees]
        test=1
        print "Centred at ",centre
        Centred at (64.44616666666667, 27.62177777777778)
```

1 - Read in the CO data table

The radio data is most likely to be in Radio coordinates and with ra and dec offsets in arcseconds. Therefore in order to find the corresponding 2MASS stars for each pixel, the offsets need to have a corresponding real world coordinate. This is done using the following formulae:

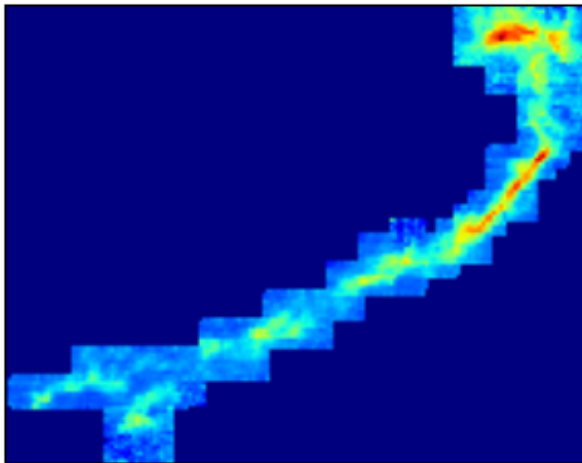
$$\alpha = \alpha_{centre} + \frac{d\alpha}{\cos(\delta_{centre})}$$

$$\delta = \delta_{centre} + d\delta$$

```
In [10]: # read in the CO data
raw_CO=ascii.read(COname)

# convert the raw offsets to actual coordinates
ra=raw_CO["ra"]/3600./np.cos(np.pi*centre[1]/180)+centre[0]
dec=raw_CO["dec"]/3600.+centre[1]
flux=raw_CO["flux"]

#We shall plot the input data to make sure it is what we want.
if test:
    plt.imshow(make_map(ra,dec,flux,res))
    plt.gca().invert_yaxis()
    plt.gca().invert_xaxis()
    plt.gca().get_xaxis().set_visible(False)
    plt.gca().get_yaxis().set_visible(False)
```



2 - Find the spatial extremes of the CO data and work out which 1 deg x 1 deg tiles need to be accessed

In order to determine which fields need to be downloaded we need to find the min and max spatial values of the data set. We then make a 2D histogram and pass the edge of each tile (ie exact degree values, eg ra=[64,65,66]) as bin edge coordinates. This gives us an array of dRA x dDec degrees and a list of coordinates that need to be queried.

```
In [11]: # get a list of tiles that should be asked for from 2MASS
ra_sq_cen =range(int(np.min(ra)),int(np.max(ra)+2))
if np.min(dec)>0.: dec_sq_cen=range(int(np.min(dec)),int(np.max(dec)+2))
elif np.max(dec)<0.: dec_sq_cen=range(int(np.min(dec))-1,int(np.max(dec)+1))
else: dec_sq_cen=range(int(np.min(dec))-1,int(np.max(dec)+2))
```

```

# make a 2d histogram centred on each pixel
radio_area=np.histogram2d(ra,dec,bins=[ra_sq_cen,dec_sq_cen])[0]
radio_area[radio_area>=1]=1
no_tiles = np.sum(radio_area)

print "The region to be covered"
print np.fliplr(np.rot90(radio_area))
print "Extent of RA and Dec coords: ",ra_sq_cen,dec_sq_cen
print "Extreme coordinates, RA: ",np.min(ra),np.max(ra),"Dec: ",np.min(dec),n
p.max(dec)
print "Central coordinates:", centre
if test:
    plt.imshow(np.fliplr(np.rot90(radio_area)))
    plt.gca().get_xaxis().set_visible(False)
    plt.gca().get_yaxis().set_visible(False)

```

The region to be covered

```

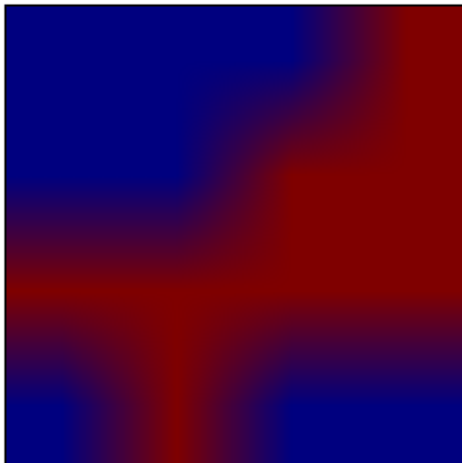
[[ 0.  0.  0.  1.]
 [ 0.  0.  1.  1.]
 [ 1.  1.  1.  1.]
 [ 0.  1.  0.  0.]]

```

Extent of RA and Dec coords: [64, 65, 66, 67, 68] [25, 26, 27, 28, 29]

Extreme coordinates, RA: 64.1522517595 67.5499080864 Dec: 25.8717777778 28.5488611111

Central coordinates: (64.44616666666667, 27.62177777777778)



3 - Check to see if they exist on the hard drive, if not download them from IRSA

Using the range of degrees in RA and Dec to be covered (ra_sq_cen, dec_sq_cen) and the coverage map (radio_area), we pull in either the data in 1.1 x 1.1 deg squares from the hard disk, or we query the online 2MASS catalogue at IRSA for the data.

```

In [12]: # make an list to contain all the tiles
irsas_cat=range(int(np.sum(radio_area)))

```

```

irsa_legend=r(irsa_cat)
print no_tiles, "square degrees will be loaded"

# either read from file or ask IRSA for the data
# cycle through radio_area array, and if the tile has been deemed needed,
#ie, radio_area[i,j]==1, load it. Otherwise, skip the region
k=0
for i in range(len(ra_sq_cen)-1):
    for j in range(len(dec_sq_cen)-1):
        if radio_area[i,j]:

            # load in the wanted tile. query_2MASS_psc check the hard disk
            # first, then online
            print int(((k+1)/no_tiles)*100), "%"
            irsa_cat[k] = query_2MASS_psc(float(ra_sq_cen[i])+0.5,
                                         float(dec_sq_cen[j])+0.5,4200)

            if np.min(dec)>0.:
                irsa_legend[k] = (ra_sq_cen[i],dec_sq_cen[j])
            elif np.max(dec)<0.:
                irsa_legend[k] = (ra_sq_cen[i],dec_sq_cen[j+1])
            else:
                print "ARGH! Region over the ecliptic! Deal with it!"

            irsa_cat[k]=flag_check(irsa_cat[k])

            k=k+1

```

```

8.0 square degrees will be loaded
12 %
    ./irsa/64.5+26.5.irsa exists. Reading in the file
25 %
    ./irsa/64.5+27.5.irsa exists. Reading in the file
37 %
    ./irsa/64.5+28.5.irsa exists. Reading in the file
50 %
    ./irsa/65.5+26.5.irsa exists. Reading in the file
62 %
    ./irsa/65.5+27.5.irsa exists. Reading in the file
75 %
    ./irsa/66.5+25.5.irsa exists. Reading in the file
87 %
    ./irsa/66.5+26.5.irsa exists. Reading in the file
100 %
    ./irsa/67.5+26.5.irsa exists. Reading in the file

```

4 - Create an extinction value for each pointing based on stars within a radius "res" of the pointing

We work through the tiles and assign an extinction to each star

```
In [13]: for i in r(irsacat):
          if "av" not in irsacat[i].colnames:
              # the NICER_AV() function applies NICER to each star, to find Av
              Av_data=NICER_AV(irsacat[i])
              irsacat[i].add_column(table.Column(data=Av_data[2,:], name='av'))
              irsacat[i].add_column(table.Column(data=Av_data[3,:],
                                                  name='av_std'))
```

Now we work out an average extinction for every pixel in the radio map

Find the nearest stars - to within a radius of $2 \times \text{res}$ of the radio pixel centre - and gaussian weight their Av values. Then sum up the weighted Av values to find an average value for each radio pixel

- 1 - Cycle through each pixel in the radio map
- 2 - Find the stars that are within a radius of $2 \times \text{res}$
- 3 - for each star, weight its Av value by using the inverse of its distance.
- 4 - Sum up the weighted Avs for an averaged value

```
In [21]: # a radius of 2*res, ie 150" is sampled around the pixel centre for stars.
          # res = the niquist footprint of the pixel is a radius "res" around the pixel
          centre.

          radio_data=np.asarray((ra,dec,flux))

          w=r(radio_data[0,:])
          radio_Av=r(radio_data[0,:])
          Av_median=np.zeros((len(radio_data[0,:])))
          Av_sig=np.zeros((len(radio_data[0,:])))
          Av_n=np.zeros((len(radio_data[0,:])))

          # cycle through each pixel in the radio data and work out an Av for the pixel
          for i in r(radio_data[0,:]):
              # find which tile we're using for this pixel
              k=get_cat_region(radio_data[0,i],radio_data[1,i],irsacat)

              if k>-1:
                  stars_sel = get_stars_in_pixel(np.asarray([irsacat[k]["ra"],
```

```

        irsa_cat[k]["dec"]]),
        radio_data[0,i],
        radio_data[1,i],2*res)

# record the number of stars used for each pixels Av
Av_n[i]=np.sum(stars_sel*1)

# find the distance from the pixel centre to each star
dist = stars_sel *((irsa_cat[k]["ra"]-radio_data[0,i])**2 +
                    (irsa_cat[k]["dec"]-radio_data[1,i])**2)

# generate the weights for the stars.
# This is done with a exp(-x^2/res^2).
# The factor out the front doesn't matter as we'll normalise later
w = np.exp(-0.5*dist/res**2)*stars_sel

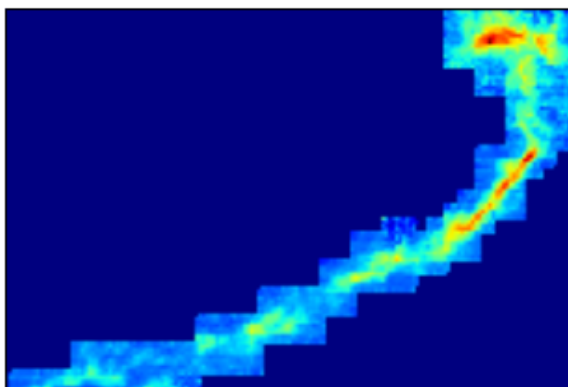
# use the weights and average all possible Av values for the pixel
Av_median[i] = np.sum(w*irsa_cat[k]["av"]*stars_sel)/np.sum(w)

# find the weighted average of the stdev for each pixel
Av_sig[i] = (np.sum(w*irsa_cat[k]["av_std"]*stars_sel)/np.sum(w))
if i%1000==0: print "Av values: ",i,"/",len(radio_data[0,:])

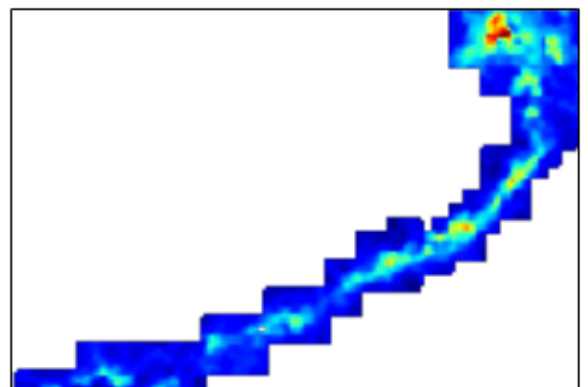
if test:
    plt.figure(figsize=(12,6))
    plt.subplot(121)
    plt.imshow(np.rot90(make_map(radio_data[0,:],radio_data[1:],
                                radio_data[2,:],res),2))
    plt.title("Radio Data",fontsize=20)
    plt.gca().get_xaxis().set_visible(False)
    plt.gca().get_yaxis().set_visible(False)
    plt.subplot(122)
    plt.imshow(np.rot90(make_map(radio_data[0,:],radio_data[1:],
                                Av_median,res),2))
    plt.title("Av Data",fontsize=20)
    plt.gca().get_xaxis().set_visible(False)
    plt.gca().get_yaxis().set_visible(False)

```

Radio Data



Av Data



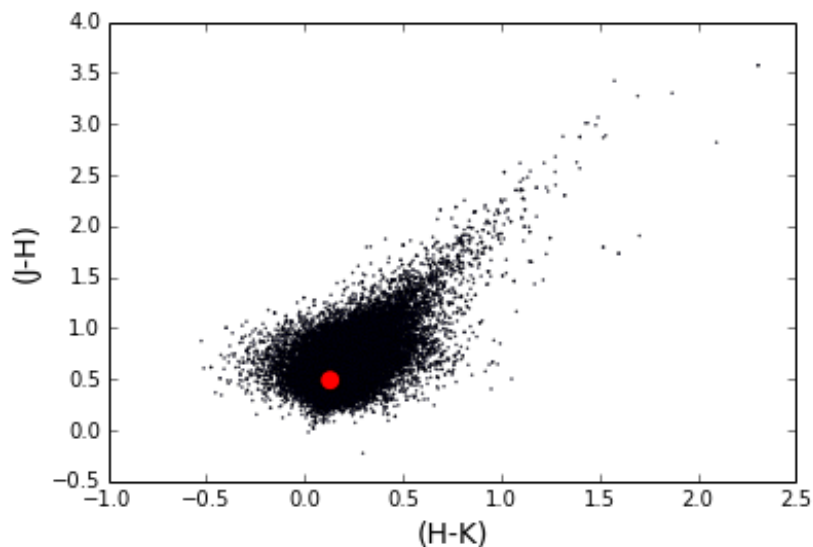


5 - Output a table with the values: RA, Dec, CO, AV, dAV, NCO, NH2, XCO

```
In [16]: gname=C0name[:len(C0name)-4]+"_processed.dat"
#ra
#dec
WCO=flux
AV=Av_median
dAV=Av_sig
nAV=Av_n
NCO=WCO*9.914E14
NH2=AV*9.4E20
XCO=NCO/NH2
table.Table(data=(ra,dec,WCO,AV,dAV,nAV,NCO,NH2,XCO),
             names=("ra","dec","W(C180)","AV","AV_sig","AV_n",
                   "N(C180)","N(H2)","X(C180)")).write(gname,format="ascii")
```

```
In [19]: # Plot the colour-colour diagram to see how if we're on the right track
for cat in irsa_cat:
    plt.scatter(cat["h_m"]-cat["k_m"],cat["j_m"]-cat["h_m"],s=0.2)
    plt.scatter(0.13,0.49,s=100,c="r",zorder=2)
plt.xlabel("(H-K)",fontsize=14)
plt.ylabel("(J-H)",fontsize=14)
```

Out[19]: <matplotlib.text.Text at 0xb2d2590>



Appendix - Danger, here be functions! Load everything below this line before running the pipeline

The following modules are required to run this script - load them before running

```
In [1]: import os
import urllib, urllib2
import numpy as np

# Plotting modules
import matplotlib.pyplot as plt
from matplotlib.colors import LogNorm
import scipy.stats as sps
%matplotlib inline

# Astropy modules.
from astropy.io import ascii, fits
import astropy.table as table
```

Functions: `get_cat_region` gets the 1x1 deg tile that needs is relevant to the pointing in CO. `get_stars_in_pixel` queries every star in the catalogue to find if it is in the pixel beam size (a radius of `res` around the beam centre). This is VERY inefficient and needs to be optimized!!!

```
In [2]: # return a True/False list of all the stars within 2*res of the pixel centre
def get_stars_in_pixel(data,ra_pix,dec_pix,res):
    ra_selection=abs(data[0,:]-ra_pix)<res
    dec_selection=abs(data[1,:]-dec_pix)<res

    return ra_selection*dec_selection

def get_cat_region(ra,dec,irsa_legend):
    for i in r(irsa_legend):
        if irsa_legend[i]==(int(ra),int(dec)): return i

    return -1
```

`NICER_AV` calculates the extinction values towards all stars in an array using the method described in this thesis. If things don't fit, it's probably because the control field constants aren't correct. Play around with the `c_tr` and `J_H_int` and `H_K_int` to fix things. The `k` values come from Rieke and Lubofsky, 1985 and Lombardi and Alves, 2001. The NICER matrices have been expanded in order to speed up the calculations.

```
In [3]: def NICER_AV(cat,
                k=np.array([0.107,0.063]),
                c_tr=np.array([[0.0281,0.0029],[0.0029,0.0277]]),
                J_H_int=0.49,
```

```

        H_K_int=0.13):

star_data= np.asarray([cat["ra"],cat["dec"],
                        cat["j_m"],cat["j_msigcom"],
                        cat["h_m"],cat["h_msigcom"],
                        cat["k_m"],cat["k_msigcom"]])

# array with [Cij_11, Cij_12, Cij_22] because Cij_12=Cij_21.
# The whole fraction operation has been split up into multiplications.
inv_Cij = np.asarray([star_data[5,:]**2+star_data[7,:]**2 + c_tr[1,1],
                        star_data[5,:]**2 - c_tr[1,0],
                        star_data[5,:]**2+star_data[3,:]**2 + c_tr[0,0]])

# find the upper and lower parts of the b vector:
# b.upper = C.k, b.lower = k.C.k
b_lower = inv_Cij[0,:]*k[0]**2 + 2.*inv_Cij[1,:]*k[0]*k[1] + inv_Cij[2,:]
*k[1]**2
b_upper = np.array([inv_Cij[0,:]*k[0] + inv_Cij[1,:]*k[1],
                    inv_Cij[1,:]*k[0] + inv_Cij[2,:]*k[1]])
b = b_upper/b_lower

# dot product the b factors with the colours J-H and H-K vector to find t
he real Av
Av = b[0]*(star_data[2,:]-star_data[4,:]-J_H_int) + b[1]*(star_data[4,:]-
star_data[6,:]-H_K_int)

# find the Variance b.C.b for each star too
Cij = np.asarray([star_data[5,:]**2+star_data[3,:]**2 + c_tr[0,0],
                  - star_data[5,:]**2 + c_tr[1,0],
                  star_data[5,:]**2+star_data[7,:]**2 + c_tr[1,1]])

Av_err = np.sqrt( Cij[0,:]*b[0]**2 + 2.*Cij[1,:]*k[0]*k[1] + Cij[2,:]*b[1
]**2 )

Av_data= np.asarray([cat["ra"],cat["dec"],Av,Av_err])

return Av_data

```

flag_check() looks at the photometric errors of each star and removes those which aren't up to scratch from the list

```

In [4]: def flag_check(cat):
        k=0
        wanted_rows=r(cat)
        for i in r(cat["designation"]):
            if cat["designation"][i]!=cat["designation"][i-1]:
                rd_flg=cat["rd_flg"][i]
                ph_qual=cat["ph_qual"][i]
                if "0" in rd_flg or "4" in rd_flg or "6" in rd_flg or "9" in rd_f

```

```

lg: pass
        else:
            if ph_qual.count("A")>1:
                #if ph_qual.count("A")>1 or ph_qual.count("B")>1 or ("A" in p
h_qual and "B" in ph_qual):
                    wanted_rows[k]=i
                    k=k+1
wanted_rows=wanted_rows[:k]
return cat[wanted_rows]

```

make_red_cat() takes an array of irsa tables, read in my query_2MASS_psc(), and combines them into one single file. This is good for small regions (4 sq deg, L1495 filament) but for huge regions (L1495 surrounds) it become impractical to use such a huge data set.

```

In [5]: def make_red_cat(irsa_cat):
        # play with the tables
        irsa_table = table.vstack(irsa_cat)
        red_cat     = table.Table((irsa_table["ra"],irsa_table["dec"],
                                irsa_table["designation"],
                                irsa_table["j_m"],irsa_table["j_msigcom"],
                                irsa_table["h_m"],irsa_table["h_msigcom"],
                                irsa_table["k_m"],irsa_table["k_msigcom"],
                                irsa_table["rd_flg"],irsa_table["ph_qual"]),
                                names=("ra","dec","designation",
                                        "j_m","j_msigcom",
                                        "h_m","h_msigcom",
                                        "k_m","k_msigcom",
                                        "rd_flg","ph_qual"))
        red_cat     = red_cat.group_by("designation")

        # get rid of the doubles and do a quality check
        red_cat=flag_check(red_cat)
        red_cat.write("pipeline_red_cat.dat",format="ascii")

        return red_cat

```

query_2MASS_psc() looks for the file "RA_DEC.irsa" in the working directory. If it doesn't exist, it calls up the IRSA engine and requests a 1.1 x 1.1 degree (4200"x4200") field centred at RA,DEC. All entries are downloaded and then saved to disk under the name "RA_DEC.irsa". An example name is "61.5+27.5.irsa". The function returns the astropy table of that file.

```

In [6]: def query_2MASS_psc(ra_q,dec_q,width=4200):

        fname="./irsa/" +str(ra_q)+"+"+str(dec_q)+".irsa"
        c='%2C'
        if os.path.exists(fname)==False:
            print " ",str(fname)+" doesn't exist. Querying IRSA"
            url = "http://irsa.ipac.caltech.edu/cgi-bin/Gator/nph-query"
            p = {}

```

```

p['spatial'] = "Box"
p['objstr'] = str(ra_q)+" "+str(dec_q)
p['outfmt'] = 1 # IPAC ascii table format
p['catalog'] = 'fp_psc'
p['size'] = width
#p['selcols'] = 'ra'+c+'dec'+c+'j_m'+c+'j_msigcom'+....

query = urllib.urlencode(p)
get_url = url + "?" + query
handler = urllib2.urlopen(get_url)
raw = handler.read()

print get_url

f=open(fname,"w")
f.write(raw)
f.close()
else: print " ",str(fname)+" exists. Reading in the file"

return ascii.read(fname)

```

Some of the more useful functions are listed here.

```

In [7]: def r(a):
return range(len(a))

def make_map(ra,dec,X,res):

    ra_ex=[np.min(ra),np.max(ra)]
    dec_ex=[np.min(dec),np.max(dec)]
    dpd=1/res

    im=np.ones((dpd*(dec_ex[1]-dec_ex[0])+2,dpd*(ra_ex[1]-ra_ex[0])+2))*np.m
n(X)

    for i in range(len(X)):
        im[round(dpd*(dec[i]-dec_ex[0])),round(dpd*(ra[i]-ra_ex[0]))]=X[i]

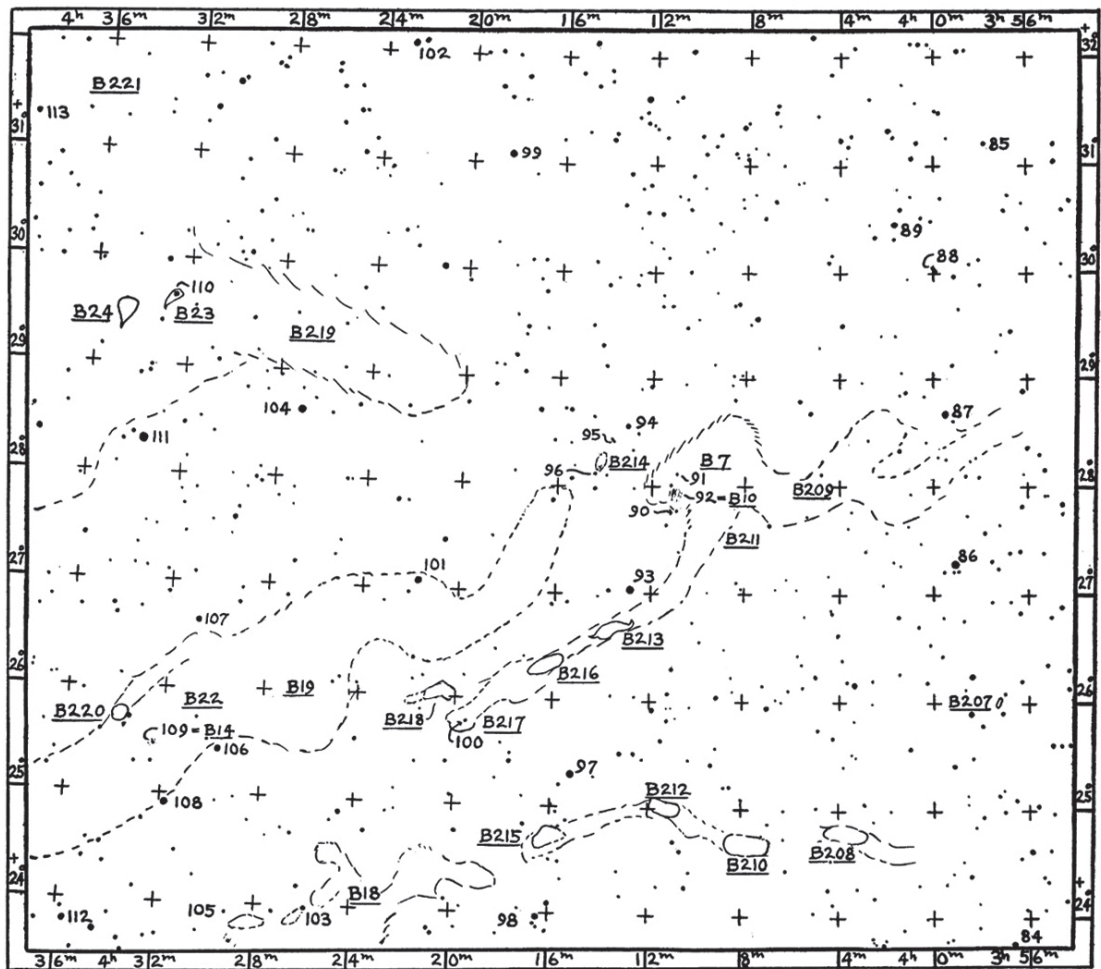
    return im

```

C. Barnard's Catalogue Entries for Taurus



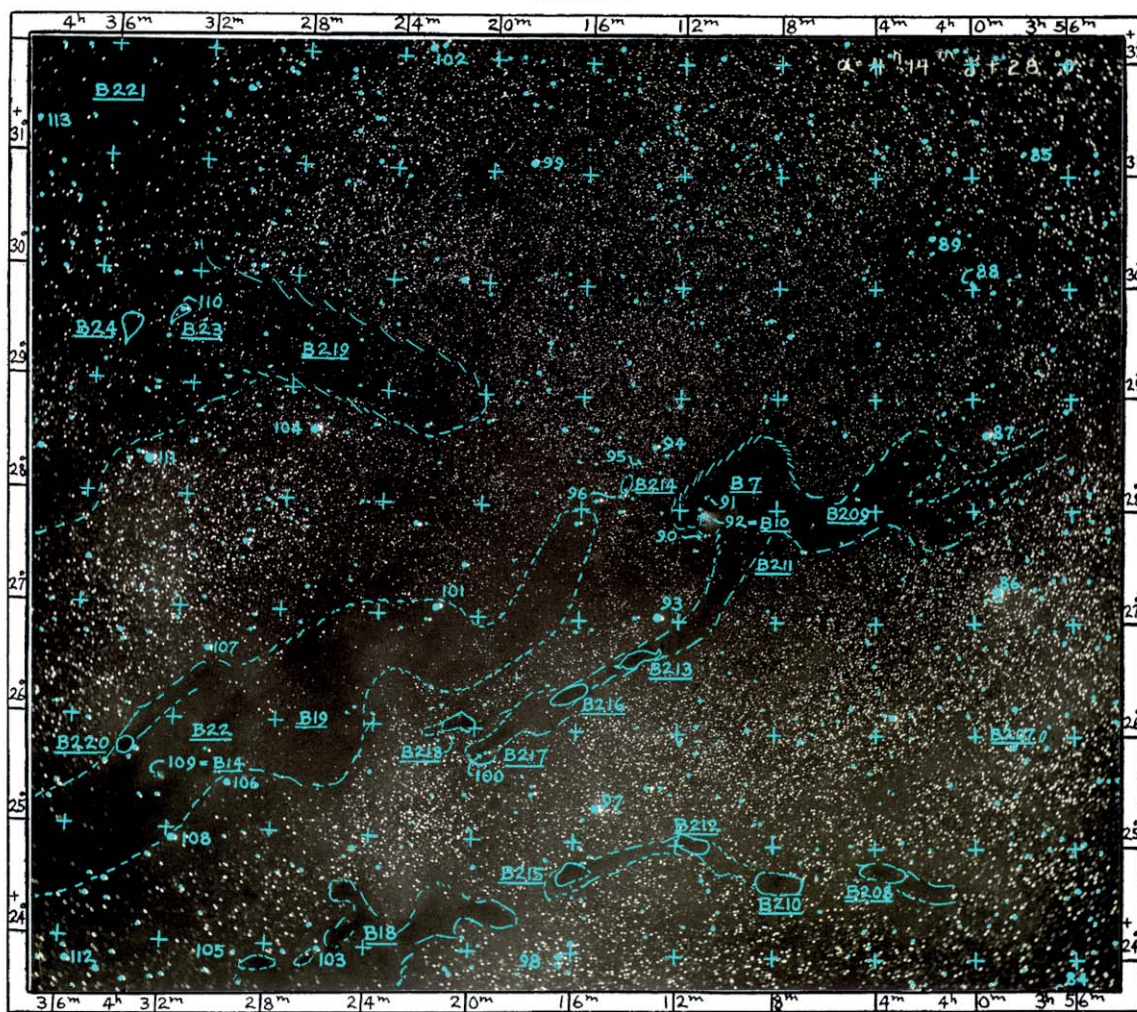
CHART 5



NEBULOUS REGION IN TAURUS

$\alpha = 4^h 16^m 5^s$ $\delta = +27^\circ 57'$

CHART 5



NEBULOUS REGION IN TAURUS

$\alpha = 4^{\text{h}}16^{\text{m}}5^{\text{s}}$ $\delta = +27^{\circ}57'$

TABLE 5

OBJECTS ON PLATE 5 INDICATED ON CHART 5

No.	OBJECT	D.M. MAG.	1875.0		H.D. MAG.		SPEC- TRUM	REMARKS
			α	δ	Ptm.	Ptg.		
84	B.D.+23°609	6.0	3 ^h 56 ^m 53 ^s .3	+23°45'6	5.67	6.09	{F5 A}	36 Tauri
85	B.D.+31°700	7.2	3 57 40.8	+31 9.2	7.43	8.61	K5	
86	B.D.+27°633	5.1	3 58 56.5	+27 15.6	5.27	5.27	A0p	41 Tauri
87	B.D.+28°619	5.4	3 59 16.8	+28 39.7	5.29	5.57	F0	42 ψ Tauri
88	Asteroid	...	4 0 30	+30 2	
89	B.D.+30°623	8.8	4 1 26.2	+30 26.5	8.6	9.6	K0	In N.G.C. 1514
90	B.D.+27°651	8.7	4 10 43.7	+27 47.7	8.8	10.0	K5	
91	B.D.+28°637	9.5	4 10 44.4	+28 9.4	
92	B 10	Neb.	4 10 57	+27 58	
93	B.D.+27°655	5.5	4 12 40.1	+27 3.0	5.06	6.06	K0	52 ϕ Tauri
94	B.D.+28°642	8.2	4 12 51.0	+28 35.4	8.2	8.2	A0	
95	Asteroid	...	4 13 55	+28 25	
96	B.D.+28°645	9.1	4 14 10.0	+28 9.1	Nebulous
97	B.D.+25°707	5.7	4 14 58.6	+25 19.9	5.38	5.36	B9	59 χ Tauri
98	B.D.+23°684	6.5	4 16 27.7	+24 0.5	6.16	6.11	B8	62 Tauri
99	B.D.+31°776	5.0	4 18 9.0	+31 9.3	5.33	6.33	K0	
100	Nebula	...	4 19 30	+25 47	
101	B.D.+27°661	6.5	4 21 36.8	+27 7.6	6.61	6.61	A0	
102	B.D.+32°806	6.5	4 22 37.2	+32 11.0	6.19	6.17	B9	
103	B.D.+23°705	8.0	4 25 55.4	+24 0.8	8.0	8.3	F0	
104	B.D.+28°666	5.7	4 26 48.8	+28 41.8	5.70	5.68	B9	
105	B.D.+23°716	9.4	4 29 14.5	+23 57.6	
106	B.D.+25°720	7.3	4 29 45.8	+25 28.3	7.61	8.68	K2	
107	B.D.+26°731	7.0	4 30 46.4	+26 41.3	6.49	6.77	F0	
108	B.D.+24°674	6.3	4 31 45.9	+24 58.1	6.27	6.35	A3	
109	B 14	Neb.	4 32 20	+25 27	
110	B.D.+29°728	6.5	4 32 28.6	+29 43.5	6.92	7.20	F0	
111	B.D.+28°680	5.0	4 33 30.5	+28 22.2	5.68	5.68	A0	
112	B.D.+23°733	6.8	4 35 39.8	+23 51.0	6.18	6.74	G0	95 Tauri
113	B.D.+31°815	9.0	4 39 6.9	+31 21.6	

DARK OBJECTS

B 207	3 ^h 57 ^m 0	+26°0	B 213	4 ^h 13 ^m 5	+26°8	B 219	4 ^h 27 ^m	+29°3
208	4 4.0	+24.8	214	4 14.2	+28.2	22	4 31	+25.8
209	4 4.7	+28.0	215	4 16.0	+24.8	14	4 32.3	+25.5
210	4 8.0	+24.8	216	4 16.3	+26.3	23	4 32.7	+29.6
211	4 9.5	+27.5	217	4 20.0	+25.8	220	4 33.8	+25.8
7	4 9.7	+28.2	218	4 20.5	+26.0	24	4 35.0	+29.5
10	4 11.0	+28.0	18	4 23.7	+24.1	221	4 36	+31.5
212	4 11.7	+25.0	19	4 26	+26.0			

PLATE 5

NEBULOUS REGION IN TAURUS

$\alpha = 4^{\text{h}} 16^{\text{m}} 5^{\text{s}}$, $\delta = +27^{\circ} 57'$

1907 January 9. 633

Scale: 1 cm = 26'.5, or 1 inch = 67'.3

Galactic Long. = 137°, Lat. = -14°

Exposure = 5^h 29^m

Very few regions of the sky are so remarkable as this one. Indeed the photograph is one of the most important of the collection, and bears the strongest proof of the existence of obscuring matter in space.

The principal object of interest outside the curious dark lanes is the partly bright nebula slightly west (to the right) and south of the center. With its feebler light it covers what appears to be an abrupt, irregular, vacant hole in the dense background of small stars. But there is every evidence that this is not a hole in the stratum of stars, for over its entire extent is a feeble veil of nebulosity with small, round dark spots in it. This veil brightens at its southeastern part until it merges into the small bright nebulosity (No. 92 of the list of stars in Part II), which is abrupt on its north-northeastern side but shades off gently to the west. There can be no question that this nebula with its fainter portions, acting as a screen, causes the apparent vacancy by cutting out our view of the stellar background. From its southern edge a narrow, irregular lane about 3° long runs toward the southeast nearly to the western edge of a great obscuring nebula (B 19), with which it is partly connected. A similar lane in the lower part of the plate, starting in about $\alpha = 4^{\text{h}} 16^{\text{m}}$, $\delta = +24^{\circ} 45'$, runs in a broken manner for some 3°-4° to the west, where it ends in about $\alpha = 4^{\text{h}} 0^{\text{m}}$, $\delta = +24^{\circ} 40'$. Its eastern end fails to connect with the group of curved, dark markings (B 18 of the list of dark objects) by an abrupt break half a degree wide in $\alpha = 4^{\text{h}} 18^{\text{m}}$, $\delta = +24^{\circ} 30'$. This and the lane from the great nebula are uniformly 10' wide, very sharp and free from stars and both have darker spots in them. See B 208, 210, 212, 213, 215, 216. [Further comment on this strange region will be found in Professor Barnard's article in the *Astrophysical Journal*, **25**, 218, 1907.]

In the lower left corner is a great mass of feebly luminous nebulosity, some of which seems to obscure the stars just as the matter in the lanes does. The entire lower half of the plate is

covered with a film of nebulosity in which the small stars seem to be placed.

To the lower right side, in $\alpha = 3^{\text{h}} 56^{\text{m}}$, $\delta = +26\frac{1}{2}^{\circ}$, are portions of some of the nebulous streaks and masses exterior to, but connected with, the Pleiades. Those extending to the east seem possibly to become the dark streaks in the region shown here. (See *Astrophysical Journal*, **41**, 253-58, 1915, where attention is called to this fact.) This nebulosity extends irregularly south-eastward to about $\alpha = 4^{\text{h}} 3^{\text{m}} 5$, $\delta = +24^{\circ} 25'$. There is a long mass of it also in $\alpha = 4^{\text{h}} 0^{\text{m}}$, $\delta = +24^{\circ} 30'$.

About 20' above the bright star B.D. +28°666, of magnitude 5.7, (No. 104) a broad, partly vacant space (B 219) 55' wide, whose edges are rather definite, extends at a slight angle toward the northeast, from about $\alpha = 4^{\text{h}} 20^{\text{m}}$, $\delta = +29^{\circ} 0'$ to its entrance into a large, partly vacant region at the upper left corner of the plate (B 221), which is sprinkled over with comparatively few brighter stars.

A very minute bright nebula (No. 100), in $\alpha = 4^{\text{h}} 19^{\text{m}} 30^{\text{s}}$, $\delta = +25^{\circ} 47'$, is not listed in the N.G.C. The small bright nebula N.G.C. 1514 involves the star B.D. +30°623 (No. 89), of magnitude 8.8. The small nebula at $\alpha = 4^{\text{h}} 14^{\text{m}} 10^{\text{s}}$, $\delta = +28^{\circ} 9'$, resembles a miniature comet with a head and two widely diverging tails. From the "head," which is the star B.D. +28°645 (No. 96), of magnitude 9.1, the main "tail" runs north for about 10' and becomes a dark mass (B 214) that hides the stars. In this respect it somewhat resembles the nebula in the vacancy, B 7, to the west of it.

Two asteroids (numbered as 88 and 95 in our list of stars in Part II) are shown on this plate. The trails, in each case, are about 80'' long.

A slight trail to the bright stars on this plate was due to trouble with the driving clock.

The original negative, No. 380, was made at the Yerkes Observatory.

D. List of Figures

1.	Extinction Map of the whole Taurus region	9
2.	Demarcation of regions within Taurus	11
3.	Extinction map of L1495 based on star counts	19
4.	Black-body curves and Bessel filter response curves	20
5.	The intrinsic scatter of colours found in the control field	23
6.	The shift of colours due to extinction	23
7.	Comparison of extinction maps	30
8.	Pixel for pixel comparison of extinction	31
9.	The relative uncertainties for A_V from Lombardi et al. (2010)	32
10.	Relative uncertainties in extinction measurements	33
11.	^{12}CO and ^{13}CO emission maps of L1495-B213	34
12.	Conversion factor from $W(X)$ to $N(X)$ for ^{12}CO , ^{13}CO and $C^{18}O$	38
13.	Maps of the L1495-B213 Filament - A_V , $N(^{13}CO)$, $N(C^{18}O)$, $X(^{13}CO/C^{18}O)$, $X(^{13}CO)$, $X(C^{18}O)$	42
14.	Maps of the L1495-B213 Surroundings - A_V , $N(^{13}CO)$, $X(^{13}CO)$	45
15.	Global comparison of $N(^{13}CO)$ to A_V	51
16.	Local comparison of $N(^{13}CO)$ to A_V for Barnard regions	54
17.	Global comparison of $N(C^{18}O)$ to A_V	58
18.	Local comparison of $N(C^{18}O)$ to A_V for Barnard regions	60
19.	$N(C^{18}O)/A_V$ versus the surface density of YSOs in the Barnard regions	61
20.	Average abundances of ^{13}CO and $C^{18}O$ compared to H_2	63
21.	Isotopologue ratio between ^{13}CO and $C^{18}O$	65
22.	Spatial position of sources used by Frerking et al. (1982)	67
23.	Comparison of the extinction sources in Frerking et al. (1982) and Lombardi et al. (2010)	68
24.	Comparison of the $N(C^{18}O)$ relationship in Frerking et al. (1982) and this study	69
25.	The $N(C^{18}O) - A_V$ relationship of 6 previous studies	70
26.	Appendix A.1.1: Extinction Map - A_V	83
27.	Appendix A.1.2: Column density map - $N(^{13}CO)$	84
28.	Appendix A.1.3: Column density map - $N(C^{18}O)$	85
29.	Appendix A.1.4: Abundance map - $X(^{13}CO)$	86
30.	Appendix A.1.5: Abundance map - $X(C^{18}O)$	87
31.	Appendix A.1.6: Isotopologue abundance map - $N(^{13}CO)/N(C^{18}O)$	88
32.	Appendix A.2.1: Extinction Map - A_V	89
33.	Appendix A.2.2: Column density map - $N(^{13}CO)$	90
34.	Appendix A.2.3: Abundance map - $X(^{13}CO)$	91

E. List of Acronyms and Symbols

ISM	Interstellar Medium
ISRF	Interstellar Radiation Field
YSO	Young Stellar Object
LTE	Local Thermal Equilibrium
FWHM	Full Width Half Maximum
R.A.	Right Ascension
DEC	Declination
NICE	Near Infrared Colour Excess method for determining extinction
NICER	Near Infrared Colour Excess method Revisited
NICEST	Near Infrared Colour Excess method for small-scale structures
2MASS	Two Micron All-Sky Survey
WISE	Wide-field Infrared Survey Explorer satellite
UKIDSS	UKIRT Infrared Deep Sky Survey
FCRAO	Five College Radio Astronomy Observatory
IRSA	Infrared Science Archive
FITS	Flexible Image Transport System
ASCII	American Standard Code for Information Interchange
HI	Atomic Hydrogen
HII	Ionised Hydrogen
H₂	Molecular Hydrogen
A_V	Extinction
CO	Carbon monoxide, most commonly taken as $^{12}C^{16}O$
¹³CO	Carbon monoxide isotopologue $^{13}C^{16}O$
C¹⁸O	Carbon monoxide isotopologue $^{12}C^{18}O$
W(A)	Total line-of-sight flux, integrated of all observed frequencies. Units of K km/s
N(A)	Total line-of-sight column density. Units of molecules/cm ²
X(A/B)	Abundance ratio of the column densities of two molecules, A and B. If only A is given, the abundance is with respect to the H_2 column density (e.g $X(^{13}CO) = N(^{13}CO)/N(H_2)$)
J, H, K_s	2MASS filter bands centred on: $J = 1.25\mu m$, $H = 1.65\mu m$, $K_s = 2.15\mu m$
τ	Optical depth
T_{ex}	Excitation temperature

F. Deutsche Zusammenfassung

Molekularer Wasserstoff, H_2 , ist einer der wichtigsten Teile des Rätsels der Sternentstehung. Da H_2 bei den Temperaturen, die in den Innenbereichen einer Molekülwolke herrschen, unsichtbar ist, müssen die Eigenschaften und räumliche Ausbreitung von H_2 durch Messungen der Extinktion oder Emission anderer Moleküle wie CO bestimmt werden. Extinktion ist bei allen Wellenlängen vorhanden und steht in einem linearen Verhältnis zur Dichte. Daher ist es die bevorzugte Methode um die H_2 Säulendichte zu bestimmen. Während die Verwendung der Extinktion auf den Bereich sehr naher Wolken beschränkt ist, kann CO auch in anderen Galaxien detektiert werden. Daher spielt der Konvertierungsfaktor zwischen diesen beiden Methoden eine große Rolle in vielen Bereichen der Astronomie.

Im Rahmen dieser Diplomarbeit wurden sieben verschiedene Regionen des L1495-B213 Filaments untersucht, um das Verhältnis zwischen ^{13}CO , $C^{18}O$ und A_V auf einen genaueren Wertebereich einzuschränken und dabei die relativ großen Diskrepanzen zwischen den bisher veröffentlichten Gradienten aufzuklären.

Extinktionskarten wurden mit Hilfe des 2MASS-Katalogs (Skrutskie et al., 2006) und der NICER-Methode (Lombardi and Alves, 2001) erstellt und wurden Pixel für Pixel mit den Karten der ^{13}CO und $C^{18}O$ Säulendichten von Goldsmith et al. (2008) und Hacar et al. (2013) verglichen. Insgesamt wurden folgende acht Datensätze untersucht: Das gesamte L1495-B213 Filament, die angrenzende Region (nur in A_V und ^{13}CO) und die 7 Subregionen des L1495-B213 Filaments.

Dabei wurde eine relativ schwache Korrelation zwischen ^{13}CO und H_2 bei mittleren bis hohen Säulendichten festgestellt. Andererseits war ein annähernd lineares Verhältnis zwischen $C^{18}O$ und Extinktion im Bereich $2^m < A_V < 20^m$ zu sehen. Der beste lineare Fit zum $A_V - C^{18}O$ Verhältnis entlang des L1495-B213 Filaments war:

$$N(C^{18}O) = (2.25 \pm 0.37) \times 10^{14} \cdot (A_V - 1.07 \pm 0.60)$$

Zusätzlich dazu wurde eine schwache Korrelation zwischen der $C^{18}O$ -Häufigkeit und der YSO-Flächendichte (Hacar et al., 2013) gefunden. Ähnlich wie in der Arbeit von Wilson and Rood (1994) wurde für das Verhältnis zwischen den Säulendichten von ^{13}CO und $C^{18}O$ ein Wert von $N(^{13}CO)/N(C^{18}O) \approx 8 \pm 3$ gefunden.

Die Untersuchung von sieben Subregionen in L1495-B213 hat gezeigt, dass es eine große Bandbreite an $^{13}CO - H_2$ und $C^{18}O - H_2$ -Verhältnissen gibt. Dies spiegelt sich auch in der Literatur der letzten 30 Jahren wider. Es wurde festgestellt, dass sich ^{13}CO besonders als Tracer von diffusem, extra-filamentärem Gas eignet und nicht für die Bestimmung der Masse von Filamenten oder Kernen eingesetzt werden sollte. Womöglich sollte stattdessen $C^{18}O$ bevorzugt werden. Dabei muss jedoch beachtet werden, dass die ^{13}CO und $C^{18}O$ Häufigkeiten sehr stark von der unmittelbaren Umgebung abhängig sind und dass unterentwickelte Regionen einen höheren ^{13}CO - und $C^{18}O$ -Anteil aufweisen.

G. Curriculum Vitae



Kieran Leschinski

Curriculum Vitae

Education:

- 1999 – 2004 Patterson River Secondary College
VCE – Successful completion with a final grade of 97.2%
- 2005 – 2011 Monash University
Bachelor of Science (Physics) – Complete
Bachelor of Engineering (Civil) – Deferred
- 2009 University of Vienna - IfA
Study Abroad Exchange Year
- 2009 – 2011 International Astronomical Youth Camp (IAYC) – Participant
- 2011 – 2012 Australian Astronomical Observatory (AAO)
Summer Internship: Supervised by Dr Michelle Cluver
- 2012 – Present University of Vienna
Master's of Science (Astronomy)

Work Experience:

- 2001 – 2011 CSIRO Science Education Centre
Laboratory Technician
Holiday Programme Supervisor
- 2005 International Lycee Novgorod, Russia
English Language Assistent
- 2008 – 2011 Private Tutor (Physics, Chemistry, Maths)
- 2013 University of Vienna - IfA
Tutor

Public Outreach:

- 2011 – Present International Astronomical Youth Camp (IAYC) – Group Leader
- 2012 – Present Member of the International Workshop for Astronomy (IWA e.V.)
- 2013 – Present Vice President of IWA e.V.

Publications:

- Title: Galaxy and Mass Assembly (GAMA): Mid-infrared Properties and Empirical Relations from WISE
- Journal: The Astrophysical Journal, Volume 782, Issue 2 id. 90
- Preprint: arXiv:1401.0837
- Authors: Cluver et al.
- Year: 2014

Proposals:

- 03.2013: ESO APEX SHFI, Semester 94 (Pending)
- Title: Inferring the UV radiation field around molecular clouds using ground-based observations
- PI: Kieran Leschinski
- 03.2014: ESO APEX SHFI, Semester 93 (Accepted)
- Title: On the internal structure of massive filaments
- PI: Dr Alvaro Hacar

Other Projects:

- 2013 – Present: Xbox Edithvale Remote Observatory (XERO)
A stand-alone micro-observatory using consumer electronics in the southern hemisphere for short, medium and long term tracking of variability in bright (<5^m) stars.